



Optical Spectroscopy of $3d$ and $4d$ correlated electron systems.

INAUGURAL-DISSERTATION
zur
Erlangung des Doktorgrades
der Mathematisch-Naturwissenschaftlichen Fakultät
der Universität zu Köln

vorgelegt von
M.Sc. IGNACIO VERGARA KAUSEL
aus
SANTIAGO, CHILE

Köln, 2022

Berichterstatter (Gutachter):

Prof. Dr. Markus GRÜNINGER

Prof. Dr. Joachim HEMBERGER

Vorsitzender:

Prof. Dr. Stephan SCHLEMMER

Beisitzer:

Dr. Christoph GRAMMS

Tag der mündlichen Prüfung: 24.11.2022

as accepted by the Faculty of Mathematics and Natural Sciences of the
University of Cologne.

Ich versichere, dass ich die von mir vorgelegte Dissertation selbständig angefertigt, die benutzten Quellen und Hilfsmittel vollständig angegeben und die Stellen der Arbeit - einschliesslich Tabellen, Karten, und Abbildungen -, die anderen Werken im Wortlaut oder dem Sinn nach entnommen sind, in jedem Einzelfall als Entlehnung kenntlich gemacht habe; dass diese Dissertation noch keiner Fakultät oder Universität zur Prüfung vorgelegen hat; dass sie - abgesehen von unten angegebenen Teilpublikationen - noch nicht veröffentlicht worden ist sowie, dass ich eine solche Veröffentlichung vor Abschluss des Promotionsverfahrens nicht vornehmen werde. Die Bestimmungen dieser Promotionsordnung sind mir bekannt. Die von mir vorgelegte Dissertation ist von Prof. Dr. M. Grüniger betreut worden.

Acknowledgments

THIS ENTERPRISE STARTED QUITE SOME TIME AGO, when I came to Cologne in 2010 for a Master degree and ends with this milestone: a Doctoral Thesis. This journey had many ups and downs, times of doubt and some of certainty, lonesomeness, and communion. New hobbies, a brief stint at a rock band, a family, a transition into the *real* world, a global pandemic, and a job change in the middle of said pandemic, while attempting to be a supportive partner. Quite a different life, but still mostly the same person.

First and foremost, I would like to acknowledge and deeply thank Markus, my doctoral supervisor, for whom I have the uttermost respect. To thank him for all his support, (extreme) patience, and teachings throughout my years in this institute that kept me going on. I did thoroughly enjoy his lectures and way of viewing physics, to the point of going to his lectures regardless if it was directly useful for me. His enthusiasm and keen eye for physics, and in particular, correlated electron systems, was contagious and inspiring. It was great to see that good quality research being done in this day and age, not falling into hype and hyperbole. He is what I expected the scientific endeavor to be, not like what I discovered it to be. This is a feat not easily achieved.

During my research, I did benefit directly from some of my colleagues, whom I would like to acknowledge. Martin Valldor for managing to successfully grow for us the $\text{La}_2\text{Cu}_2\text{O}_5$ crystals of the ladder and Luis Fels for preparing said sample and showing me how to operate the Fourier spectrometer. To Kai Schmidt, Stefan Wessel, and Kris Cöster for the extensive collaboration on the theory side of the ladder system. My chapter on $\text{La}_2\text{Cu}_2\text{O}_5$ would not be the same without this collaboration. Daniele Fausti for approaching us with what in principle seemed like a simple request, but that ended up being a good research opportunity in itself and pushing forward the research on the magnetite. And last but not least, Stefan Kunkemöller for providing the ruthenate samples and their physical characterization.

Also, many thanks to Matteo Montagnese, who upon his arrival to Cologne and the institute, took the position of lunch companion and friend with many hours

0. ACKNOWLEDGMENTS

discussing or complaining about almost any topic imaginable. An honorable mention to Francesco Randi, for his superb job while collaborating on the magnetite and then while attempting to program a small toolbox for optics was a pleasure. Is a shame we never really got to move beyond the project being an exploration. Lastly, a big thanks to Raphael German with whom I kept contact long after leaving the institute and who has been a good friend throughout the years.

At last, other friends and family, particularly my life partner, who have in one way or another supported, encouraged, and accompanied me in the highs and low, ups and downs of this whole enterprise, my deep thanks and timeless gratitude and appreciation.

Abstract

In the context of this work, three different materials are studied via optical spectroscopy methods. The three materials are $\text{La}_2\text{Cu}_2\text{O}_5$, Fe_3O_4 , and Ca_2RuO_4 , where the first one is investigated via Fourier spectroscopy, while the latter two are studied via spectroscopic ellipsometry.

$\text{La}_2\text{Cu}_2\text{O}_5$ is a low-dimensional material, particularly, a spin-1/2 4-leg ladder system that dimensionally lays in between the 1D chain and the 2D layer. While 2-leg ladder systems have been studied before, growing in the number of legs involved allows us to study the dimensional crossover towards 2D and attempt to understand the physics in the complex 2D layered cuprates that show, among other things, high-temperature superconductivity. We successfully measured the first optical spectra of this kind of material, obtaining a spectra that in many ways resembles the one obtained for 2-leg ladders.

The second material, Fe_3O_4 , a very classic material of study in the field of correlated electron systems still hosting controversies is revisited. We thoroughly studied the optical spectra as a function of temperature, particularly across the magnetic phase transition. In return, we were able to clarify a discrepancy in the literature concerning the temperature behavior of the features observed in the optical spectra. There we observe clearly two excitation features, where one of them was not completely clear from previous reports. Furthermore, both features show opposite temperature dependence. Having this experimental result, enabled us to dispel a second controversy, where the interpretation of these features was not clear. Thus, we interpret the features observed in the optical spectra, based on their temperature dependency, as intersite transitions of minority spins from the $\text{Fe}_B^{2+} t_{2g}$ levels to the t_{2g} and e_g levels of Fe_B^{3+} site.

At last, Ca_2RuO_4 , is a layered bulk system where the spin-orbit coupling potentially plays a role due to the $4d$ Ru. And while there was agreement in the presence of two features, at about 1 eV and 2 eV, in the optical spectra belonging to $d^4d^4 \rightarrow d^3d^5$ Mott-Hubbard excitations, the detailed behavior of those features as a function of temperature was not previously reported. Our measurements and analysis permitted us to establish that the spectral weight of the first feature con-

0. ABSTRACT

siderably increases as the temperature increases, while the second feature marginally does so. We attempted, with a simple theoretical model considering only spin changes, to explain this behavior in the spectral weight. While the behavior of the lowest energy feature can be explained, the second one shows opposite directions clearly indicating the shortcomings of our assumptions, namely, not considering distortions and spin-orbit coupling.

Contents

Acknowledgments	i
Abstract	iii
1 Introduction	1
2 Correlated Electron Systems	7
2.1 $3d$ orbitals and crystal-field splitting	8
2.2 Hubbard Model	10
2.3 Mott-Hubbard and Charge-Transfer Insulators	13
2.4 Spin-Orbit Coupling	14
2.5 Correlations and optics	15
3 Optical Spectroscopy	19
3.1 Light-matter interaction	20
3.1.1 Optical constants	22
3.1.2 Kramers-Kronig relations	24
3.1.3 Oscillators	24
3.2 Sample preparation	28
3.3 Fourier spectroscopy	29
3.3.1 Setup and measurement	32
3.3.2 Spins, phonons, and light: bimagnon-plus-phonon absorption	32
3.4 Spectroscopic ellipsometry	34
3.4.1 Ellipsometric angles	35
3.4.2 Setup and measurement	38
3.4.3 Data analysis	39
4 $\text{La}_2\text{Cu}_2\text{O}_5$: a 4-Leg Spin-1/2 Ladder System	45
4.1 Low-dimensional quantum spin systems	45
4.1.1 Spin chain	46

Contents

4.1.2	n-leg spin ladders	49
4.1.3	2D $S = 1/2$ square lattice	57
4.2	4-leg ladder $\text{La}_2\text{Cu}_2\text{O}_5$	59
4.3	Results	62
4.4	Analysis	65
4.5	Discussion	72
4.6	Conclusions	75
5	Revisiting Magnetite	77
5.1	Crystal, Magnetic, and Electronic Structure	79
5.2	Optical Spectroscopy	84
5.3	Measurements and Results	85
5.4	Conclusions	96
6	Mott-Hubbard excitations in Ca_2RuO_4	99
6.1	Physical Characterization	100
6.1.1	Crystal-field splitting vs. spin-orbit coupling	104
6.2	Optics on Ca_2RuO_4	107
6.3	Results	112
6.3.1	1% Ti doped	113
6.3.2	10% TI doped	114
6.4	Analysis	114
6.4.1	1% Ti doped	114
6.4.2	10% Ti doped	119
6.4.3	Peak assignment	121
6.4.4	Transition matrix elements	124
6.4.5	$S_z = 0$ states	130
6.5	Conclusion	133
7	Conclusion	135
A	Appendix	139
	Bibliography	143
	Publications	165

1. Introduction

Not only is the Universe stranger than we think, it is stranger than we can think.

Werner Heisenberg

IN CONTEMPORARY PHYSICS, as in many other areas of science, the study of properties that emerge from the interaction of elements is a vibrant and active topic. In *condensed matter physics* such subfield is called *correlated electron systems* (CES). These systems' hallmark is the many-body character arising out of the strong interactions between the electrons in the material. Due to the many-body nature of these systems, the basic premise of what could be regarded as "classical" or "text-book" Condensed Matter Physics, namely to consider electrons as non-interacting entities in a periodic potential, is not the right approach.¹ For this, the Pauli exclusion principle can be held responsible as it constrains the phase space available for electron excitations small compared to the Fermi energy. This means that electron-electron interactions often have a small effect on the properties of materials, and thus, in many materials, it can be safely disregarded.

In correlated electron systems, the strong electrostatic electron-electron interaction gives rise to a plethora of fascinating, puzzling, and highly complex phenomena. For example, new ground states like quantum spin liquids with correspondingly new excitations are observed.

Not surprisingly, some commonly experienced phenomena like magnetism are, ultimately, due to electron-electron interaction. Magnetism is not the only one. Other phenomena originating from electronic correlations are colossal magnetoresistance (CMR) in manganates [1], metal-insulator transitions (MIT) [2, 3] in, *e.g.*,

¹It is worthy to note that it is somewhat surprising at first sight that the independent electron approximation describes many materials very well.

Chapter 1: Introduction

vanadates, and unconventional² superconductivity [4] in cuprates to name a few of them [5].

Correlated electron systems play a central role in contemporary condensed matter physics, as they provide a rich and varied playground to explore fundamental issues in physics. Exotic states of matter like Weyl quasiparticles [6], Majorana fermions [7], among others, can be realized in this class of systems.

Besides these fundamental topics, correlated electron materials have tremendous potential for technological devices [8]. One such example exploits the metal-insulator transition driven by temperature found in vanadates to make windows that switch between reflecting or transparent to infrared radiation, at high and low temperatures, respectively [9]. Moreover, there is not only a significant potential for applications but there are already some available. One of the most common ones is the use of manganates, which are already in use in magnetic storage solutions, *e.g.*, magnetic hard drives, by exploiting the colossal magnetoresistance (CMR) where small changes in an applied magnetic field yield massive changes in electrical resistivity [10]. This effect has been responsible for the explosion in the storage density of magnetic hard drives. Furthermore, it is impossible not to mention the wide breadth of high-temperature superconductivity applications, as people have been fascinated by the potential they promise. High-temperature superconducting materials are already applied to reduce the size, increase the efficiency, or make new devices available in power generation and transmission, transport, information technology, science, and medicine [11].

Ultimately, all these interesting emerging phenomena in correlated electron materials arise from the interaction of the electron's charge, spin, orbital, and lattice degrees of freedom. The competition between these many degrees of freedom provides complex, rich, and sometimes mind-boggling phenomena. Unfortunately, many-body physics is a complicated subject as most relevant models are not exactly solvable and, in many cases, even too costly to explore computationally.

This emerging complexity can be seen in the rather complex and rich phase diagrams of this class of materials. For example, one such phase diagram is sketched in fig. 1.1 for a typical layered cuprate material like $\text{La}_{2-x}\text{Sr}_x\text{CuO}_4$, where many different phases compete and emerge in the various regions of the temperature-doping diagram. Most notably is the destruction of the low-temperature antiferromagnetic (AF) order and the emergence of a superconducting (SC) state when

²Namely not through a phonon induced Cooper pairing of electrons and where the order parameter has a lower symmetry than the one shown by the lattice.

sufficiently hole-doped. It is believed that antiferromagnetic interactions could be the driving mechanism behind correlated superconductivity and other electronic ordered phases present [12].

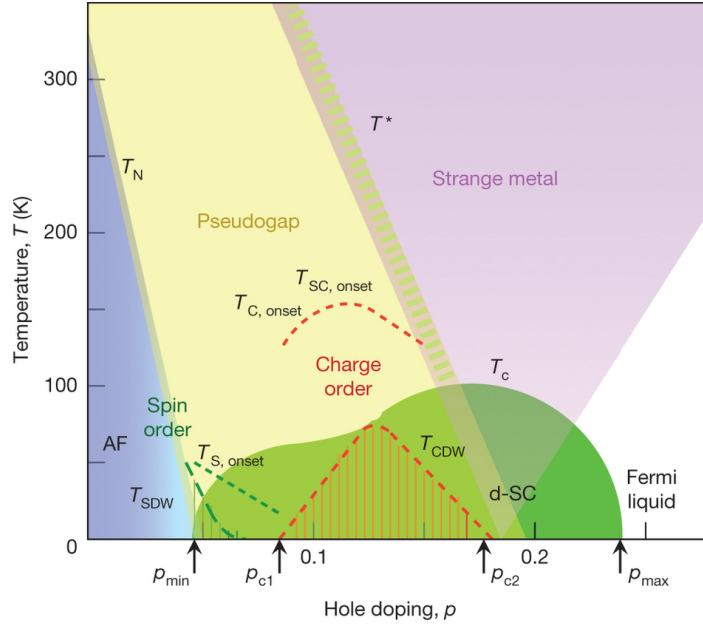


Figure 1.1.: Sketch of a temperature-doping (\mathbf{T}, \mathbf{x}) phase diagram of a correlated electron system like $\text{La}_{2-x}\text{Sr}_x\text{CuO}_4$. It shows the competition between different phases. Antiferromagnetic (AF), superconducting (SC), and spin-glass (SG) phases are reached by varying the temperature (\mathbf{T}) and the doping level (\mathbf{x}) of the system. Reproduced from [13].

Not only the localization of electrons due to their correlations and the interaction between different degrees of freedom are relevant for the physical properties of these systems. Another essential concept is dimensionality, since reducing it enhances the correlations and their effects. For example, going from a 3D system to a quasi-2D system composed of stacked layers is critical for the emergence of superconductivity in the cuprates. Going even further, to a spin 1/2 quasi-1D system, the role of quantum fluctuations in the observed phenomena is greatly enhanced. For example, in the $S = 1/2$ spin chain, this enhancement leads to complete long-range order suppression even at $T = 0$.

In the context of correlated electron systems, optical spectroscopy is a versatile tool to explore the electrons' behavior. Optical methods allow us to study materials in a non-destructive way and to peek into the microscopic behavior of the electrons. The two techniques used in this work are Fourier transform infrared (FTIR) spectroscopy and spectroscopic ellipsometry.

Chapter 1: Introduction

This thesis' organization is as follows: Chapter 2 starts with a general description of the main elements to understand correlated electron systems and their relationship with optics. Then in chapter 3, the basics of optical spectroscopy and the experimental methods used in this work are briefly described. The core of this thesis follows by exploring a diversity of correlated electron systems.

In chapter 4, we study the magnetic excitations as a function of temperature of the 4-leg ladder system $\text{La}_2\text{Cu}_2\text{O}_5$ employing infrared spectroscopy. Until now, the primary outcome of light absorption and scattering experiments on the 2-leg ladder has been the observation of magnetic singlet bound states arising from strong triplet-triplet interactions [14]. These bound states characterize the excitation spectra of these low-dimensional spin systems. Besides a fundamental interest in low-dimensional quantum magnets, a strong motivator in studying the magnetic excitations in 4-leg ladders cuprates lies in the fact that the current understanding of the optical spectroscopy of the quasi-2D square layer cuprates is not fully described. By trying to perform a dimensional crossover from the well-understood 1D chain to the 2D square layer, *i.e.*, going through the ladders, we expect to learn how to better describe the spectra of such a cornerstone piece of modern condensed matter physics.

We successfully measured the first optical spectra of a 4-leg $S = 1/2$ ladder cuprate via Fourier spectroscopy. There is a strong resemblance between the measured spectra of the 4-leg ladder and the 2-leg ladder. This similitude gives a hint that some 2-leg character continues to be present when transitioning from 2 to 4 legs, which leads to an interpretation of the features in similar terms. Thus, we interpret the features observed as coming from a 2-triplon quasi-bound state and a continuum of magnetic excitations. There is one extra feature, a clear peak with a satellite shoulder whose origin is unclear so far.

Then, in chapter 5, the behavior of Fe_3O_4 (magnetite) across the Verwey transition is studied. Magnetite has been studied for more than a century and is known for even longer, leading to many applications since its discovery. Despite this fact, magnetite still offers open questions regarding its physics. There is currently an experimental disagreement on the shape and temperature dependence of the optical spectra, which we set to answer. Moreover, high-quality measurement and modeling of magnetite's optical spectra also set the basis for further research into the non-equilibrium optical response. The literature on magnetite's optical conductivity is controversial, particularly around the optical feature around 2 eV, as reported by reflectivity measurements performed via Fourier spectroscopy.

We can clarify the behavior and character of the two observed features in the optical spectroscopy that show opposite temperature-dependent behavior. Given

this behavior, we interpret the excitation as intersite transitions of minority spin from the t_{2g} levels to the t_{2g} and e_g levels. Moreover, the detailed measurement across the Verwey metal-insulator transition shows an explicit step-like behavior of these two features.

Finally, the ruthenate Ca_2RuO_4 , being a prototypical multi-orbital Mott system, is studied in chapter 6. Materials of the family $\text{Ca}_{2-x}\text{Sr}_x\text{RuO}_4$, are layered perovskite that are isostructural to the $\text{La}_{2-x}\text{Sr}_x\text{CuO}_4$ high-temperature superconducting cuprates. The understanding of the orbital degree of freedom in the ground state of Ca_2RuO_4 has been elusive. We use spectroscopic ellipsometry to follow the optical spectra's temperature dependence and assign the observed features to plausible electronic transitions.

We dispel the contradiction in the literature, where the behavior of the two features observed was not clear. Our measurements establish that the first observed feature increases considerably in spectral weight while the second does it marginally as a function of increasing temperature. We also calculated the transition matrix element to estimate the spectral weight changes between a low- and a high-temperature state. The result of this calculation agrees with the observed temperature dependence of the first spectral feature as a function of temperature but gives the opposite direction for the second one hinting to a possible role played by the spin-orbit coupling in this material.

2. Correlated Electron Systems

The miracle of the appropriateness of the language of mathematics for the formulation of the laws of physics is a wonderful gift which we neither understand nor deserve.

Eugene Wigner

BY THE EARLY 1930S, very shortly after the development of quantum mechanics, a successful quantum theory of electrons in solids was developed. This theory, based on weakly interacting electrons in a periodic potential, classifies solids as metals, insulators, and semiconductors depending on the filling of their electronic bands [15–18]. It is formidable that such a crude approximation can provide so much, but this is not an isolated case in physics.¹ Regardless of this feat, this theory fell short of classifying some transition-metal oxides correctly.

Two early examples showing the limitations of band theory are NiO and Fe₃O₄ [19, 20]. For these materials, band theory predicts a metallic state due to partially filled bands. However, experiments showed that NiO behaves as an insulator, and Fe₃O₄ is a very poor conductor at room temperature while showing an unexpected temperature-driven metal-insulator transition at about 121 K [21]. It can be claimed that with these observations, the field of strongly correlated electron systems got kickstarted. This situation led to the realization that something was missing in the basic description of solids. Mott and Peierls [20] stated in 1937:

A rather drastic modification of the present electron theory of metals would be necessary to take these facts into account.

¹Particularly interesting is the result of Drude for the electrical conductivity that regardless of being based on a classical approach coincided with the semi-classical one performed by Sommerfeld later on.

With such modification being that strong Coulomb interaction play a pivotal role for compounds like NiO and Fe_3O_4 . Ultimately, this modification meant that such interaction could not be considered as an afterthought as in a perturbation. However, it has to be fully considered from the beginning into the physics of these systems. Unfortunately, explicitly treating the electron interaction leads to the enormous and complicated task of handling many-body problems.

Many of these materials are *transition-metal oxides* (TMO) with partially filled d bands. In these materials, the narrow radial extension, or bandwidth, of the d orbitals boosts the importance of the repulsive Coulomb interaction between the electrons. The stronger Coulomb interaction with the reduced bandwidth gives rise to correlation effects between electrons beyond what a mean-field approximation can describe. Ultimately, the correlation of electrons leads to the scenario where the electrons are forced to be localized in real space at half-filling. This is the opposite picture compared to the free, fully delocalized states in band theory and closer to atomic physics. Strong electron-electron interactions are not only present in TMO's like NiO or Fe_3O_4 , but also in other d - and f - electron systems, heavy metals [22]. This strong electron-electron interaction also gives rise to a wide variety of physical phenomena due to the interplay of various degrees of freedom present: spin, charge, and orbital, plus their interactions with the lattice and each other. Furthermore, when these systems are doped, the electrons are not necessarily localized, which leads to complex interactions between the degrees of freedom previously mentioned.

This chapter aims to provide a basic vocabulary and qualitative descriptive framework regarding correlated electron systems. It starts with a description of on-site properties commonly found in transition-metal oxides, then describes inter-site properties through the Hubbard model and how it opens the door to understanding correlated electron phenomena, to later explain the role of optics in investigating this class of materials. A more extended introduction and detailed description of the theory can be found in [23, 24].

2.1. $3d$ orbitals and crystal-field splitting

Knowing the local environment of the relevant ion and the on-site orbital properties is crucial to understanding the phenomena observed in solids. The local environment dramatically influences the excitations possible in a material.

The d orbitals ($L = 2$) in a free transition-metal ion are five-fold degenerate, as seen in fig. 2.1. For example, in YTiO_3 the electronic configuration of the

2.1 3d orbitals and crystal-field splitting

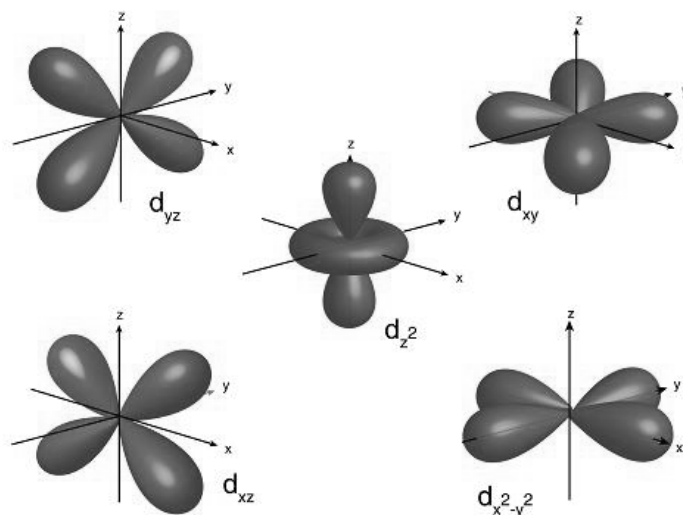


Figure 2.1.: When placed in an octahedral environment, the five 3d orbitals split into the t_{2g} (upper row) and e_g (lower row) groups. By CK-12 Foundation [CC BY-SA 3.0].

transition-metal ion is Ti^{3+} ($[\text{Ar}]3d^1$) with one electron in the 3d level. Or consider the case of La_2CuO_4 with a Cu^{2+} ($[\text{Ar}]3d^9$) state, where the Cu ion has nine electrons or alternatively one hole. The question is which orbitals are occupied in each case. For this, we need to know the local environment of the transition-metal ion.

The transition-metal ion is surrounded by, *e.g.*, oxygen ions, so-called ligands. The ligands' electric fields introduce anisotropy at the transition metal position, producing a local crystal field that lifts the degeneracy of the d orbitals. Simple cases of typical local environments in transition-metal compounds, as shown in fig. 2.2, are the octahedral (left) and tetrahedral (right) ones.

When placed in octahedral (fig. 2.2 left) or tetrahedral (fig. 2.2 right) coordination, the d orbitals split into a double and a triple degenerate level, named e_g and t_{2g} , respectively. The energy splitting is commonly expressed as $10Dq$ with a typical energy of about 1 eV to 5 eV, and it is schematically shown in fig. 2.3. The e_g orbitals consist of the $d_{x^2-y^2}$ and $d_{3z^2-r^2}$ orbitals, whereas the t_{2g} orbitals consist of the d_{xy} , d_{yz} , and d_{xz} orbitals. In octahedral coordination, the lobes of the t_{2g} orbitals point towards the midpoints between ligands while the e_g ones towards the ligands. This orientation means that the t_{2g} orbitals are lower in energy than the e_g ones. For tetrahedral coordination, the splitting is inverted. Additional anisotropies, caused by distortions like Jahn-Teller or steric effects or

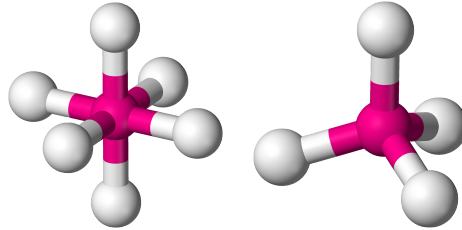


Figure 2.2.: The pink (central) balls represent the transition-metal ion, whereas the ligands are represented as grey balls. The ligands are usually oxygen thus leading to the name transition-metal oxides. Two common coordination geometries are octahedral (left) and tetrahedral (right).

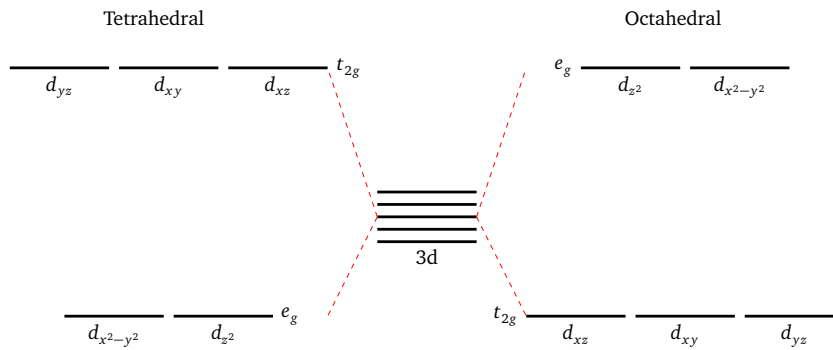


Figure 2.3.: For octahedral and tetrahedral coordination, the five d orbitals split into two groups, a triply degenerate t_{2g} , and a double degenerate e_g .

different coordination, further split the $3d$ ion orbitals' degeneracy.

2.2. Hubbard Model

The simplest theoretical model capturing the essential physics of correlated electrons is the one-band Hubbard model [25, 26], which consists of a single non-degenerate orbital per site² and an on-site Coulomb interaction. Regardless of the many simplifications involved in this model, it can describe low-energy and low-temperature properties of correlated electron systems. This model shows the competition between delocalizing and localizing effects in these systems. It has

²It can be visualized as a lattice of hydrogen atoms with a non-degenerate $1s$ orbital at each site.

two parts,

$$H_H = H_0 + H_I \quad (2.1)$$

where H_0 expresses the kinetic energy or electron hopping in the lattice as in band theory, *i.e.*, an electron in a periodic potential, and H_I the interaction between electrons describing the penalty incurred for double occupancy. Here it is very explicit the interplay between electron kinetic energy reduction by delocalization and the localization of the electrons due to Coulomb interaction. Despite its simplicity, this model can describe the Mott insulating state, the emergence of long-range magnetic order, and the metal-insulator transition [25, 26] among other correlated electron phenomena.

The term H_0 is given by

$$H_0 = -t \sum_{\langle i,j \rangle, \sigma} (c_{i\sigma}^\dagger c_{j\sigma} + h.c.) \quad (2.2)$$

where the sum, in the simplest case, is carried over the nearest neighbors and over the electron spins $\sigma = \uparrow, \downarrow$. $c_{i\sigma}^\dagger$ ($c_{j\sigma}$) is the creation (annihilation) operator, which operates on site i (j) with spin $\sigma = \uparrow, \downarrow$. The parameter t is the hopping matrix element given by the overlap of the electrons between sites.

Regarding the interaction term, the most straightforward description is provided by taking into account only an on-site effect given by

$$H_I = U \sum_i \hat{n}_{i\uparrow} \hat{n}_{i\downarrow} \quad (2.3)$$

where $\hat{n}_{i\sigma} = c_{i\sigma}^\dagger c_{i\sigma}$ is the occupation number operator on site i and spin $\sigma = \uparrow, \downarrow$, and U describes the strength of the electron-electron on-site interaction.³ Thus U is the energy cost of double occupancy on a site.

³The parameter U is formally defined as the overlap integral between the electrons given by

$$U = \int d\mathbf{r}_1 \int d\mathbf{r}_2 |\phi(\mathbf{r}_1 - \mathbf{R}_i)|^2 \frac{e^2}{|\phi(\mathbf{r}_1 - \mathbf{r}_2)|} |\phi(\mathbf{r}_2 - \mathbf{R}_i)|^2 \quad (2.4)$$

where ϕ is the electron wavefunction and \mathbf{R}_i is a lattice site. Frequently this parameter acts as a phenomenological one and is determined experimentally.



Figure 2.4.: Single non-degenerate orbital at half-filling ($n = 1$). Left: At $U = 0$, a single band is filled producing a metallic state (delocalized electrons). Right: At $U > W$, two subbands emerge, the lower Hubbard band (LHB) and upper Hubbard band (UHB), producing a Mott insulator. For both panels, the horizontal axis is in units of energy.

Adding the two contributions we obtain

$$H_H = -t \sum_{\langle i,j \rangle, \sigma} c_{i\sigma}^\dagger c_{j\sigma} + U \sum_i \hat{n}_{i\uparrow} \hat{n}_{i\downarrow} \quad (2.5)$$

showing that effectively, the Hubbard model is governed by only two parameters. The first is the relative interaction strength U/t , or U/W , where W is the bandwidth $W = 2zt$ and z being the coordination number. The second relevant parameter is the electron density $n = N_e/N$ where N_e is the total number of electrons, and N is the number of lattice sites or unit cells.

At half-filling, *i.e.*, one electron per lattice site ($n = 1$), excursions of an electron from its site will produce a gain t in energy while paying an energy penalty of U for double occupancy. When considering the non-interacting limit ($U = 0$), there is one half-filled band with $2N$ states, recovering the metallic state of band theory. For $U > W$, electrons stay at their sites rendering the system insulating. Thus, the original band splits and gives rise to two *subbands*. The subbands are called *lower Hubbard band* (LHB) depicting states with $N - 1$ electrons (one hole) and *upper Hubbard band* (UHB) depicting states with $N + 1$ (one doublon).⁴ In this case, to create an electron-hole excitation, an energy gap of $E_g \sim U - W = U - 2tz$ must be overcome. This insulating state is called *Mott insulator*.

The energy gap in a Mott insulator plays a similar role as the energy gap between valence and conduction bands in standard insulators or semiconductors. Regardless of this similarity, the nature of this energy gap is very different, and it is borne from the electron-electron interaction instead of the periodic potential.

⁴The electron addition and removal spectra can be measured via inverse photoemission (IPES) and photoemission (PES) spectroscopy, respectively.

Moreover, metal-insulator transitions are usually linked to structural changes that reduce the bandwidth and switch from a metallic to insulating behavior. Also, the preference of antiferromagnetic ordering of the spins in the insulating state ($t \ll U$) can be argued from this simple model. Electrons have an energy gain of $J = 4t^2/U$ by performing virtual hopping (superexchange), which is only allowed for antiferromagnetic ordering since Pauli's exclusion principle blocks such virtual hopping for ferromagnetic order.

2.3. Mott-Hubbard and Charge-Transfer Insulators

In the previous section, a model for a single non-degenerate orbital was introduced. This model allows us to understand the phenomena observed in correlated electron systems in broad terms. However, transition-metal oxides are more complex than isolated ions, and the role of the ligand ions has to be taken into account. To make the discussion a bit more explicit, oxygen ions will be considered as ligands.

The inclusion of the O2p states leads to two different energies to be considered. The first is an excitation from one d orbital of a transition-metal ion to another one ($|d^n d^n\rangle \rightarrow |d^{n-1} d^{n+1}\rangle$) requiring an energy $\sim U$. The second is an excitation from an O2p orbital to a transition-metal ion d orbital ($|d^n 2p^6\rangle \rightarrow |d^{n+1} 2p^5\rangle$) requiring an energy Δ . By comparing the energy of both excitations, a material can be classified as (following [27]):

- If $U < \Delta$, upper panel in fig. 2.5, the excitation between two transition-metal ions ($|d_i^n d_j^n\rangle \rightarrow |d_i^{n-1} d_j^{n+1}\rangle$) is the lowest energy charge fluctuation which corresponds to an optical gap at an energy $\sim U$. This case corresponds to a *Mott-Hubbard* (MH) insulator and it is found on the left-hand side of the 3d elements, e.g., titanates and vanadates.
- If $U > \Delta$, lower panel in fig. 2.5, the excitation between a transition-metal ion and an oxygen ($|d^n p^6\rangle \rightarrow |d^{n+1} p^5\rangle$) is the lowest energy charge fluctuation which corresponds to an optical gap at energy Δ . This case corresponds to a *charge-transfer* (CT) insulator and it is common on the right-hand side of the 3d elements, e.g., nickelates and cuprates.

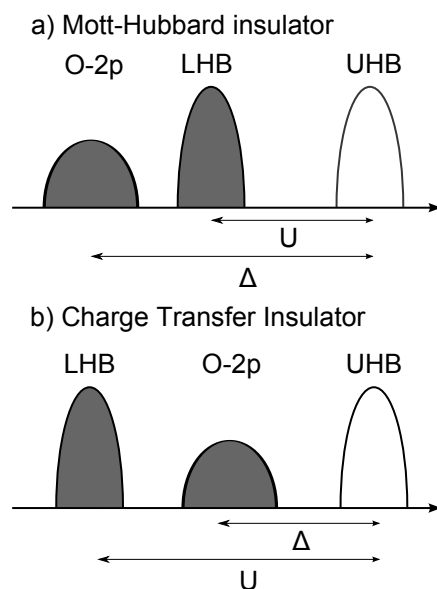


Figure 2.5.: Scheme of the electron addition (IPES) and electron removal spectra (PES) for (a) Mott-Hubbard (MH) and (b) charge-transfer (CT) insulators. LHB stands for Lower Hubbard Band, UHB for Upper Hubbard Band, and O-2p refers to the oxygen 2p band.

2.4. Spin-Orbit Coupling

As seen in the previous sections, many transition-metal compounds happen to be Mott insulators, where strong electron correlation suppresses low-energy charge dynamics. Nevertheless, there are still rich physics remaining that originate in the unquenched spin and orbital magnetic moments. In the case of Mott insulators where the relevant orbitals are of e_g symmetry, the angular momentum L of the ground state is quenched, for example, in manganites and cuprates. On the other hand, the threefold degenerate t_{2g} level shows an effective orbital angular momentum $L = 1$ leading to an intricate interplay between spin-orbit coupling and the superexchange interaction.

Spin-orbit coupling ($\lambda \mathbf{L} \cdot \mathbf{S}$) plays a significant role in atoms, mainly determining their multiplet structure. In a crystal, it can still play a significant role even when, due to the breaking of rotational symmetry caused by the crystal field, L and J are not good quantum numbers. How relevant the spin-orbit coupling is in a compound depends on the ratio between the spin-orbit coupling and the crystal-field splitting.

For most 3d transition-metal compounds, the role of spin-orbit coupling can be

treated as a weak perturbation because the crystal field splitting Δ_{CF} is considerably more significant. For example, a typical value of λ is of the order of 20 meV in Ti and 70 meV for Co. This perturbation leads to single-site and exchange magnetic anisotropy while also leading to possible anti-symmetric exchange interactions. Even when Δ_{CF} is usually much more significant than λ , the splitting of d levels due to distortions can be comparable with the spin-orbit coupling and thus affect them.

In 4d and 5d systems, the spin-orbit coupling is considerably stronger since the coupling scales as Z^4 , while the on-site Coulomb repulsion is significantly smaller. A stronger spin-orbit coupling leads to novel phenomena like Weyl semimetal, axion insulator, topological Mott insulator, and topological insulators [28].

2.5. Correlations and optics

Optical means are extremely powerful experimental techniques to study the electrodynamic response of correlated electron systems because the response of these systems to an electromagnetic wave gives key information about them. The interplay between localization and delocalization of electrons, which is at the core of these systems, is contained in electrons' behavior under the action of an electric field. Such an interaction between an electromagnetic wave and matter yields information in an energy range where elementary and collective modes can be found. A remarkable feature of correlated electron systems is that low-energy physics, in the meV range, can be probed by its influence at higher energy scales. An in-depth review of many experimental results of this can be found in [29].

In Mott insulators, the Coulomb interaction dominates, and electron motion is suppressed, which is seen as an energy gap in the optical spectra. Optical experiments show substantial deviations from what a conventional free-electron material shows upon doping or changes in temperature. This can be seen in fig. 2.6 where the optical conductivity for the layered cuprate compound $\text{La}_{2-x}\text{Sr}_x\text{CuO}_4$ is shown for different doping levels. In optics, a fundamental concept is the spectral weight, which depends on the number of states contributing to a given transition. In band insulators such as Si, the spectral weight for the excitation from the valence band to the conduction band is constant. If we dope Si by e_g , substituting P, a Drude peak appears but the spectral weight of excitations across the band gap is not affected.

In band insulators, the spectral weight is constant with a value of $2N$ for each band. In contrast, the number of states in a Hubbard subband is not constant and

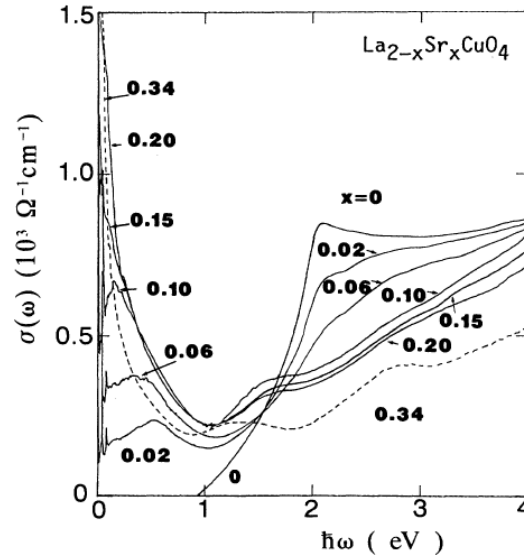


Figure 2.6.: Optical spectra of a layered cuprate ($\text{La}_{2-x}\text{Sr}_x\text{CuO}_4$) showing how upon doping it evolves from an insulator ($x = 0$) to a system with metallic characteristic. Note the change of spectral weight around 2.0 eV. Reproduced from [30].

depends on the number of electrons available. When the number of electrons changes, a redistribution of states between these subbands occurs. This explains why the spectral weight of excitations across the Mott gap is substantially reduced upon doping in $\text{La}_{2-x}\text{Sr}_x\text{CuO}_4$, see fig. 2.6.

Correlated electron systems are very susceptible to ordered states, making them especially suitable to be probed by optical means, particularly to study spin and orbital correlations and thus to ordering phase transitions or any symmetry-breaking phenomena. For example, YVO_3 is a compound that shows a spin- and orbital-ordering phase transition at around 77 K. At this temperature, the spin and orbital order of the system changes, allowing and prohibiting certain excitations in a given polarization due to the selection rules. This change is clearly seen in the optical spectra's substantial change, as shown in fig. 2.8 [31]. Particularly, when focusing on the c axis, the spectral features at low energies (~ 2 to 2.5 eV) are suppressed upon cooling below 77 K whereas at high energies (~ 3.8 eV), a peak in the optical conductivity emerges. This redistribution of spectral weight signals the spin and orbital ordering changes in YVO_3 , highlighting the power of optical methods and ellipsometry in particular. Via the selection rules, the temperature dependence also provides hints for the assignment of the observed features. Proceeding in a similar way, we will study the temperature dependence of excitations

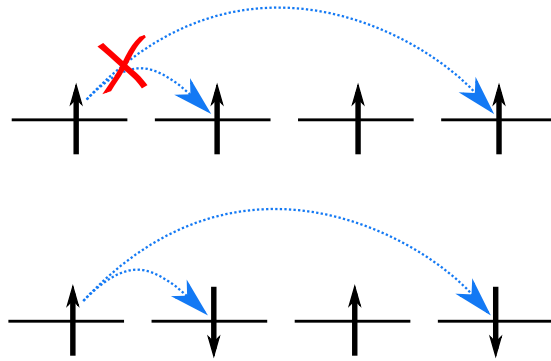


Figure 2.7.: Spin selection rules for inter-site excitations. a) for a ferromagnetically ordered system. b) for an antiferromagnetically ordered system.

across the Mott gap in Fe_3O_4 and Ca_2RuO_4 in chapters chapter 5 and chapter 6, respectively.

More specific introductions to the questions addressed in this thesis are given in the later chapters concerning each one of the systems studied.

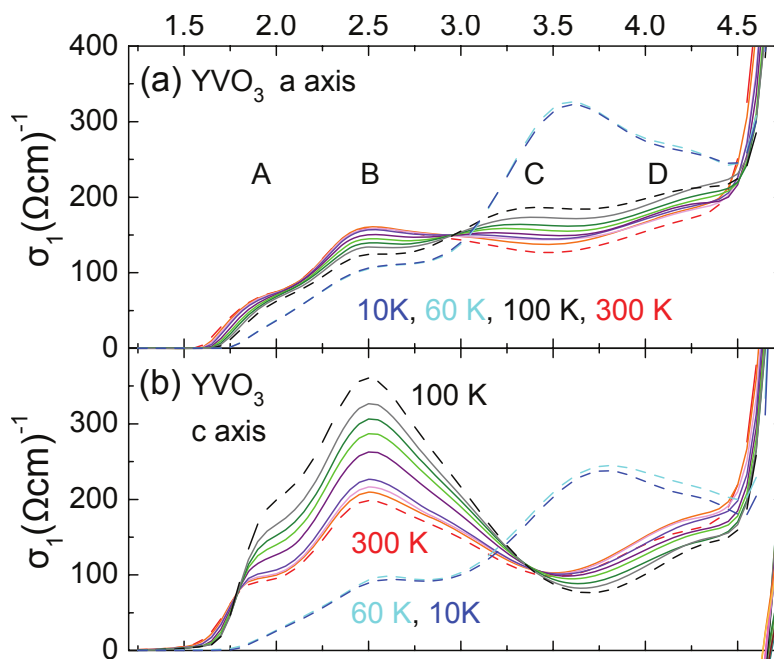


Figure 2.8.: The optical conductivity of YVO_3 shows the sensitivity of optical methods to spin and orbital phase transitions. Phase transitions can be detected by optical spectroscopy through a spectral weight redistribution due to changes of spin and orbital order which subsequently enhance or suppress excitations that can be observed given by the selection rules. Focusing on the c axis, the spectral features at low energies are suppressed while the ones at high energies become allowed when the sample enters the low-temperature phase below 77 K. Reproduced from [31].

3. Optical Spectroscopy

We have to remember that what we observe is not nature herself, but nature exposed to our method of questioning.

Werner Heisenberg

THE BASIC PRINCIPLE of optical spectroscopy is very simple and straightforward, to direct light onto a sample and see what goes through or gets reflected from it. Now, if optical spectroscopy were that simple, this chapter would not be needed. Written more formally, as defined by Dressel and Grüner [32], optical spectroscopy is the "*information gained from the absorption, reflection, or transmission of electromagnetic radiation, including models which account for, or interpret, the experimental results.*"

Ultimately, the objective of optical spectroscopy is to obtain the so-called *dielectric function* or, alternatively, the *optical conductivity*, which describes the optical properties of the sample. The dielectric function of a material contains contributions of many phenomena, e.g., lattice vibrations, electronic excitations, or magnetic excitations, among others. All these excitations can dramatically change the absorption spectra providing information about the electronic structure of the material.

Optical spectroscopy encompasses a broad energy range from $\sim 0.5 \times 10^{-3}$ eV in the far infrared (FIR) to 12 eV in the ultraviolet (UV). For convenience as well as for historical reasons, many different units are in use in spectroscopy. This broad range of energies is a great advantage, as it covers many single-particle and collective excitations present in solids.

Multiple instruments and techniques have to be employed to cover this broad range of energies due to sources and detectors' limitations. *Fourier transform infrared spectroscopy* (FTIR) is a well-established technique commonly able to meas-

Chapter 3: Optical Spectroscopy

	ω (cm ⁻¹)	E (eV)	Technique
Far infrared (FIR)	4–400	0.5×10^{-3} –0.05	F. Transform
Mid infrared (MIR)	400–4000	0.05–0.5	F. Transform & IR-Ellipsometry
Near infrared (NIR)	4000–12 500	0.5–1.5	Ellipsometry & F. Transform
Visible (VIS)	12 500–25 000	1.5–3.1	Ellipsometry
Ultraviolet (UV)	25 000–100 000	3.1–12	Synchrotron Radiation

Table 3.1.: Frequency and energy range for different segments of the optical part of the electromagnetic spectrum, accompanied by the preferred experimental technique to explore such region. Note that the limits of each segment are not a standard, but are a rough guideline to follow. Adapted from [33, 34].

ure from the far-infrared into the visible, and will be described in section 3.3. *Spectroscopic ellipsometry* can cover from near-infrared (NIR) into the UV in its most standard configuration and will be described in section 3.4. In the far-infrared, terahertz spectroscopy is nowadays widely available, whereas synchrotron radiation is used for the ultraviolet region.

First, we will review the basics of light-matter interaction to understand how we can learn about materials by using light in condensed matter physics. Then, we describe some key elements in the analysis of optical spectroscopy. Finally, the experimental techniques used for this work will be introduced, highlighting key elements of the theory and implementation details behind them. An introduction to optical spectroscopy covering basics, methods, and instrumentation in condensed matter physics can be found in references [33, 35, 36] and with considerably more depth in [32].

3.1. Light-matter interaction

When an electromagnetic wave encounters a medium, matter responds to it by creating electric dipoles, magnetic moments, polarization charges, induced currents, and others, thus modifying the electromagnetic field within the material.¹ The interaction between light and matter can be highly complex, and here we

¹There are two processes involving electrons and light: dispersion and dissipation. From a macroscopic point of view, the first has to do with a change in the propagation speed of light in the material (n) while the second with absorption (k). From a microscopic point of view, what is known as the dielectric function ϵ is a better quantity to describe the properties of a solid. As it will be shown later, both descriptions are equivalent.

3.1 Light-matter interaction

will assume a linear response² to the electric field vector \mathbf{E} . Thus, the response³ of matter at position \mathbf{r} and time t when interacting with an electromagnetic wave given by $\mathbf{E}(\mathbf{r}', t')$ at position \mathbf{r}' and time t' is given by

$$D_i(\mathbf{r}, t) = \int \int \varepsilon_{ij}(\mathbf{r}, \mathbf{r}', t, t') E_j(\mathbf{r}', \mathbf{t}') dt' d\mathbf{r}' \quad (3.1)$$

where i and j refer to the vector components of the electric field \mathbf{E} and displacement field \mathbf{D} . Here, ε_{ij} is the *complex dielectric tensor* which encodes the response of matter to the electromagnetic wave. Ultimately, the complex dielectric tensor summarizes the optical properties of matter.

For most solids, two simplifying assumptions can be considered.

1. assuming a homogeneous solid and for wavelengths much bigger than the lattice constants, the spatial response depends only on $\mathbf{r} - \mathbf{r}'$.
2. assuming that the Hamiltonian does not depend explicitly on time, the time response depends only on $t - t'$.

By using these two considerations, equation (3.1) reduces to

$$D_i(\mathbf{r}, t) = \int \int \varepsilon_{ij}(\mathbf{r} - \mathbf{r}', t - t') E_j(\mathbf{r}', \mathbf{t}') dt' d\mathbf{r}'. \quad (3.2)$$

Taking the Fourier transform in space and time of equation (3.1)

$$D_i(\mathbf{q}, \omega) = \varepsilon_{ij}(\mathbf{q}, \omega) E_j(\mathbf{q}, \omega) \quad (3.3)$$

the response takes a wavevector \mathbf{q} , and frequency ω dependence. Equation (3.3) shows that the response of matter is dependent on the frequency, and all frequencies are independent of one another. It also shows that the response happens at the same frequency as the one from the applied external field.⁴ Both of these facts

²There are some fascinating phenomena when higher orders of \mathbf{E} and \mathbf{B} are considered. These usually play a role when the intensity of the light $\propto E^2$ is very high, as encountered in highly focused laser light.

³The response can be described by many equivalent ways: polarization \mathbf{P} , current \mathbf{J} , or displacement vector \mathbf{D} , each having a different but related representation and physical meaning.

⁴Due to the linearity of the response when considering an oscillating electric field of the form

$$\mathbf{E}(\mathbf{r}, t) = \mathbf{E}_0 \exp[i(\mathbf{q} \cdot \mathbf{r} - \omega t)] \quad (3.4)$$

the response happens at the same frequency as the one from the applied field. This can be

are at the core of the power of optical spectroscopy.

Since the wavelength of the electric field is large compared to the lattice spacing⁵, and since the wave vector is inversely proportional to the wavelength, we are restricted to probe close to $q = 0$. In other words, the effect is local. This locality is paramount in condensed matter physics as it plays a role in the selection rules of optical transitions. Thus, we can drop the explicit wave vector dependence of our equations.

For example, we can also simplify and consider isotropic media, reducing our second rank tensor $\varepsilon_{ij}(\omega)$ to a scalar function $\varepsilon(\omega)$ called *complex dielectric function*

$$D(\omega) = \varepsilon(\omega)E(\omega). \quad (3.5)$$

Now the question is how to go from something that we can measure in a laboratory to the response function. This will be covered in sections 3.3 and 3.4 when discussing the particular experimental techniques used. For now, we will continue exploring some other essential elements⁶, which will give us tools to answer this question.

3.1.1. Optical constants

Once equipped with the dielectric function, other optical properties can be defined. There are many equivalent ways to describe the interaction of light and matter. An alternative one is by using a frequency-dependent version of Ohm's law given by

$$j(\omega) = \sigma(\omega)E(\omega) \quad (3.6)$$

where σ is the optical conductivity. Both descriptions are analogous, and one can

evidenced by the Fourier transform of equation 3.1.

⁵A typical value for visible light is 10^5 cm^{-1} . In contrast, the Brillouin zone extends typically for about 10^8 cm^{-1} .

⁶Until now, no mention to the magnetic field of the electromagnetic wave has been discussed. Most materials couple very weakly to the magnetic field; this is the case for the materials investigated in this thesis. This means that magneto-optical effects can be ignored and assume that $\mu_r = 1$.

3.1 Light-matter interaction

go from one to the other by the following transformation

$$\frac{4\pi i}{\omega} \sigma(\omega) = \varepsilon(\omega) - 1, \quad (3.7)$$

Furthermore, an extra set of optical constants commonly used is the complex refractive index N

$$N(\omega) = \sqrt{\varepsilon(\omega)} = n + ik, \quad (3.8a)$$

$$n = \frac{1}{2} \left(\varepsilon_1 + \sqrt{\varepsilon_1^2 + \varepsilon_2^2} \right)^{1/2}, \quad (3.8b)$$

$$k = \frac{1}{2} \left(-\varepsilon_1 + \sqrt{\varepsilon_1^2 + \varepsilon_2^2} \right)^{1/2}, \quad (3.8c)$$

where n is the refractive index and k is the extinction coefficient.

If the reflectivity (R) and the transmittance (T) of a sample can be measured⁷, then to obtain ε or σ is straightforward since R and T are functions of n and k , and thus of ε (see eq. (3.8)).

$$T(\omega) = \frac{(1 - R(\omega))\Phi}{1 - (R(\omega)\Phi)^2}, \quad (3.9a)$$

$$R(\omega) = \frac{(n(\omega) - 1)^2 + k^2(\omega)}{(n(\omega) + 1)^2 + k^2(\omega)}, \quad (3.9b)$$

$$\Phi(\omega) = e^{-2\omega k(\omega)d/c}, \quad (3.9c)$$

where d is the sample thickness, c the speed of light in vacuum. Furthermore, if $k \ll n$, a simplification for the reflectivity can be achieved as

$$R(\omega) = \frac{(n(\omega) - 1)^2}{(n(\omega) + 1)^2} \quad (3.10)$$

⁷Experimentally, we cannot measure the exact same sample. Equation eq. (3.9b) is valid for a semi-infinite sample to avoid contributions from the back side of the sample. Whereas equation ?? assumes finite thickness.

3.1.2. Kramers-Kronig relations

Due to causality, there cannot be an absorption before the beginning of the experiment. This means that the real and imaginary parts of a response function, *e.g.*, ε or σ , are not independent of each other, see fig. 3.1. Both quantities are related through what is known as a Kramers-Kronig relation [32]. Considering the response function $\varepsilon = \varepsilon_1 + i\varepsilon_2$, the real and imaginary parts are related as follows

$$\varepsilon_1(\omega) = 1 + \frac{2}{\pi} \mathcal{P} \int_0^{\infty} \frac{\omega' \varepsilon_2(\omega')}{\omega'^2 - \omega^2} d\omega', \quad (3.11a)$$

$$\varepsilon_2(\omega) = -\frac{2}{\pi\omega} \mathcal{P} \int_0^{\infty} \frac{\omega'^2 [\varepsilon_1(\omega') - 1]}{\omega'^2 - \omega^2} d\omega', \quad (3.11b)$$

where \mathcal{P} is the principal value of the integral. Ultimately, the absorption at a frequency ω implies that a shift in the phase at other frequencies (ω') is required not to violate causality. The reverse also holds, a change in the phase at a specific frequency necessarily is connected to an absorption.

Kramers-Kronig analysis is a powerful tool, but it also provides some challenges. As shown in the previous equation, knowing the full spectrum of ε_2 , from 0 to ∞ is needed to construct the real part of the dielectric function. Experimentally, it is not possible to know the full absorption spectrum of a sample. This means that an extrapolation to low and high frequencies has to be made. This step is critical to the whole procedure and may generate errors, affecting particularly close to the measured frequency window's borders.

Similar expressions can be found for other response functions or derivations like the reflectivity $R(\omega)$. This is the main ingredient to obtain the real part of the optical conductivity σ_1 from reflectivity measurements performed with a Fourier spectrometer, as explained in the section 3.3.

3.1.3. Oscillators

To describe the features observed in optical spectroscopy, different functions describing the dielectric function are used. The absorption features can be described by various lineshapes, whose shape can provide some information about the nature of the absorption in question.

3.1 Light-matter interaction

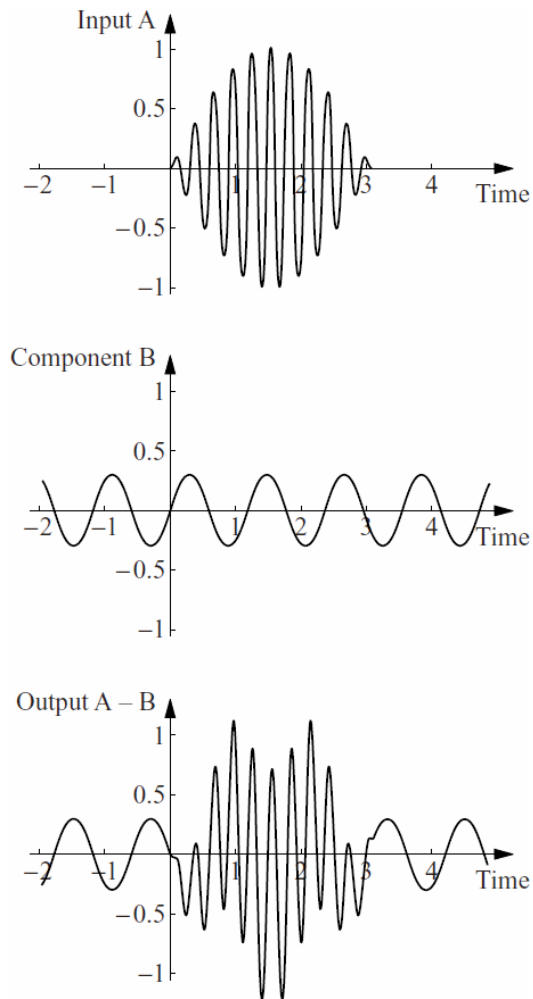


Figure 3.1.: Top: A wave packet existing for $t > 0$ as input A. Such a wave packet is formed by many Fourier components. Middle: One such component is B, which extends in time from $-\infty$ to ∞ . Bottom: If such component B is subtracted from input A, the result would be an output containing contributions for $t < 0$, which would violate causality. To mend this situation, the phases of all other Fourier components change. Thus the absorption at a certain frequency is linked to the phase at all other frequencies, which is encoded in the Kramers-Kronig relations given in equations (3.11). Reproduced from [32].

Chapter 3: Optical Spectroscopy

The most standard lineshape to describe an excitation is a Drude-Lorentz one. It comes naturally when considering a bound charge driven by an external electric field in a harmonic potential, and can be used to describe free electrons in a metal or bound electrons in insulators.

The definition of a Drude-Lorentz oscillator is given by

$$\epsilon^{DL} = 1 + \frac{4\pi N e^2}{m} \frac{1}{\omega_0^2 - \omega^2 - i\omega\gamma} \quad (3.12)$$

where N is the effective number of electrons, e the electron charge, m the electron mass, ω_0 the center frequency, and γ the damping. Separating in real and imaginary parts one obtains

$$\epsilon_1(\omega) = 1 + \frac{\omega_p^2(\omega_0^2 - \omega^2)}{(\omega_0^2 - \omega^2)^2 + \omega^2\gamma^2}, \quad (3.13a)$$

$$\epsilon_2(\omega) = \frac{\omega_p^2\omega/\tau}{(\omega_0^2 - \omega^2)^2 + \omega^2\gamma^2}, \quad (3.13b)$$

$$\omega_p^2 = \frac{4\pi N e^2}{m} \quad (3.13c)$$

When considering unbound charged particles as in the case of metals, $\omega_0 = 0$, and in such case, it is called Drude oscillator⁸.

Even when the Drude-Lorentz oscillator is pervasive and a good descriptor of many physical phenomena, nature is not so simple. Factors like instrumental function, bandgap, coupling to a continuous background, and interactions can strongly influence the lineshape of an excitation. This leads to the introduction of other lineshapes. The most common ones are the Gaussian and Tauc-Lorentz oscillators.

In the case of the Gaussian lineshape, the imaginary part (ϵ_2) is defined as follows [37]

$$\epsilon_2^G(\omega) = A e^{-4 \ln 2 \left(\frac{\omega - \omega_0}{\sigma}\right)^2} - A e^{-4 \ln 2 \left(\frac{\omega + \omega_0}{\sigma}\right)^2} \quad (3.14)$$

where A , ω_0 , and σ are the amplitude, peak frequency, and full width at half maximum, respectively. Note that the second term produces an inverted Gaussian

⁸In the Drude and Lorentz lineshapes, an explicit analytical description of the full dielectric function is available, but this is not the general case.

at $-\omega_0$, thus outside of the physical range. The introduction of such a term is needed to assure that causality is not being violated. The real part (ε_1) is defined to be Kramers-Kronig consistent as follows

$$\varepsilon_1^G(\omega) = \frac{2A}{\sqrt{\pi}} \left[D\left(2\sqrt{\ln 2} \frac{\omega + \omega_0}{\sigma}\right) - D\left(2\sqrt{\ln 2} \frac{\omega - \omega_0}{\sigma}\right) \right] \quad (3.15)$$

where D is the Dawson function⁹.

Another useful lineshape is the Tauc-Lorentz [38]. This lineshape provides a generalization to the Lorentz one and allows for asymmetric lineshapes, thus being able to account for, *e.g.*, a bandgap.

$$\varepsilon_2^{TL}(\omega) = \frac{A\omega_0\gamma(\omega - \omega_g)^2}{(\omega^2 - \omega_0^2)^2 + \gamma^2\omega^2} \frac{\Theta(\omega - \omega_g)}{\omega} \quad (3.16)$$

where A , ω_0 , and γ are the amplitude, peak frequency, and damping constant, respectively, as for the Lorentz model. The new parameter ω_g is the bandgap frequency, and Θ is the Heaviside function yielding a value of $\varepsilon_2^{TL} = 0$ for frequencies below the bandgap. The real part of the dielectric function is obtained through a Kramers-Kronig transformation [38]. Compared to the Lorentz or Gaussian lineshapes, the Tauc-Lorentz lineshape has the drawback of needing an extra parameter.

The imaginary part of the dielectric function of the three previously described oscillators is shown in fig. 3.2. We can observe how the Gaussian oscillator (left) contributes mainly around the center and rapidly goes to 0. In this case, with $\sigma = 0.5$ eV, at a distance of 1 eV from the center the contribution is already marginal. In contrast, the Lorentz oscillator (middle) shows a broader contribution with a softer decay. In this example, there is still a considerable contribution to ε_2 for energies which are about 1.5 eV above the peak frequency. On the other hand, the Tauc-Lorentz oscillator (right) shows how the extra parameter can introduce a strong asymmetry in the lineshape. Here, ε_2 sharply goes to 0 on the left of the center reaching it at $\omega_g = 1.5$ eV whereas, towards the right, it extends considerably.

Beyond oscillators, other types of contributions can be included in modeling the optical response of a material. One such contribution is ε_∞ , which is a constant real value and accounts for high-energy contributions to ε_1 . Poles are con-

⁹The Dawson function is defined as $D(x) = e^{-x^2} \int_0^x e^{t^2} dt$.

Chapter 3: Optical Spectroscopy

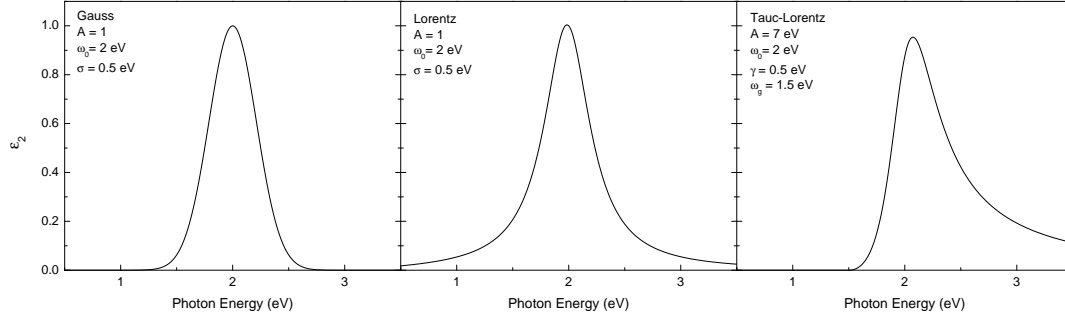


Figure 3.2.: Comparison of the imaginary part of the Gauss, Lorentz, and Tauc-Lorentz oscillators. For the Lorentz oscillator, A corresponds to ω_p^2 in eq 3.13. The parameters for each oscillator are indicated in the plot.

tributions to ε_1 of excitations far outside the measured range, providing some dispersion in ε_1 . Their functional form is given by

$$\varepsilon_1^{pole}(\omega) = \frac{A}{E_n^2 - E^2} \quad (3.17)$$

where A is the magnitude in eV^2 and E_n is the energy position of the pole.

An optical model can be built by using a combination of oscillators and other contributions. Building models is a significant step in analyzing Fourier transform spectroscopy and spectroscopic ellipsometry, as will be described in their respective sections. In this model building process, care must be taken to keep the constructed and then fitted model physical. Since, in most cases, the parameters in oscillators are linked to physical processes, by building a model, one can estimate some microscopic information about the sample under study.

An optical model is given by the sum of lineshapes and other contributions as follows

$$\varepsilon(\omega) = \varepsilon_\infty + \varepsilon_{Drude} + \varepsilon_{poles} + \sum \varepsilon_{Lorentz} + \sum \varepsilon_{Gauss} + \dots \quad (3.18)$$

where ε_∞ is a real value that accumulates all the high-energy contributions to ε_1 .

3.2. Sample preparation

In studying crystals, it is vital to know their crystallographic orientation before doing a measurement. The orientation of a sample is achieved by the x-ray Laue

method. Once oriented, the sample can require cutting to provide the oriented surface. In some fortunate cases, the crystal can be readily cleaved to expose a well-defined surface.

Once cut and oriented, the sample is lapped down and polished to obtain a uniformly flat and smooth surface as required in optical methods. To lap the sample, a cast iron plate is used together with an aluminum oxide water suspension of $3\ \mu\text{m}$ sized particles. Lapping a sample is also used to thin out samples for transmission measurements when required. After the lapping procedure, the sample is polished to obtain a smooth and shiny surface. This is important since, after lapping, the surface is coarsely grained, producing strong scattering and losing specularly reflected light. A plate made of polyurethane foam is used together with a fine colloidal suspension of SiO_2 of $0.032\ \mu\text{m}$ in water. For transmission measurements, both sides of the sample have to be polished, whereas, for reflectivity-based measurements, only one side is needed. The plate is placed on a Logitech PM2 machine in both cases, which rotates it at a constant speed up to 50 rpm.

After lapping and polishing, the sample is transferred to a sample holder. In most cases, silver paste is used to glue the sample due to good thermal conductivity. When doing transmission measurements, the sample holder contains an aperture to let the light go through. The aperture size has to be the same for the reference and sample.

3.3. Fourier spectroscopy

Fourier transform spectroscopy is a very versatile technique to investigate the optical properties of materials. Nowadays, it is a well-established technique in many areas of physics, chemistry, environmental sciences, and industry¹⁰. In-depth descriptions are readily available [33, 39, 40], thus we are going to focus on the basic principles of Fourier transform spectroscopy.

At its core, Fourier spectroscopy is an interferometric technique. A detailed scheme of the Bruker IFS 66v instrument's experimental setup used in the laboratory is shown in fig. 3.3. Using a Michelson interferometer, the white light from a source is separated in two and then merged with the addition of time-dependent path difference through a moving mirror. After the production of the interference

¹⁰Outside the laboratory, uses of Fourier spectroscopy can be found in diverse areas, for example, food processing, quality control, pharmaceuticals, and forensics. There are even devices small enough to be used in the field.

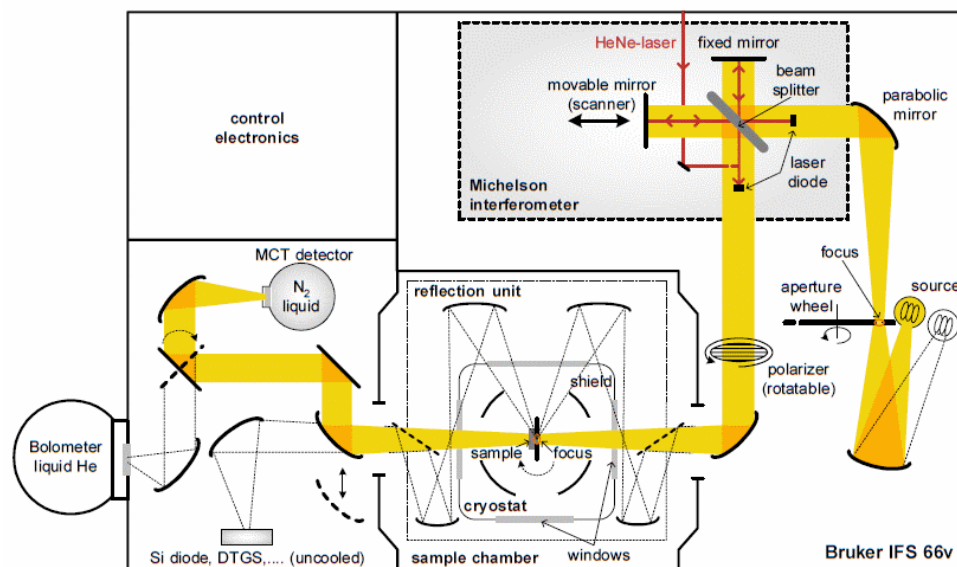


Figure 3.3.: Fourier transform IR setup. Light from the source is directed to the Michelson interferometer. Later the beam goes through a polarizer and is focused onto the sample. Afterwards, the light is collected and directed into the detector. Reproduced from [41].

pattern¹¹, the light is optionally polarized and then focused onto the sample/aperture. The transmitted light is then collected and focused onto a detector where the interferogram is recorded. Once the interferogram is obtained, a Fourier transform is applied to obtain the intensity spectra. The following ratios then give the transmittivity/reflectivity

$$T(\omega) = \frac{S_s^t(\omega)}{S_r^t(\omega)}, \tag{3.19a}$$

$$R(\omega) = \frac{S_s^r(\omega)}{S_r^r(\omega)} \tag{3.19b}$$

where S_s , and S_r are the sample and reference spectra, respectively, and the superscripts t and r refer to the transmitted and reflected cases.

This technique provides two significant advantages when compared with dispersive spectroscopic techniques that use a grating monochromator. The first one is called Fellgett or multiplex advantage, amounting to an improvement of the

¹¹Effectively performing a physical Fourier transform! Thus the name of the technique.

signal-to-noise ratio (SNR) through an increased number of measurements in a given time interval compared to dispersive methods. An amount of N independent measurements can be done at the same time interval that would take for a dispersive technique to measure one single spectrum consisting of N frequency intervals. This leads to an improvement of the SNR on the order of \sqrt{N} . The second advantage, called Jacquinot or throughput advantage, stems from the fact that no narrow slit is needed, but circular apertures can be used leading to less light intensity being lost. This increases the light intensity reaching the sample and detector. This is particularly critical in frequency regions where the light sources have very low intensity, like in the far-infrared. Both together also imply a reduction in acquisition time. Other advantages are an excellent frequency calibration and a very high resolution of the order of 0.01 cm^{-1} .

However, not everything is so perfect in experimental physics. There are two main disadvantages to FTIR. The first one is that it requires a reference measurement, namely an open aperture for transmission, or, *e.g.*, gold surface for reflection. Since reference and sample cannot be measured simultaneously, having to measure twice implies that drifts in the light sources' output, particularly for long measurements, can introduce errors in the acquired spectra. The second disadvantage is that when reflection and transmission cannot be obtained, Kramers-Kronig analysis is employed. This limits the measurements' sensitivity due to possible artifacts introduced through the extrapolations performed in the Kramers-Kronig process, as discussed in section 3.1.2.

Once the reflectivity is measured, we want to extract the dielectric function, and for that, we have two options. The first one is to use a Kramers-Kronig analysis. For this, we take a more general expression [42] than equation 3.9b

$$\sqrt{R(\omega)}e^{i\phi_r(\omega)} = \frac{1 - \sqrt{\varepsilon(\omega)}}{1 + \sqrt{\varepsilon(\omega)}} \quad (3.20)$$

where $\phi_r(\omega)$ is the phase shift experienced by the electromagnetic wave upon reflection. In reflectivity, the value of the phase is lost since the employed detector can measure only the intensity of the light but it can be reconstructed by using the following Kramers-Kronig formula

$$\phi_r(\omega) = -\frac{2\omega}{\pi}P \int_0^\infty \frac{\ln \sqrt{R(\omega')}}{\omega'^2 - \omega^2} d\omega' \quad (3.21)$$

As seen in section 3.1.2, the use of the Kramers-Kronig relations means a know-

ledge of the full spectrum. Since this is not possible, extrapolations to low and high frequencies are used.

The second option is to build an oscillator model that can be used to fit the reflectivity derived from it to the measured reflectivity. Alternatively, a combined strategy can be employed, where the oscillator fit is used to provide the extrapolations for the Kramers-Kronig analysis.

3.3.1. Setup and measurement

The spectrometer used is a Bruker IFS 66/v, and its scheme is shown in fig. 3.3. The set of detector, polarizer, cryostat windows, beam splitter, and lamp were chosen to maximize the signal in the mid-infrared range 0.2 eV to 1.1 eV.

Liquid nitrogen cooled MCT (HgCdTe) detector with a proper calibration was used. The spectrometer is maintained at approximately 10 mbar throughout the measurements. Also, it is continuously being flushed with N_2 to reduce the absorption lines of common elements in air.

The sample is placed into a He-flow cryostat, with a temperature range from about 4 K to 500 K and with a 0.1 K temperature stability. The cryostat pressure is kept below 10^{-5} mbar to avoid the build-up of ice on the surface of the sample as it could produce artifacts like interference fringes on the acquired spectra.

The sample and aperture are placed on the same axis but might have slightly different positions. First, the sample is measured and immediately after the reference is measured under the same experimental conditions. For each measurement, the vertical and horizontal positions, together with the azimuthal angle, are optimized to obtain the maximum intensity at the detector.

3.3.2. Spins, phonons, and light: bimagnon-plus-phonon absorption

Since in chapter 4 we will be concerned with magnetic excitations, the question is what and how can we learn from these low-dimensional quantum spin systems with infrared spectroscopy. To a first approximation, only electric-dipole-allowed excitations are probed by optical spectroscopy. Thus, we have to find a way to study the spin-spin correlation function by measuring the dipole-dipole correlation function. A magnetic excitation, or spin-flip, has $\Delta S^z = 1$. Spin conservation in optical spectroscopy implies that $\Delta S^z = 0$ has to be fulfilled. This means that

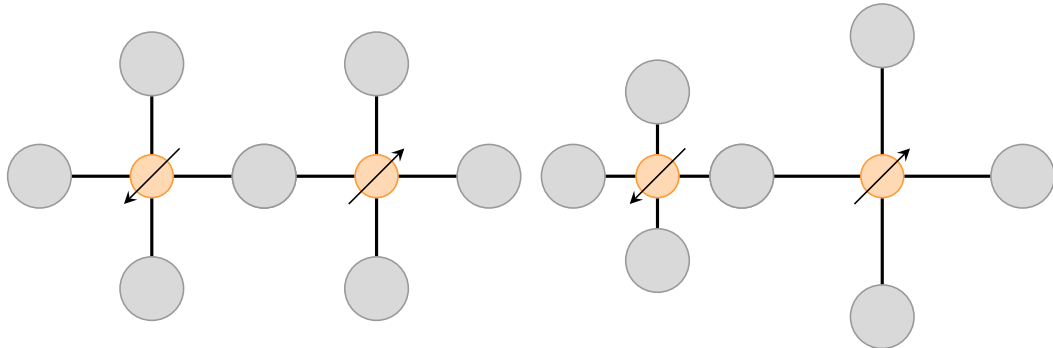


Figure 3.4.: Local (planar) environment of the spins in 2D cuprates. Small orange circle is copper, and big gray circle is oxygen. Left: The structure is inversion symmetric upon spin exchange. Right: Bond-stretching phonon breaks the symmetry, and IR absorption becomes weakly allowed.

the optical excitation of a single magnetic excitation is not possible¹², and spin degrees of freedom are not directly accessible by linearly polarized light.

Due to the presence of an inversion center in the tetragonal structures of cuprates, as shown in fig. 3.4 (left), an asymmetric displacement of charge is not possible in this material and, thus, no electric dipole to couple to and observe. One alternative to circumvent this limitation and fulfill the optical selection rule, is to have two magnetic excitations with a total spin of zero involved in the process. When a general Hamiltonian, including lattice and spin degrees of freedom coupling to an electromagnetic field, is considered, the Taylor expansion at second order in the ion's displacement and the electric field produces spin-dependent effective dipole moments terms [43]. Thus, the observation of magnetic excitations employing FTIR in this class of materials is then possible by the simultaneous excitation of two elementary magnetic excitations plus a bond-stretching symmetry breaking phonon [44]. This mechanism is commonly referred to as *bimagnon-plus-phonon absorption*¹³. The phonon breaks the symmetry along the Cu-O-Cu bond (fig. 3.4 right), such that the exchange of two spins now creates a weak effective dipole moment, thus making the whole process infrared active.

As it will be discussed in chapter 4, this approach has been particularly successful in describing magnetic excitations in spin chains [45, 46] and 2-leg ladders [47].

¹²This is the case when neglecting spin-orbit coupling.

¹³The name is slightly misleading because the magnetic excitation changes in character depending on the dimensionality of the system, but calling it double-"magnetic excitation"-plus-phonon would be too cumbersome.

The simultaneous excitation of a phonon has some consequences. Besides breaking the symmetry, it adds momentum and an energy shift to the process. Since the photon transfers almost no momentum, and because of momentum conservation, $k_{total} \sim 0$ and $k_{total} = k_{ph} + k_{m_1} + k_{m_2}$. This means that the two magnetic excitations are created with arbitrary momentum, and since k_{ph} covers the whole Brillouin zone, the observed absorption is a weighted average over the Brillouin zone. Due to energy conservation, the energy scale will be shifted as the phonon also carries energy. Since only optical phonons are involved in this process, it is safe to consider dispersionless phonon modes, and the shift considered is $\hbar\omega_{ph}$.

3.4. Spectroscopic ellipsometry

Spectroscopic ellipsometry (SE) is a very sensitive method to determine the optical constants of materials. This technique particularly excels in studying and characterizing thin films and has wide applications in areas like semiconductors, chemistry, and real-time monitoring of PVD, CVD, and MBE growth processes. A selection of various books covering ellipsometry in great depth can be found in the following references [48–50]. Here the basic principles behind ellipsometry will be described, with a focus on bulk materials.

The core strength of ellipsometry resides in being able to measure two independent quantities simultaneously. Having two measured quantities amounts to be able to determine the full dielectric function in the measured energy range without resorting to extrapolations as required for a Kramers-Kronig analysis, as seen in section 3.1.2. The price to pay is that, in a general case, there is no invertible relationship between the measured quantities and the optical constants of the material. This means that building an optical model is a necessary and critical step for interpreting the measured data. However, since the two measured quantities are physically related, as shown in section 3.1.2, a strong constraint is placed to model the optical properties. A second advantage is that ellipsometry is a self-normalizing technique, which removes the need for a reference sample and issues related to fluctuations in the light source.

Ellipsometry has two general restrictions, one related to the surface roughness, and another to the light beam's angle of incidence. The sample's surface roughness has to be small since the light scattering produced by it strongly reduces the reflected intensity, making it challenging to determine the polarization state. When the surface roughness's size exceeds about 30% of the wavelength being

measured, the error increases considerably. In ellipsometry, the measurement has to be performed at an oblique angle¹⁴ because close to normal angle of incidence, it becomes tough to distinguish between p- and s- polarizations since they become the same for normal incidence (see ??). Despite these restrictions, spectroscopic ellipsometry can achieve excellent quantitative results.

3.4.1. Ellipsometric angles

First, we need to describe the polarization state of the electromagnetic wave. We can split the electric field vector into two components, parallel ($\mathbf{E}_{i,r}^p$) and perpendicular ($\mathbf{E}_{i,r}^s$) to the plane of incidence. Figure 3.5 shows the basic geometry of how the physics behind ellipsometry works for fixed photon energy. A linearly polarized wave with amplitude \mathbf{E}_i and wave vector \mathbf{k}_i impinges on the surface of the sample under study. Upon reflection, a wave with field amplitude \mathbf{E}_r emerges with the same wave vector magnitude ($|\mathbf{k}_r| = |\mathbf{k}_i|$) but with a different amplitude and polarization state.

Ellipsometry measures the ratio of amplitudes (Ψ) and the relative phase difference (Δ) between the parallel and perpendicular components of the reflected electromagnetic wave. The incidence angle is usually close to the Brewster angle¹⁵, because there we find the maximal difference between the Fresnel coefficients for parallel (r_p) and perpendicular (r_s) components.

The ratio between reflected and incident field amplitudes for p- or s- polarization are called Fresnel coefficients and are given as

$$\frac{E_p^r}{E_p^i} = r_p(\varepsilon_{air}, \varepsilon_{bulk}; \theta) \quad (3.22a)$$

$$\frac{E_s^r}{E_s^i} = r_s(\varepsilon_{air}, \varepsilon_{bulk}; \theta). \quad (3.22b)$$

In the most simple case of a bulk sample in air, they are a function of the corresponding dielectric functions and the angle of incidence. Fresnel coefficients are complex quantities, which can be written in polar form as

¹⁴In contrast to Fourier transform spectroscopy where the angle of incidence can be normal for transmission and almost normal, about 11° , for reflection measurements.

¹⁵The Brewster angle depends on the frequency of light $\Theta_B = \Theta_B(\omega)$.

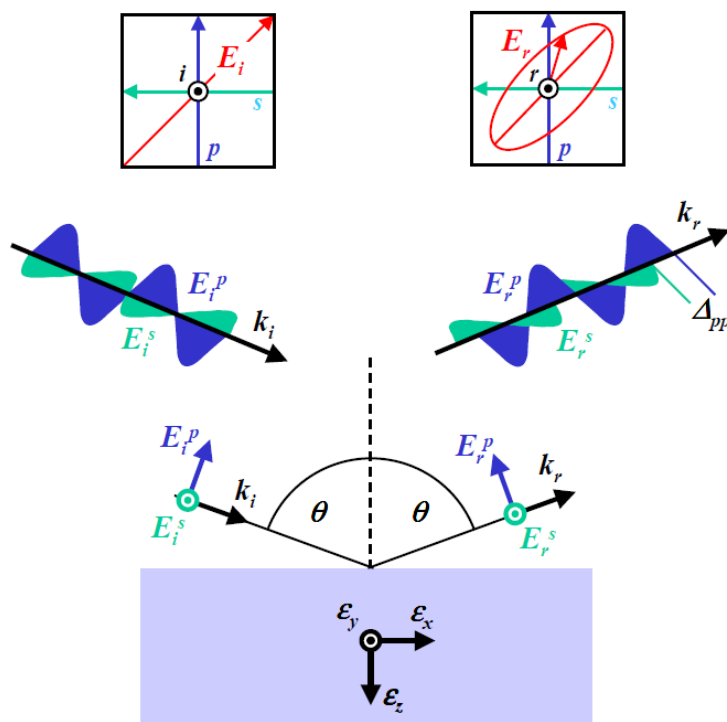


Figure 3.5.: Ellipsometry consists, in its most basic setup, of linearly polarized light that interacts with the surface of the sample with the reflection being measured. Due to the interaction, the polarization state changes depending on the optical properties of the sample. In the general case, the polarization's elliptical state is obtained because of a change in the amplitudes and a delay of one component of the polarization relative to the other. Reproduced from [51].

$$r_p = |r_p| e^{i\delta_{rp}} \quad (3.23a)$$

$$r_s = |r_s| e^{i\delta_{rs}} \quad (3.23b)$$

where it is clear that upon reflection an attenuation and phase delay are introduced. The connection between the so-called ellipsometric angles Ψ and Δ and the physical properties of a sample, namely the Fresnel coefficients, is given by

$$\rho = \frac{r_p}{r_s} = \tan \Psi e^{i\Delta} \quad (3.24)$$

Using the polar representation given in equations (3.23) one obtains

$$\tan \Psi = \frac{|r_p|}{|r_s|} \quad (3.25a)$$

$$\Delta = \delta_{rp} - \delta_{rs} \quad (3.25b)$$

which means that Ψ and Δ are the ratios of the electric field amplitudes and phase difference between the reflected p- and s-polarizations.

Naively, one can consider the bulk sample under investigation to be infinite and isotropic. In this particular case, a direct inversion from the ellipsometric angles (Ψ, Δ) to what is called the pseudo-dielectric function $\langle \varepsilon \rangle$ is possible and given as

$$\langle \varepsilon \rangle = \sin^2 \theta \left[1 + \left(\frac{1 - \rho}{1 + \rho} \right)^2 \tan^2 \theta \right] \quad (3.26)$$

where θ is the angle of incidence and ρ is defined as in equation (3.24) [52]. Since we are interested in the samples' bulk properties, we could stop here as is commonly done.

However, we know that the bulk-air interface is not perfectly flat, or the material can have some anisotropy. Both of these cases cannot be described by such a simple analysis as given by equation (3.26), leading to erroneous results. Thus, a more sophisticated analysis method is presented later on in section 3.4.3.

3.4.2. Setup and measurement

The ellipsometer used throughout the measurements is a J.A. Woollam VASE unit, corresponding to a *rotating analyzer ellipsometer*. It consists of three main units: monochromator unit, and the source and detector arms, as shown in fig. 3.6. Multiple angles of incidence, in the range 20° to 90° can be measured by rotating the sample stage and the detector arm.

The light is provided by a single source, a broad-band Xenon lamp, located in the monochromator unit. The monochromator unit also hosts two reflection (Czerny-Turner) gratings to perform the chromatic dispersion, which later is focused on the exit slit and delivered to the source arm of the ellipsometer through an optical fiber.

At the source arm, an initial linear polarizer is used to select a particular polarization state. Then the autoretarder, consisting of a computer-controlled MgF_2 Berek waveplate, turns the linear state into an elliptical one. After interaction with the sample, the light beam goes to the detection arm. The detection arm contains a constant speed rotating analyzer and two detectors, a Si diode and an InGaAs photodiode covering two distinct energy ranges. Through the parameters of a fit of the modulated intensity, the values of Ψ and Δ are extracted.

The introduction of an autoretarder obeys the following rationale. If the reflected light is nearly linearly polarized, the ellipsometer has very low precision. This happens when Δ is close to 0 or 180° . An autoretarder allows a higher level of accuracy by avoiding this situation and allowing the ellipsometer to differentiate between $\Delta = \delta$ and $\Delta = 360^\circ - \delta$.

To perform temperature-dependent measurements, the setup is equipped with a KONTI flowing Helium cryostat manufactured by Cryovac and kept in UHV conditions to reduce the build-up of absorbates, which strongly affect the measured properties of the sample. This cryostat is capable of attaining temperatures ranging from 12 K to 500 K. The temperature accuracy at the sample is ± 1 K with a stability better than 0.2 K throughout a measurement. Due to this cryostat design, the angle of incidence is constrained to a few particular values, the most used being fixed at 70° . When using the cryostat, a calibration procedure is performed against an in-situ silicon wafer reference sample to account for the effects of the entrance and exit windows as well as slight off-angle measurement on the polarization state of the light.

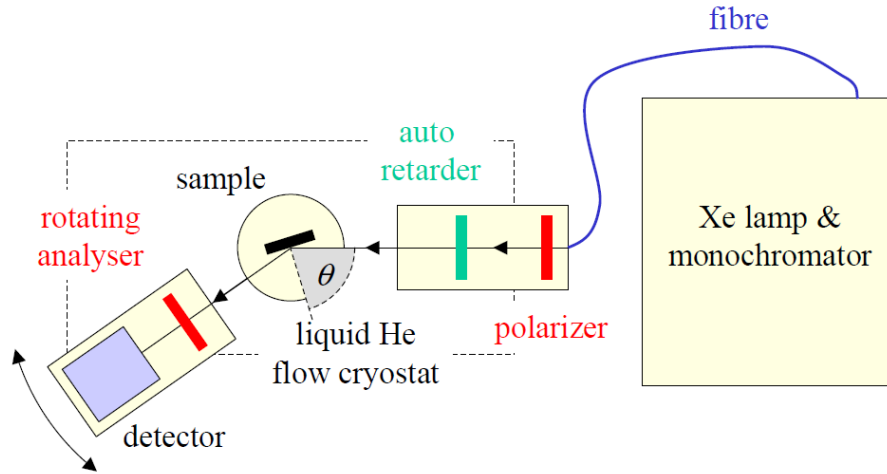


Figure 3.6.: Ellipsometer setup scheme: Light is generated by a Xe lamp, which goes through a monochromating unit (two diffraction gratings) before being sent through an optical fiber to the source arm. There a polarizer and auto-retarder manipulate the polarization state before the light reaches the sample at an angle of θ . On the detector arm, a rotating analyser is placed before the detector stack. The sample can be placed in a liquid-Helium cryostat allowing low-temperature measurements. Reproduced from [51].

3.4.3. Data analysis

The data analysis of the ellipsometric data, namely, the ellipsometric angles, is a critical step. The analysis is performed in the WVASE software provided by J.A. Woollam, which is highly specialized in analyzing ellipsometric data. Still, ellipsometry analysis is somewhat more art than science.

As stated before, once more complex situations than a pure bulk material are considered, an optical model must be built. The workflow of the data analysis can be seen in fig. 3.7 and can be summarized as i) construction of an optical model, ii) selection of dielectric functions, iii) fit model to ellipsometric angles, iv) and evaluate. Effectively, we search for the values of ϵ_1 and ϵ_2 that, given the optical model, reproduce the ellipsometric angles measured.

Since ellipsometry is a very surface-sensitive technique, a more sophisticated analysis is required to obtain the sample's proper bulk dielectric function. To achieve this, a multilayer formalism is used, which is a generalization of the core principle of bulk ellipsometry. Although very elegant, a full account of the multilayer formalism to analyze ellipsometric measurements is beyond the scope of this work. For us, in most cases, the primary source of error in the determination

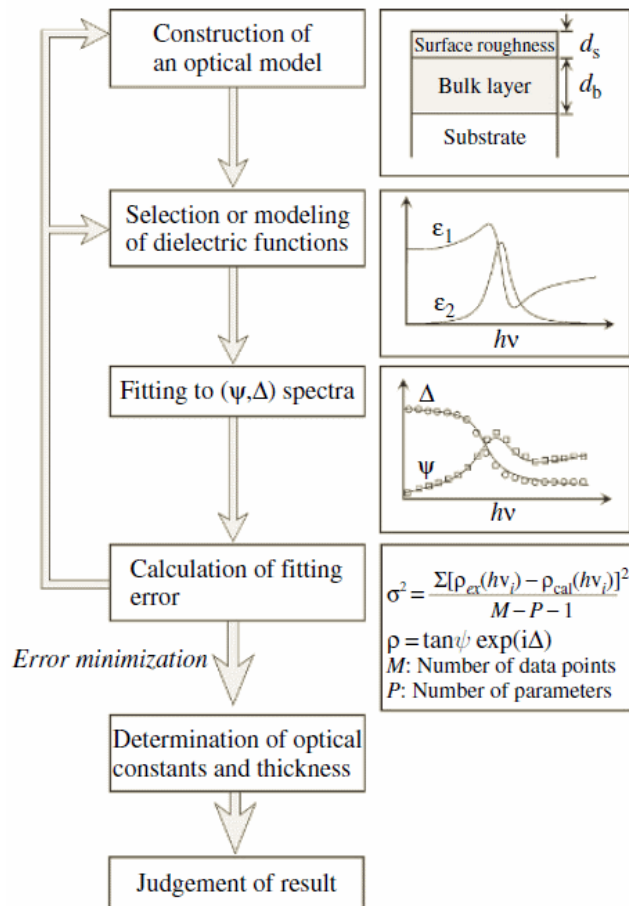


Figure 3.7.: The workflow to analyze the ellipsometric data starts with the construction of an optical model. In our case, the model consists only of a substrate, which is equivalent to our bulk material and a surface roughness layer of a certain thickness. In the second step, we populate the optical model with a set of oscillators. These oscillators are chosen to approximate the measured ellipsometric data. A fit of the optical model's parameters is performed between the Ψ and Δ given by the model and the measured ones. Reproduced from [50].

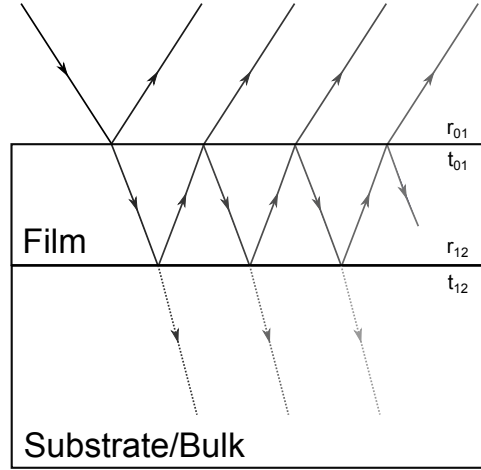


Figure 3.8.: When encountering a system of a bulk sample and a film one has to consider two interfaces and multiple reflections originating from them. Interfaces 01 and 12 are between ambient/film and film/substrate, respectively.

of the dielectric function of bulk materials is the existence of a surface roughness layer.¹⁶

When considering an extra layer on top of the bulk, as shown in fig. 3.8, equation (3.26) is not valid since the relationship is not invertible. Without going into the derivation, when considering two interfaces, the ratio between reflected and incident light is a function of the Fresnel coefficients at both interfaces r_{01} and r_{12} and given by [48]

$$\frac{E^r}{E^i} = \frac{r_{01} + r_{12}e^{-i2\beta}}{1 + r_{01}r_{12}e^{-i2\beta}} \quad (3.27)$$

where β is the optical thickness of the film which depends on the thickness d , wavelength λ , and angle of incidence θ given by

$$\beta = 2\pi \frac{d}{\lambda} \sqrt{n_1^2 - n_2^2 \sin^2 \theta} \quad (3.28)$$

Equation (3.27) holds for both polarizations, parallel and perpendicular. By combining both orientations, the ellipsometric angles are obtained. Here it is very explicit the difficulty of ellipsometry as, in principle, there are five unknown

¹⁶Effectively this also could consider other things like adsorbates, surface reconstruction, or slight surface oxidation.

Chapter 3: Optical Spectroscopy

parameters for a single thin layer on top of the substrate ϵ_{bulk} , ϵ_{film} , and the film thickness but only two measured values. Usually, the film's thickness is an externally known parameter that is independent of the photon energy. Measuring at different angles or with different thicknesses for the thin film can provide the extra information needed.

In the context of investigating bulk materials, we assume that the thin film is, effectively, only a surface roughness of undetermined thickness but with optical properties defined by the bulk material. This thin film is present in our experiments regardless of how well we prepare the surface by careful polishing. Eventually, oxidation or adsorbates (contamination) will always be present since the sample preparation is done *ex-situ*. Previous work in this setting established that the data for single crystals, the measured pseudo-dielectric function $\langle \epsilon \rangle$ is almost independent of the angle of incidence, thus indicating that such cover layer must be thin [31]. Thus, the measured optical properties are primarily determined by the bulk and only marginally impacted by the thin cover layer of adsorbates. This cover layer's primary effect is an energy-dependent vertical shift of the calculated dielectric function of the bulk material that does not change the relative spectral weights of the features as a function of temperature. Regardless, we aim to take this thin cover layer to obtain absolute values of the bulk optical properties. Due to this situation with the cover layer, measurements are performed in one extended session to avoid or minimize issues with an evolving surface layer or other measuring device drifts.

The most straightforward way to account for surface roughness effects is by using an *effective medium approximation* (EMA). In this approximation, an equally weighted average of the dielectric functions at the interface, in this case, the bulk and air/vacuum, are used as the dielectric function of a thin film representing the surface roughness. Using such an approximation reduces the number of parameters to determine by two since the thin layer's dielectric function is given only by the dielectric function of the bulk material.

Now, the problem is how to determine the thickness of such a thin cover layer. A strategy to do so is to look for a non-absorbing region and do a fit of the EMA cover layer thickness using a *Cauchy* model for the bulk in that region. Going into a non-absorbing region implies that the optical parameter k is absent; thus, instead of having three parameters (n , k , d) to determine, we only have two. In the case of materials that show no transparent region in the measured range, then a reasonable thickness is used.

To obtain the optical constants from the ellipsometric angles, there are two main strategies. The first tries to fit the data point-by-point at each measured

wavelength. At each measured wavelength, the best ε_1 and ε_2 are chosen to describe the measured Ψ and Δ given a model. This strategy has the advantage of assuming very little about the sample being investigated and performing quickly. However, it has some problems, like not being necessarily Kramers-Kronig consistent, or in some cases, not converging. The second option is to build an oscillator model, as discussed in section 3.1.3, and fit the parameters to the measured data. This strategy has the potential to describe microscopic features, but it is not guaranteed or necessary that an oscillator used in the modeling has a physical meaning. Compared with the point-by-point strategy, this has the advantage of using a reduced set of parameters to fit and being Kramers-Kronig consistent if the oscillators used are so.

Once a fit is obtained, it is evaluated to see if it is consistent and makes physical sense. At this step, the analysis can be considered done, or if the fit is not good enough, the optical model can be further modified and refined to describe the measured data better.

In the case of anisotropic samples, to fully describe the dielectric function one needs to measure different orientations and then fit them simultaneously with an anisotropic-aware model [49, 50]. Alternatively, one may use eq. (3.26) to obtain the pseudo-dielectric function instead, which often is a good approximation in layered systems.

4. $\text{La}_2\text{Cu}_2\text{O}_5$: a 4-Leg Spin-1/2 Ladder System

THE DISCOVERY OF *unconventional* superconductivity at relatively high temperatures in the two-dimensional doped cuprates [4] gave a substantial research boost to the whole field of low-dimensional quantum spin systems. Two reasons behind this are the suggestion of a close relationship between magnetism and high-temperature superconductivity [53], and the belief that the relevant physics emerges from the degrees of freedom on the planes. The parent compounds of the high-temperature superconductors consist of stacked CuO_2 layers, which are considered to be the best experimental realization of 2D square-lattice Heisenberg antiferromagnets. This has led to the exploration of alternative low-dimensional magnetic systems in transition-metal oxides like vanadates, manganites, nickelates, and of course, cuprates, looking for clues and hints to understand the microscopic mechanisms of superconductivity at high temperature. For example, quite recently, Li et al. [54] reports superconductivity in a nickelate layered system which is isostructural to copper oxides layered systems.

Although a lot is known, the understanding of low-dimensional quantum spin systems is still far from complete. Here, we are interested in how the properties of spin ladders evolve with an increasing number of legs. It is expected that a crossover to the 2D square lattice can be approached by adding more and more legs. Thus, the aim is that through the study of the ground state and elementary excitations of $S = 1/2$ n -leg ladders, new insights can be gained towards understanding the parent compounds of high-temperature superconductivity [55].

4.1. Low-dimensional quantum spin systems

Dimensionality plays a significant role in the behavior of materials, *e.g.*, the shape of the density of states is strongly influenced by it. In magnetic systems, as the dimension and spin are reduced, quantum fluctuations become increasingly more

relevant. For example, in the 2D $S = 1/2$ square lattice, long-range order is achieved only at $T = 0$. The appearance of long-range order in actual materials at $T \neq 0$ is due to finite 3D coupling [56]. Also, in the 1D $S = 1/2$ chain, not even at $T = 0$ long-range magnetic order is achieved [57]. This means that fundamental to low-dimensional quantum spin systems is the concept of *spin liquids*¹ where the ground state is dominated by these strong quantum fluctuations that suppress long-range magnetic order.

A way to describe spin liquids, pioneered by Anderson [53], is called resonating valence bond (RVB). This model considers a ground state of nearest-neighbor singlet ($\frac{1}{\sqrt{2}}[|\uparrow\downarrow\rangle - |\downarrow\uparrow\rangle]$) pairs. This resonating valence bond picture is supported in the 2- and 4- leg ladders by mean field [58], density matrix renormalization group (DMRG) [59, 60], Quantum Monte Carlo (QMC) [61], Lanczos [55], and variational *ansatz* [62, 63]. Analogous to the carbon single and double bonding in aromatic rings found in organic chemistry, where the double bond alternates position, in an antiferromagnetically ordered spin system, the singlets alternate pairing partners.

The lack of long-range magnetic order in spin liquids leads to new magnetic excitations different from magnons found in long-range ordered systems. For example, optical spectroscopy studies and inelastic neutron scattering have shown the existence of triplet bound states in $S = 1/2$ two-leg ladders. These bound states stem from strong triplet-triplet interactions. The way spins pair is essential as it provides a way to form charged hole pairs when doped, possibly giving rise to charge density wave or superconducting states in these materials [55]. These magnetic excitations will be explored in more detail in sections 4.1.1 and 4.1.2, for chains and 2-leg ladders, respectively.

It is worthy of mentioning that nowadays, in theoretical circles, the emphasis has moved towards topological aspects [64].

4.1.1. Spin chain

The lowest-dimensional extended spin structure is the 1D spin chain. It is also a relevant system because it provides a way to test exactly solvable theoretical models or to test and benchmark numerical calculations against experimental realizations like the spin-1/2 chain Sr_2CuO_3 or the spin-Peierls system ² CuGeO_3 .

¹Analogous to real liquids, the correlations, magnetic in this case, are very short-ranged leading to short-range order.

²A spin-Peierls system consists of a dimerized spin chain.

4.1 Low-dimensional quantum spin systems

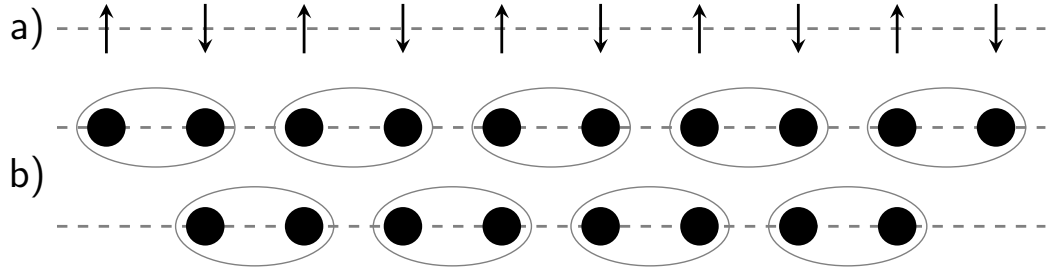


Figure 4.1.: Two sketches of the ground state of a spin-1/2 chain. a) Classical Néel ground state. b) Resonating valence bond picture of the ground state showing two resonating configurations of singlets.

Chains also provide an excellent playground where to understand and visualize some of the physics of low-dimensional systems.

The spin-1/2 Heisenberg antiferromagnetic chain is one of the simplest quantum many-body systems. Thus it has attracted much interest since the early days of quantum physics. It is simple enough to have an exact analytic solution through the Bethe *ansatz* [15]. Regardless of this apparent simplicity, it shows a lot of exciting physics. Some of this wealth of physics will be exposed in the following.

In its most simple scenario, an array of spins can be considered to have only nearest-neighbor interactions³. The Hamiltonian of such a Heisenberg spin chain can be written as

$$H = J \sum_i \mathbf{S}_i \mathbf{S}_{i+1}, \quad (4.1)$$

where \mathbf{S}_i are the spins of the chain, and J their coupling strength. The interesting case is when the coupling is positive, $J > 0$, where the interaction is antiferromagnetic. In contrast to the ferromagnetic case, where the ground state shows a parallel alignment of the spins, in antiferromagnetic chains, the classical Néel configuration as shown in fig. 4.1a) is not the ground state. Instead, the ground state is better represented by a collection of singlets in the resonating valence bond model, which schematically is shown in fig. 4.1b). Regardless of this, the Néel picture can be used to draw some quick understanding of the systems.

The elementary excitations of a Heisenberg antiferromagnetic spin-1/2 chain are described by spinons with spin 1/2. Since a spin flip changes S_z by ± 1 , spinons are excited in pairs [45, 65]. A spinon can be visualized, semiclassically, as a

³When considering further interactions, frustration effects set in enhancing the quantum fluctuations.

Chapter 4: $\text{La}_2\text{Cu}_2\text{O}_5$: a 4-Leg Spin-1/2 Ladder System

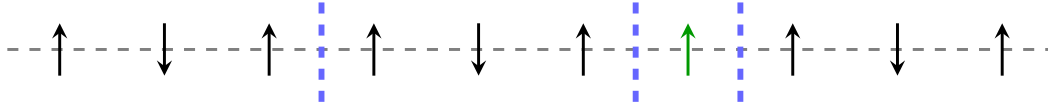


Figure 4.2.: Semiclassical picture of a spinon as a domain wall is indicated as the blue dashed bar between two magnetic domains. When creating an excitation via a spin-flip, two spinons (domain walls) are created as indicated by the green spin. Adapted from [34].

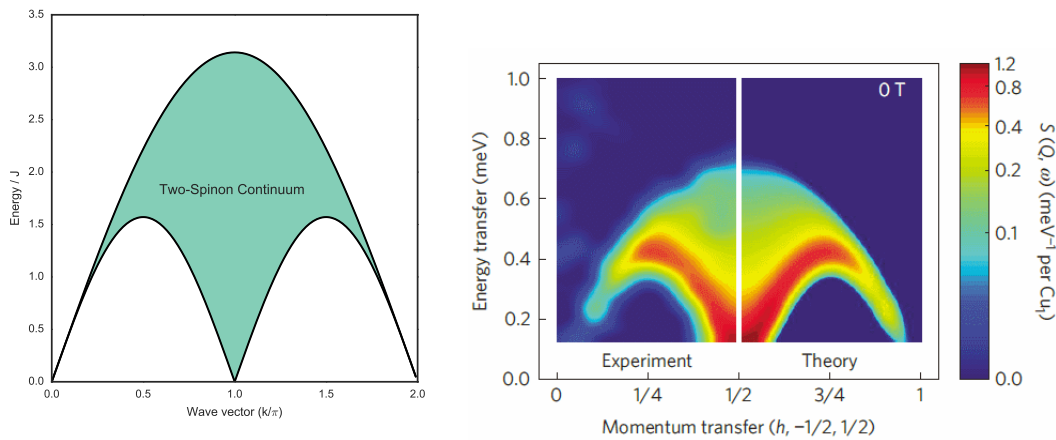


Figure 4.3.: Left: Schematic of the two-spinon continuum [66]. Right: Inelastic neutron scattering (INS) and theory excitation spectra of the magnetic excitations of CuSO_4 . Most of the weight is located close to the lower boundary of the two-spinon continuum. Reproduce from [67].

domain wall between two magnetic domains, as shown with blue dashed bars in fig. 4.2. When creating an excitation, meaning performing a spin-flip shown in green in fig. 4.2, two domain walls are formed. Since two spinons are created, the total momentum k is given by the sum of two contributions as $k = k_1 + k_2$. This leads to the two-spinon continuum in the excitation spectrum because there is effectively one free parameter. Figure 4.3, on the left, shows the theoretical two-spinon continuum for the antiferromagnetic spin-1/2 chain with its lower and upper boundaries. Experimental evidence of this excitation spectrum can be seen in fig. 4.3 on the right part as obtained by inelastic neutron scattering, and most of the intensity is located close to the lower boundary of the continuum. Note that this excitation is gapless at $k = 0$ and $k = \pi$.

The absorption of infrared light of the Sr_2CuO_3 $S = 1/2$ chain is shown in fig. 4.4 as measured by Suzuura et al. [45] and used by Lorenzana and Eder [46]

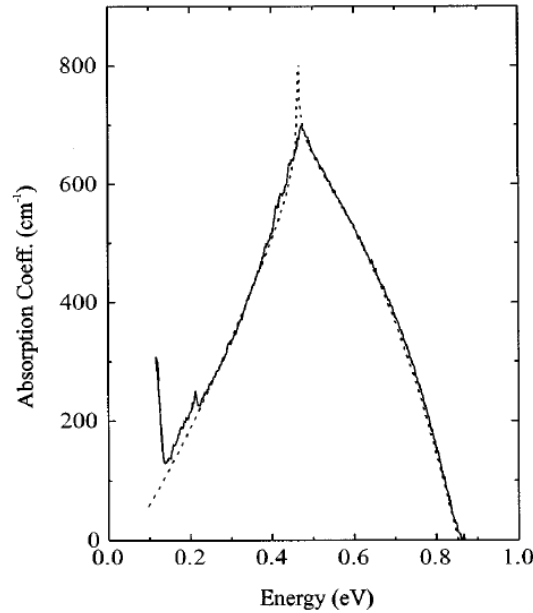


Figure 4.4.: Optical absorption in the mid-infrared range of Sr_2CuO_3 showing a good fit between experiment and bi-magnon-plus-phonon theory. Reproduced from [46].

to test the bi-magnon-plus-phonon theory as described in section 3.3.2 on page 32. The elementary magnetic excitation used here was spinons instead of a classical magnon. After the subtraction of a linear term, a very good fit between theory and experiment is obtained. Particularly notable is the reproduction of a sharp cusp located close to 0.5 eV.

4.1.2. n -leg spin ladders

A crossover from 1D to 2D is offered by n -leg spin ladders [5]. By coupling a number n of chains, one obtains an n -leg ladder. A physical realization of ladders can be found in the family of compounds of the type $\text{Sr}_{n-1}\text{Cu}_{n+1}\text{O}_{2n}$ [68, 69] which give rise to ladder structures with n legs. Figure 4.5 shows the cases for $n = 3, 5$, which give rise to a two and a three-leg ladder, respectively. The ladders are composed of CuO_2 planar structures, which are highlighted in blue. In this series, $\text{Cu}_{n+1}\text{O}_{2n}$ sheets alternate with Sr_{n-1} ones along the c axis, decoupling ladders in the perpendicular direction.

Two in-plane ladders are decoupled through the combined effects of two effects.

Chapter 4: $\text{La}_2\text{Cu}_2\text{O}_5$: a 4-Leg Spin-1/2 Ladder System

The first is that the spins in the trellis structure shown in the rightmost highlight (light red) of fig. 4.5 have a weak ferromagnetic exchange interaction given by

$$|J'| = \frac{8t_{pd}^4}{\Delta^2} \left[\frac{1}{E_T + 2\Delta} - \frac{1}{E_S + 2\Delta} \right] \quad (4.2)$$

where t_{pd} is the nearest neighbor hopping between Cu $3d_{x^2-y^2}$ and O $2p_{x,y}$, Δ is the difference between on site energies between Cu $3d_{x^2-y^2}$ and O $2p_{x,y}$, and $E_{T,S}$ is the triplet (singlet) energy level [58]. Using the estimated parameters, one can estimate $|J'|/J \sim 0.1-0.2$, showing that it is a weak ferromagnetic exchange interaction. This is a more elaborate way to say that the exchange between spins in two ladders is ferromagnetic and weak due to the 90° Cu-O-Cu bonds. This leads to frustration and, thus, to a negligible coupling between ladders.

Spin ladders show many exciting properties arising from their low dimensionality, and their study is crucial due to their possible relevance in connection to the high-temperature superconductivity phenomena. Remarkably, Dagotto and Rice [70] predicted that even-leg ladders could show superconductivity under slight hole doping. This has been found in the 2-leg ladder $\text{Sr}_{14-x}\text{Ca}_x\text{Cu}_{24}\text{O}_{41}$ with $x = 13.6$ at $T = 13\text{K}$ under high pressure of 3 GPa [71]. Moreover, Dagotto and Rice [70] predicted that whether n is even or odd produces striking differences in the properties of each system. Ladders with even n show a spin-liquid ground state with a gapped (spin) excitation spectrum and short-range (spin) correlations. In contrast, odd n ladders show a ground state which is isomorphous to the 1D chain and power-law (spin) correlations. This predicted behavior, has been confirmed experimentally through the physical realizations of the 2-leg SrCu_2O_3 and 3-leg $\text{Sr}_3\text{Cu}_2\text{O}_5$ [69] ladders. Observations for higher n are scarce.

As the number of legs is increased, the physical properties should converge to the 2D square layer. This convergence is not necessarily smooth; for example, odd ladders show no spin gap like the chain and 2D square layer. This dimensional crossover is one of the driving forces in the research of this class of materials. We will keep the discussion focused mainly on 2-leg ladders, with some odd-leg ladders' observations when needed. It also serves as an excellent introduction to the similar physics in the compound of interest, the 4-leg ladder.

The most straightforward ladder corresponds to a 2-leg spin ladder, consisting of two spin chains coupled through an inter-chain exchange J^\perp . It is schematically

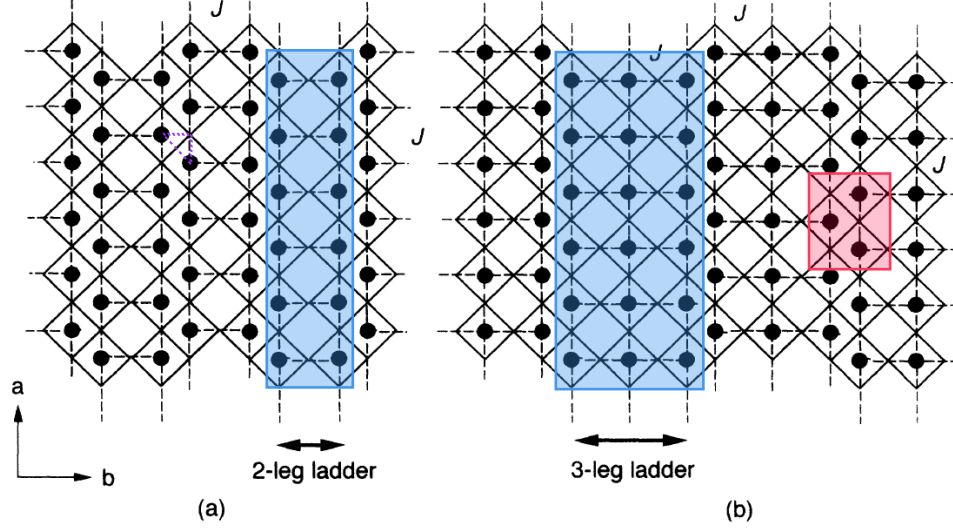


Figure 4.5.: The ladders are highlighted in blue. The legs of the ladders run along the a direction and the rungs along the b direction. The 90° degree Cu-O-Cu bond between neighboring ladders is shown in purple, while the frustration situation is highlighted in red. a) 2-leg ladder SrCu_2O_3 b) 3-leg ladder $\text{Sr}_2\text{Cu}_3\text{O}_5$. Reproduced from [69].

shown in fig. 4.6. The simplest Hamiltonian for the 2-leg ladder is given as

$$H = \sum_i J_{\parallel} (\mathbf{S}_{1,i} \mathbf{S}_{1,i+1} + \mathbf{S}_{2,i} \mathbf{S}_{2,i+1}) + J_{\perp} \mathbf{S}_{1,i} \mathbf{S}_{2,i}, \quad (4.3)$$

where the first term represents two Heisenberg chains as in equation (4.1) with coupling constant J_{\parallel} and the second term describes the interaction between chains with coupling constant J_{\perp} . The first subscript of the spin $1/2$ operator denotes the legs, while the second one (i) denotes the rung index.

The most straightforward way to understand the physics of the 2-leg ladder is by considering the strong-coupling⁴ limit where $J_{\perp} \gg J_{\parallel}$. In this case, the ground state can be described by a product of independent rung singlets sitting on each rung shown as blue bars in fig. 4.6. This means that the elementary spin excitation is the creation of a triplet state $|\phi_T\rangle = \{|\uparrow\uparrow\rangle, |\downarrow\downarrow\rangle, (|\uparrow\downarrow\rangle + |\downarrow\uparrow\rangle)/\sqrt{2}\}$ ($S = 1$) from a singlet, shown as red bars in fig. 4.6. This well-defined spin excitation, also

⁴Another possibility is to start from the weak-coupling limit $J_{\parallel} \gg J_{\perp}$. However, the strong-coupling limit has proven to be an excellent starting point to describe the physics in ladders [72].

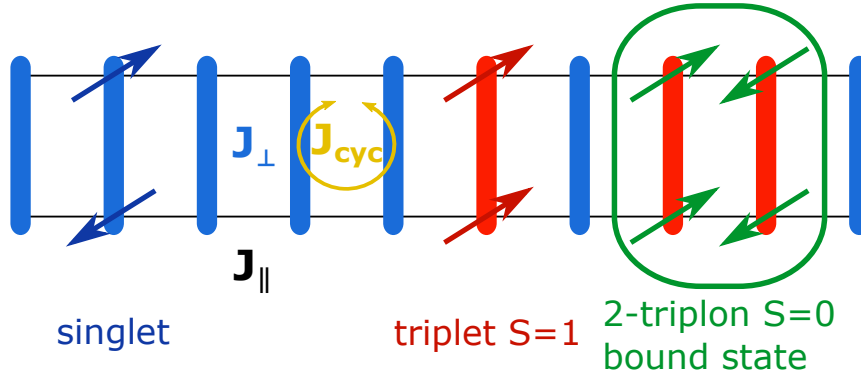


Figure 4.6.: Sketch of a 2-leg ladder in the strong coupling limit ($J_{\perp} \gg J_{\parallel}$) indicating the rung J_{\perp} , leg J_{\parallel} , and cyclic J_{cyc} exchange interactions. Blue (red) thick bars are the singlet $S = 0$ (triplet $S = 1$) states on the rungs. Due to the antiferromagnetic interaction two triplets/triplons can bind together. One such scenario is depicted in green, where the 2-triplon bound state with $S = 0$ is shown. Reproduced from [34].

called triplon, has due to a finite⁵ J_{\parallel} exchange interaction a dispersion as shown in fig. 4.7 with closed symbols for different coupling ratios. Figure 4.7 also shows the lower boundary of the 2-triplon continuum with open symbols, showing that the triplet dispersion merges into the continuum for small wave vectors.

Evidence of the elementary triplon dispersion of a 2-leg ladder can be observed in fig. 4.8 for the nearly ideal system $\text{La}_4\text{Sr}_{10}\text{Cu}_{24}\text{O}_{41}$ as obtained by inelastic neutron scattering [74]. The figure shows that most of the weight is located at $k = 0.52\pi/c$. The white line shows the calculated⁶ 1-triplon excitation.

Due to the antiferromagnetic interaction, 2-triplon bound states in the 2-leg ladder were expected [76–78]. Two triplons can interact and form a bound state with $S = 0, 1, 2$. The $S = 0$ bound state is naively depicted inside the green blob in fig. 4.6. Figure 4.9 shows, for the isotropic 2-leg ladder ($J_{\perp}/J_{\parallel} = 1$), the elementary triplon excitation, the $S = 0$ and $S = 1$ bound states, and the 2-triplon continuum [72]. For the isotropic case, the binding energy of the bound state vanishes below $k \sim 0.3\pi$ as it merges into the continuum. Still, inside the continuum, a resonance may appear due to the attractive interaction. The $S = 1$

⁵If J_{\parallel} would be zero, then the system consists of a collection of "diatomic molecules" showing no dispersion. An isolated singlet's energy is $-3/4J_{\perp}$, whereas the one for a triplet is $J_{\perp}/4$. The difference yields J_{\perp} as the excitation gap.

⁶The model used is slightly more complex than the one described in equation (4.3) by including a cyclic four-spin interaction. The introduction of this cyclic interaction is essential to describe the 2-leg ladders accurately [75].

4.1 Low-dimensional quantum spin systems

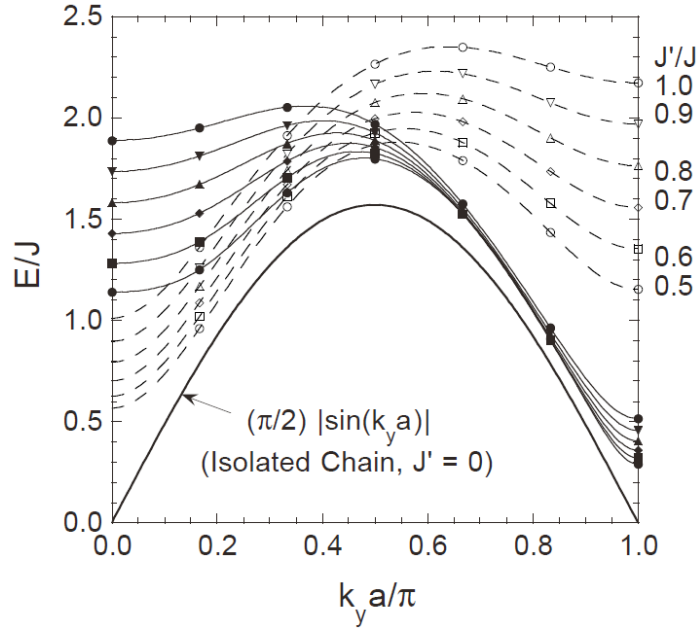


Figure 4.7.: Calculated one-triplon dispersions (closed symbols) and lower boundary (open symbols) of the 2-triplon continuum for different J_{\perp}/J_{\parallel} ratios (J'/J in the figure) for an isolated 2-leg (2×12) ladder. Reproduced from [73].

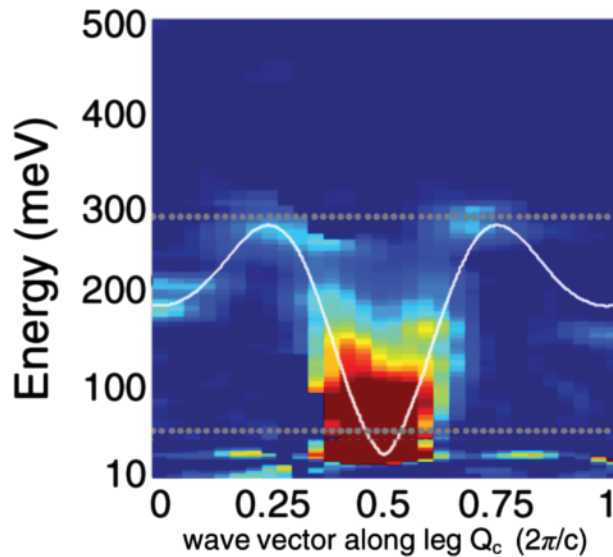


Figure 4.8.: The 1-triplon dispersion of the 2-leg ladder $\text{La}_4\text{Sr}_{10}\text{Cu}_{24}\text{O}_{41}$ obtained by inelastic neutron scattering. It shows a spin gap of 26.4 ± 0.3 meV. The white curve shows the calculated 1-triplon dispersion. Most of the scattered intensity lays around $0.52\pi/c$. Reproduced from [74].

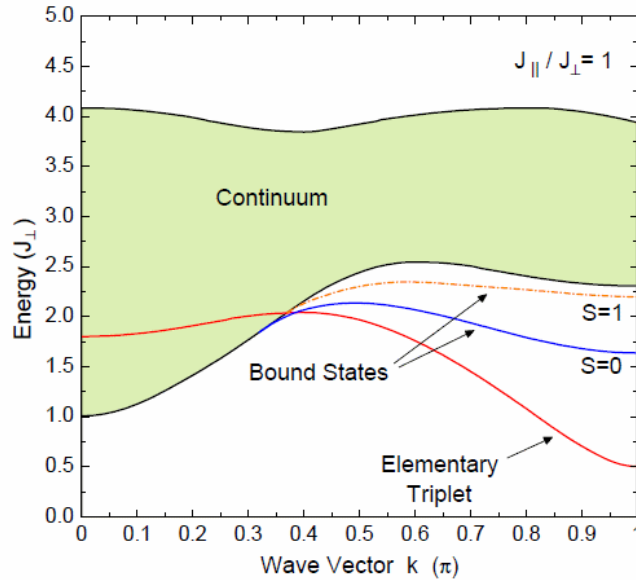


Figure 4.9.: The calculated excitations for the isotropic 2-leg ladder ($J_{\perp}/J_{\parallel} = 1$). It shows the triplon dispersion in red, and the 2-triplon continuum in green area. Furthermore, it shows the $S = 0$ and $S = 1$ bound states in blue and dashed red, respectively. Reproduced from [72].

bound state has lower binding energy than the $S = 0$ one; thus, it is shown closer to the continuum and enters earlier into it. For $S = 2$, one finds an anti-bound state, for which we will not go into detail.

Inelastic neutron scattering (INS) is the *de facto* tool to investigate magnetic excitations. However, the dynamical structure factor of the $S = 1$ bound state is 20 times smaller than the one for the triplet excitation [76]. Moreover, the high energy of these bound states in the cuprates makes inelastic neutron scattering experiments challenging. Besides, the $S = 0$ bound state is invisible to INS since its structure factor is zero. These three facts open the door to optical methods like infrared absorption, as described in section 3.3.2 to probe these bound states.

As mentioned in section 3.3.2, infrared absorption of the bi-magnon-plus phonon process measures the whole magnetic Brillouin zone. Thus it is equivalent to making a horizontal cut in fig. 4.9 (or vertical one in fig. 4.10) and adding the contribution to the absorption in a weighted fashion. This means that the optical absorption calculations require the momentum-resolved spectral densities of the $S = 0$ channel, *i.e.*, bound state and continuum. The momentum-resolved spectral densities are shown in fig. 4.10 for leg (top) and rung (bottom) polarization for the isotropic 2-leg ladder ($J_{\perp}/J_{\parallel} = 1$). Thus, the optical conductivity

4.1 Low-dimensional quantum spin systems

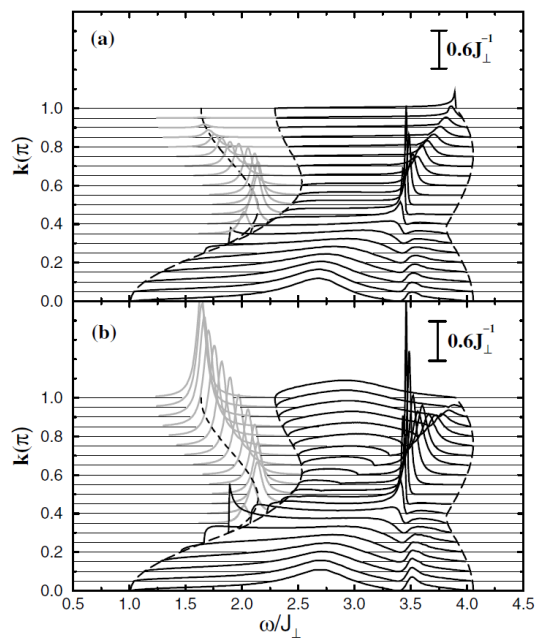


Figure 4.10.: The k -resolved spectra for a 2-leg ladder for the $S = 0$ channel showing the bound state (dashed) and the 2-triplon continuum (bold area) as obtained by continuous unitary transformation technique for $J_{\perp}/J_{\parallel} = 1$. Top: Rung polarization shows a strong reduction of the bound state weight approaching $k = \pi$. Bottom: Leg direction shows a steadily strong weight over the whole bound state. Here the continuum contribution is multiplied by 4 to make the features more visible. Adapted from [72].

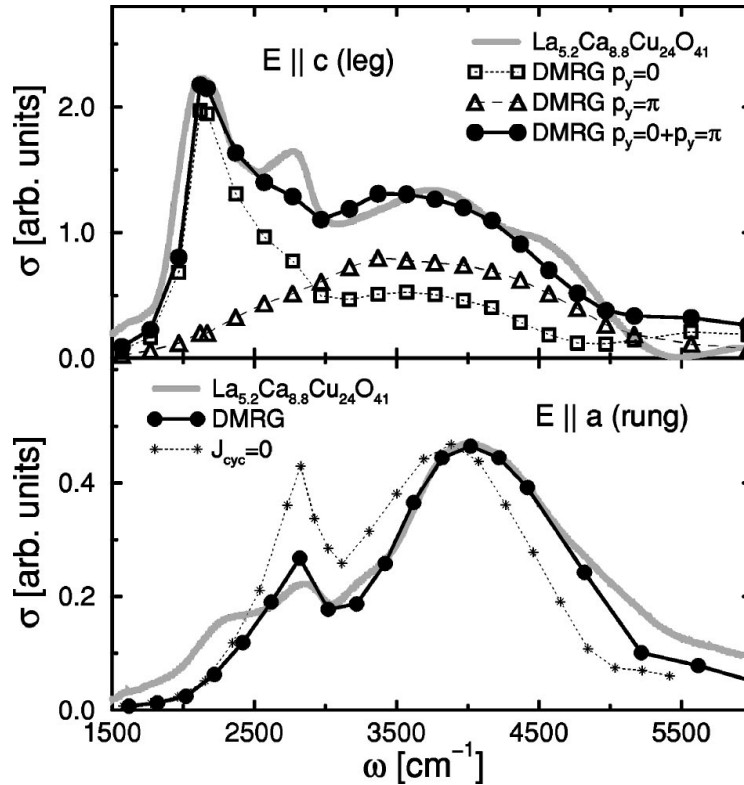


Figure 4.11.: Optical conductivity of the 2-leg ladder $\text{La}_{5.2}\text{Ca}_{8.8}\text{Cu}_{24}\text{O}_{41}$ for polarization along the ladder and rung directions. Density-matrix renormalization group (DMRG) calculations [75] show a good fit between theory and experiment. Through the theoretical models, the broad feature at high energies is interpreted as the contribution of the continuum to the spectra, while the peaks correspond to contributions stemming primarily from the $S = 0$ bound state [47]. Top: Leg direction. Bottom: Rung direction. Reproduced from [75].

is obtained by integrating the k -resolved spectra with a suitable weighting factor, which accounts for the phonon involved in the process.

The 2-triplon bound state was first observed in $\text{La}_{5.2}\text{Ca}_{8.8}\text{Cu}_{24}\text{O}_{41}$ employing infrared spectroscopy [47]. In fig. 4.11, the optical conductivity (light gray) for light polarized in leg (top) and rung (bottom) polarization is shown. Interestingly, in contrast to the single peak in 2D square layers, the infrared absorption of 2-leg ladders shows two peaks. Moreover, similar to the 2D square layer in $\text{YBa}_2\text{Cu}_3\text{O}_6$ (YBCO) as described in 4.1.3, the 2-leg ladder shows a high-energy contribution to the optical conductivity.

The first feature is easily explained. The spectral intensity is proportional to

the integrated density of states. This means that singularities in the density of states, also known as van Hove singularities, which are located at the maxima or minima of a dispersion curve, produce peaks in the optical absorption. Since the $S = 0$ bound state has a maximum and a minimum at $k \sim \pi/2$ and $k = \pi$ as shown in figs. 4.9 and 4.10, two peaks can be expected in optical absorption. Contributions to the optical absorption at higher energies come mainly from the 2-triplon continuum⁷ [47].

From the position of the peaks in the optical conductivity and the value of the spin gap from neutron scattering, a set of exchange constants can be extracted [74]. Besides the experimental data, density-matrix renormalization group (DMRG) calculations based on the extracted parameters are displayed in fig. 4.11, showing a good fit of the features [75]. The DMRG calculation shows that the optical conductivity has two contributions to the leg polarization (p_y). One in-phase ($p_y = 0$) excitation mode that contains the $S = 0$ two-triplon bound state with some contribution to the continuum stemming from 2- and 4-triplon excitations. And one out-of-phase ($p_y = \pi$) mode contains contributions from 3-triplon continuum excitations [75]. The source of the differences between the DMRG calculated and experimental data are related to effects stemming from the choice of the weighting function.

In this section, we have seen how the 2-leg ladder is well described and understood, with a particular focus on the optical spectra of a specific 2-leg ladder realization. This knowledge and experience will allow the possibility of exploring the 4-leg ladder in section 4.2.

4.1.3. 2D $S = 1/2$ square lattice

In 2D, instead of trying to do a full review of its properties, we will focus on the optical spectra of spin-1/2 antiferromagnetic square lattices. These systems also show interesting features in their infrared data, but they are still not completely understood. As shown in fig. 4.12, different 2D cuprates feature an absorption lineshape, which is independent of the chemical composition of the material⁸ [79]. Every compound shows a sharp peak close to $3J$, which for the compound La_2CuO_4 means about 0.4 eV (see left panel of fig. 4.13), and sidebands at higher energies. The strong features present below 0.1 eV are the fingerprints of the phonons, whereas at high energy (above ~ 1 eV), the feature originates from the

⁷Contributions of 4-triplon and higher-order excitations can also be present.

⁸Note that the authors of reference [79] subtracted different backgrounds from the data.

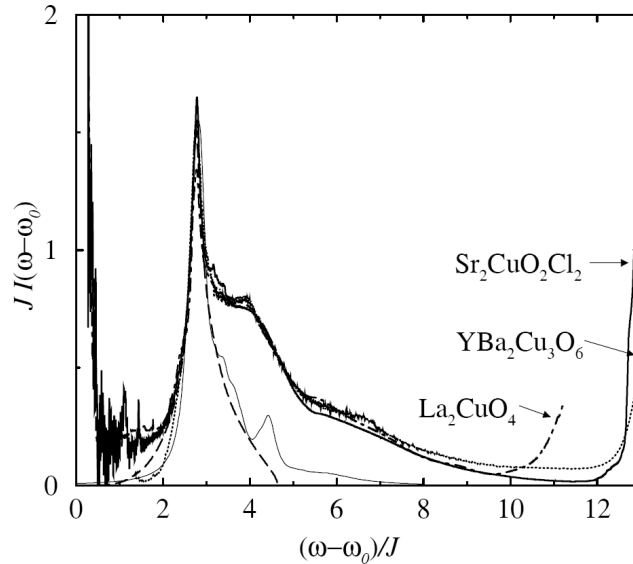


Figure 4.12.: Comparison of absorption measurements of several 2D cuprates (dot-dashed: La_2CuO_4 , solid: $\text{Sr}_2\text{CuO}_2\text{Cl}_2$, and dotted: $\text{YBa}_2\text{Cu}_3\text{O}_6$) showing a similar behavior. All compounds show a peak close to $3J$ plus higher-energy sidebands. The dashed line shows the theoretical expectation in spin-wave theory, and the thin line for a cluster calculation. Reproduced from [79].

charge transfer (electronic gap) excitation. The dashed line in fig. 4.12 shows the theoretical description based on a bimagnon-plus-phonon absorption process within the spin-wave theory, as described in section 3.3.2, while the thin gray line depicts the result of a cluster calculation.

The bimagnon-plus-phonon absorption theory manages to fit very well to the sharp peak at about $3J$ but does not describe the high-energy spectral weight at about $4J$ and above [80]. One alternative is that multi-magnon contributions carry the missing spectral weight. However, this weight is also missing when doing exact diagonalization of the square-lattice Heisenberg model [79]. Including a cyclic exchange has been suggested as a possible solution [79]. The cyclic exchange is ruled out since J_{cyc}/J is comparable between the 2-leg ladder and the 2D square lattice, and in the 2-leg ladders, it only enhances the spectral weight by about 20% [81].

When an isostructural compound to La_2CuO_4 is considered, namely La_2NiO_4 with $S = 1$, the complete magnetic absorption spectrum is well reproduced as it can be seen in fig. 4.13. In this case, the higher value for the spin ($S = 1$) drastically reduces the effects of quantum fluctuations, and the spin-wave description of

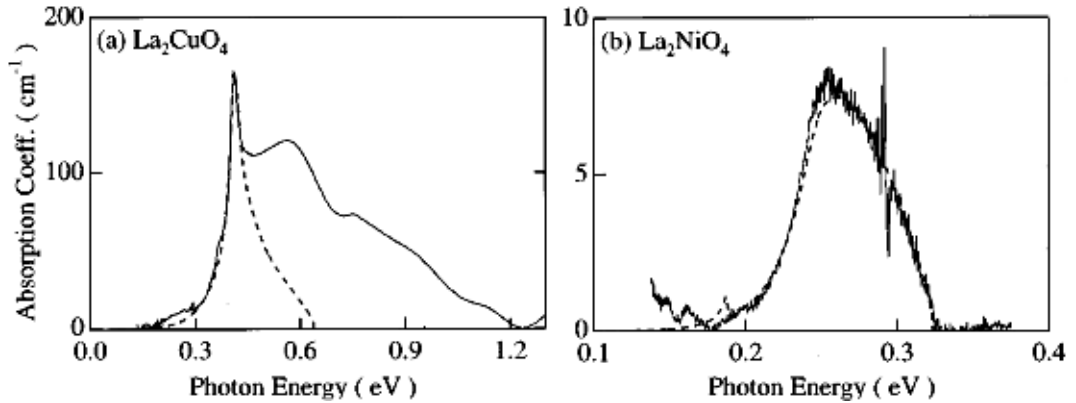


Figure 4.13.: Comparison of $S = 1/2$ and $S = 1$ square-lattice compounds La_2CuO_4 (left) [82] and La_2NiO_4 (right) [83]. The dashed lines are the bi-magnon-plus-phonon predicted outcome. Clearly, the case for $S = 1$ shows a very good agreement between experiment and theory, giving a strong hint towards the role of quantum fluctuations in the nature of the sidebands.

magnetic excitations is enough to describe the optical absorption.

The role of quantum fluctuations is further confirmed by the optical absorption results in spin chains, as shown in section 4.1.1. The starting point to describe the magnetic absorption feature is not a conventional spin-wave but a two-spinon structure that encodes the quantum fluctuations directly, where the high-energy spectral weight arises from the continuum of excitations of the spinons involved in the process. This leads to the hypothesis that quantum fluctuations beyond spin-wave theory should be considered to describe the infrared absorption in 2D cuprates [84] fully.

4.2. 4-leg ladder $\text{La}_2\text{Cu}_2\text{O}_5$

A physical realization of a 4-leg ladder can be found in the $\text{La}_2\text{Cu}_2\text{O}_5$ compound⁹. This compound's growth is complicated [86], due to a very narrow temperature tolerance in its growth process, leading to a scarcity of experimental data on it.

The crystal structure of $\text{La}_2\text{Cu}_2\text{O}_5$ is monoclinic (space group $C 2/c$) with lattice parameters $a = 13.869(3)\text{\AA}$, $b = 3.7487(5)\text{\AA}$, and $c = 27.967(5)\text{\AA}$, with an angle

⁹This material is a member of the homologous series of lanthanum cuprate $\text{La}_{4+4n}\text{Cu}_{8+2n}\text{O}_{14+8n}$ [85, 86] with $n = 2$. This series with $n = 3$ gives rise to a 5-leg ladder.

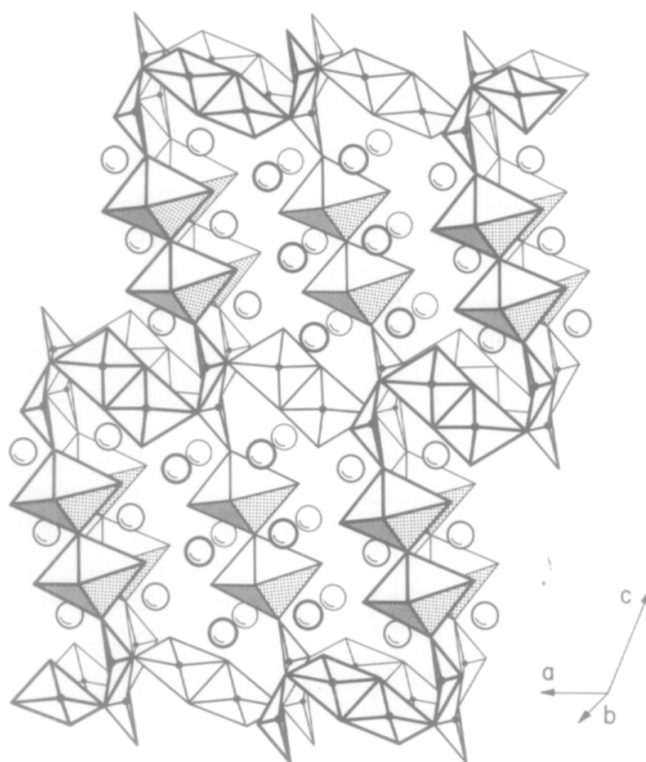


Figure 4.14.: Simplified view of the crystal structure of $\text{La}_2\text{Cu}_2\text{O}_5$. The big open circles correspond to La. The ladder structures are made of two different environments, tetrahedral and octahedral ones. The Cu(1) is inside the solid octahedra which is slightly distorted by a Jahn-Teller effect, while the small solid circles are the Cu(2) inside a highly flattened tetrahedron. Reproduced from [87].

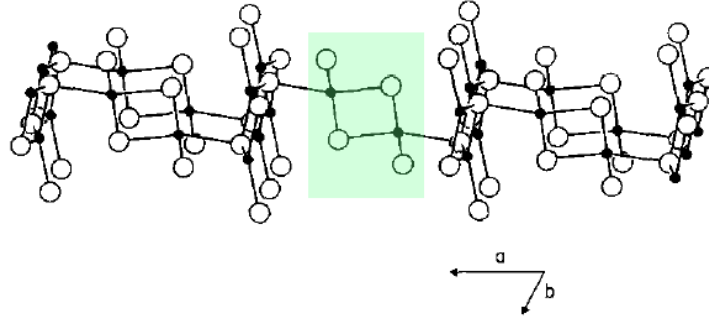


Figure 4.15.: Alternative view of the crystal structure of $\text{La}_2\text{Cu}_2\text{O}_5$ showing more details of the bonding scheme of the Cu–O planes. The big open circles correspond to O while the small ones to Cu. Highlighted in the center, are the Cu(3) ions forming a double chain along the b direction. Adapted from [87].

		α ($^\circ$)	d (\AA)	bond
Rung	$J_{\perp 1}$	179.87	3.87	Cu(1)-Cu(1)
	$J_{\perp 2}$	178.65	3.93	Cu(1)-Cu(2)
Leg	$J_{\parallel 1}$	179.11	3.75	Cu(1)-Cu(1)
	$J_{\parallel 2}$	154.73	3.85	Cu(2)-Cu(2)

Table 4.1.: Angle (α) and distance (d) between the different Cu ions involved in the formation of the 4-leg ladder.

$\beta = 106.06(1)^\circ$ and is depicted in 4.14 [85] showing the two Cu environments present. Within the unit cell, three different crystallographic Cu^{2+} sites are found, but only two of the three different Cu ions participate in the ladder structure, the other (Cu(3)) forms a Cu–O chain along the b axis shown in fig. 4.15.

$\text{La}_2\text{Cu}_2\text{O}_5$ contains Cu^{2+} ions that are coupled by almost 180° Cu–O–Cu bonds along leg and rung directions shown in a top view of the structure in fig. 4.16. The figure shows the two Cu environments involved in the ladder structure in green the Cu(2) ions and in blue the Cu(1) ones. The ladders are composed by Jahn-Teller-elongated CuO_6 octahedra (Cu(1)) at the center of the ladder forming CuO_2 -layer-like pieces composed of 2 Cu(1) units, and a complex copper-oxygen structure of CuO_4 tetrahedra at the borders of the ladder (Cu(2)). When considering nearest-neighbor interactions only, four different possible exchange couplings are expected due to the bond angles and lengths (cf. fig. 4.16 and table 4.1).

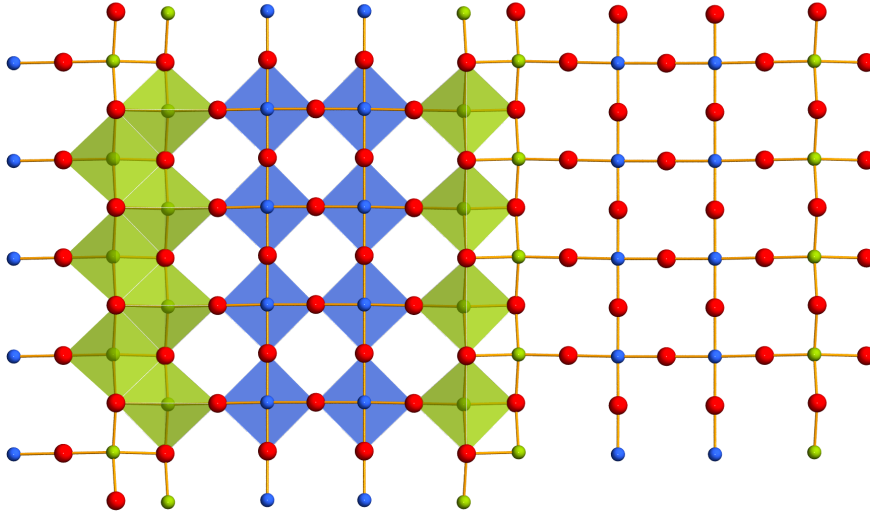


Figure 4.16.: A simplified top view of a layer of $\text{La}_2\text{Cu}_2\text{O}_5$. Cu(1) in blue and Cu(2) in light green. The legs of the ladder are along the b direction.

Since copper's valence state is $2+$, it is expected to be a bad electrical conductor. The electrical resistivity of an as-grown $\text{La}_2\text{Cu}_2\text{O}_5$ crystal measured along the leg direction at room temperature gives a value of $1.7 \times 10^3 \Omega \text{cm}$ [85]. It has been found that $\text{La}_2\text{Cu}_2\text{O}_5$ has an antiferromagnetic ordering temperature of $T_N = 130 \text{ K}$ [86, 88]. The magnetic susceptibility shows a broad peak near 190 K with a FWHM of about 200 K [87, 88].

4.3. Results

The sample used in this work was grown and structurally characterized in-house by Martin Valldor. Then it was prepared for transmission measurements by Luis Fels, with a thickness of $200 \mu\text{m}$.

The transmission was obtained from 0.1 to 1.2 eV and is shown in fig. 4.17 for leg (upper) and rung (bottom) polarizations exhibiting a strong polarization dependence. We can observe a steep suppression of the transmission for leg polarization in the range 0.25 eV – 0.6 eV for the 15 K measurement, where it does not surpass the 1% transmittance. For rung polarization, the suppression is more gradual, showing a minimum at about 0.53 eV . The most notable feature in the transmission is in the leg polarization, where a double bump is seen at 15 K . A hint of a similar but much weaker absorption is also seen for the transmittance in

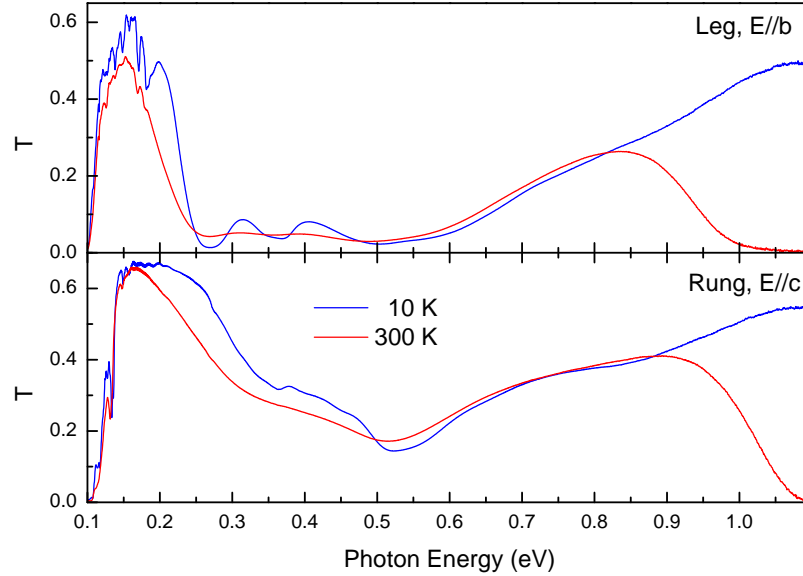


Figure 4.17.: The transmission spectra for $\text{La}_2\text{Cu}_2\text{O}_5$ at 10 K and 300 K for leg (top) and rung (bottom) polarizations.

the rung polarization. At 300 K, the features broaden considerably. These dips in the transmission are the interesting features as they directly relate to absorption.

Since only the transmission was measured, a constant reflectivity value was assumed to obtain the optical conductivity. This is justified since, by experience, the reflectivity for insulating cuprates in the measured region is relatively flat [89] which stems from a small value of k which further implies a relatively constant value for n . Thus, the reflectivity value is calculated by assuming the extinction coefficient $k = 0$ and calculating n through the interference fringes¹⁰ in the transmittance data by using

$$\Delta \nu = \frac{1}{2nd}, \quad (4.4)$$

where $\Delta \nu$ is the frequency distance between two maxima of the fringes in cm^{-1} , d the sample thickness in cm, and n the refractive index. $\Delta \nu$ is calculated by taking the average of at least 10 consecutive maxima in the low-energy sector. Once n is determined as a constant value, the reflectivity value is obtained using equation (3.10).

¹⁰The interference fringes are a result of multiple reflections inside the sample due to the smoothness of the interfaces after polishing.

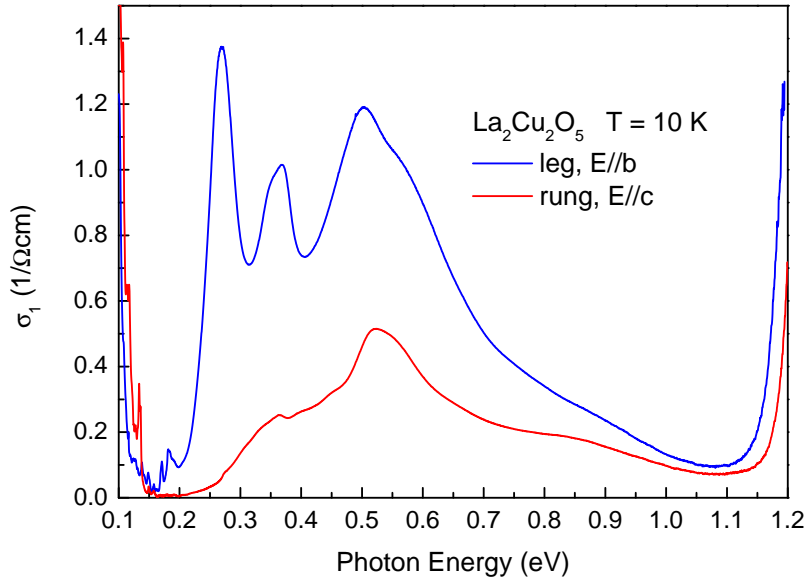


Figure 4.18.: Optical conductivity of $\text{La}_2\text{Cu}_2\text{O}_5$ for leg (blue) and rung (red) polarizations. Phonons can be clearly seen below 0.15 eV, whereas a clear electronic gap is observed above about 1.1 eV. In between, the magnetic excitations are present, showing distinctive behavior for both polarizations.

Once equipped with the measured transmission and calculated constant reflectivity, the set of equations (3.9) are used to obtain the optical conductivity, as shown in fig. 4.18 for both leg (blue) and rung (red) polarizations at 10 K. Strong phonon lines below 0.15 eV and a clear, steep electronic gap above 1.1 eV dominate the spectra at both ends. A tiny background contribution of about $0.1 \Omega^{-1} \text{cm}^{-1}$ can be observed at about 1.1 eV, indicating a good quality of the sample with few impurities and defects. The optical conductivity value is extremely low, not surpassing $1.5 \Omega^{-1} \text{cm}^{-1}$, as expected due to the only weakly allowed process. Three marked peaks are observed for leg polarization, at 0.27 eV, 0.37 eV, and 0.5 eV. The peak at 0.37 eV shows a soft shoulder at slightly lower energy (~ 0.35 eV), whereas the peak at 0.5 eV presents a more pronounced one at higher energy (~ 0.56 eV). For rung polarization, there is a small feature at about 0.36 eV and a clear one at 0.52 eV with a similar shoulder as for leg polarization. At even higher energy, at about 0.85 eV, there is a broad feature present in both polarizations. Drawing from what has been learned in the 2-leg ladder (cf. figs. 4.11 and 4.20), the magnetic contributions to the optical conductivity are clearly visible in the range 0.2 eV to 1.1 eV.

Figure 4.19 shows the optical spectra for different temperatures. As the tempe-

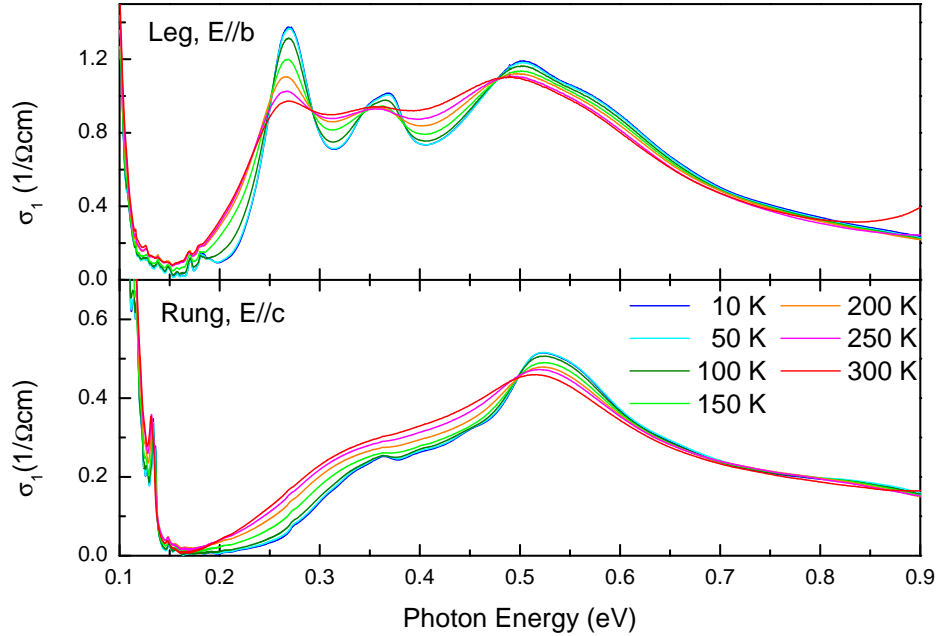


Figure 4.19.: Temperature-dependent optical conductivity of $\text{La}_2\text{Cu}_2\text{O}_5$ for leg (top) and rung (bottom) polarizations.

temperature increases, the features broaden considerably. Curiously enough, the temperature behavior measured differs substantially from the one reported for the 2-leg ladder $\text{La}_{5.2}\text{Ca}_{8.8}\text{Cu}_{24}\text{O}_{41}$ where substantial redistribution of spectral weight is observed [47].

4.4. Analysis

When comparing the results for 2- and 4-leg ladders, as shown in fig. 4.20, it is remarkable how similar they look. Qualitatively, there are some minor differences between them. For both polarizations, the spectra of the 4-leg ladder are slightly shifted to higher energies. In leg polarization, the optical conductivity in the 4-leg ladder is slightly lower than in the 2-leg ladder, while the broad high-energy feature shows a big difference. Part of that difference could originate from an overly aggressive background subtraction performed on the 2-leg ladder data [34, 47]. Interestingly, as noted in the previous section, the second prominent feature at about 0.35 eV shows a non-resolved double peak structure, which is absent from the 2-leg ladder measurement. In rung polarization, the main feature shows a more asymmetric profile, while only one peak-like structure is observed on the

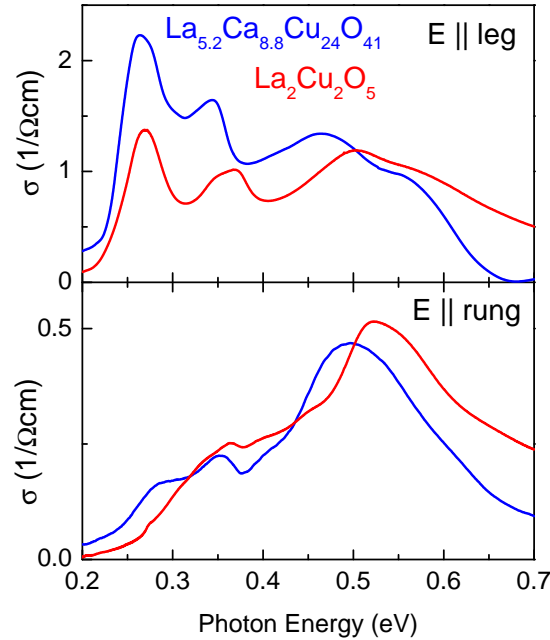


Figure 4.20.: Optical conductivity of the 2-leg ladder $\text{La}_{5.2}\text{Ca}_{8.8}\text{Cu}_{24}\text{O}_{41}$ [47] (blue) and the 4-leg ladder $\text{La}_2\text{Cu}_2\text{O}_5$ (red). For both polarization directions, there is a great degree of similarity on the features present in the optical spectra.

low-energy side.

It is tempting to interpret the 4-leg ladder features as having the same origin as in the 2-leg ladder, namely, to interpret the two peaks as signals from a bound state and the high-energy feature as contributions from a triplon continuum. However, without further theoretical support¹¹, such an interpretation is just wishful thinking because the jump from 2 to 4 legs can considerably change the physics involved.

Physically, due to the structure of the 4-leg ladder, we can expect at least four different couplings. These being $J_{\parallel 1}$ for the inner sites along the legs, $J_{\parallel 2}$ for the outer sites along the legs, $J_{\perp 1}$ for the inner sites along the rungs, and $J_{\perp 2}$ for the outer sites along the rungs, which is schematically shown in fig. 4.21.

To make it computationally tractable and to provide for a continuous transition from 2- to 4-leg ladders, the model Hamiltonian for a 4-leg ladder is written as two coupled isotropic 2-leg ladders showing identical coupling J in rung and leg

¹¹The discussion of the theory for 4-leg ladders to some extent follows [90–92] as part of a collaboration.

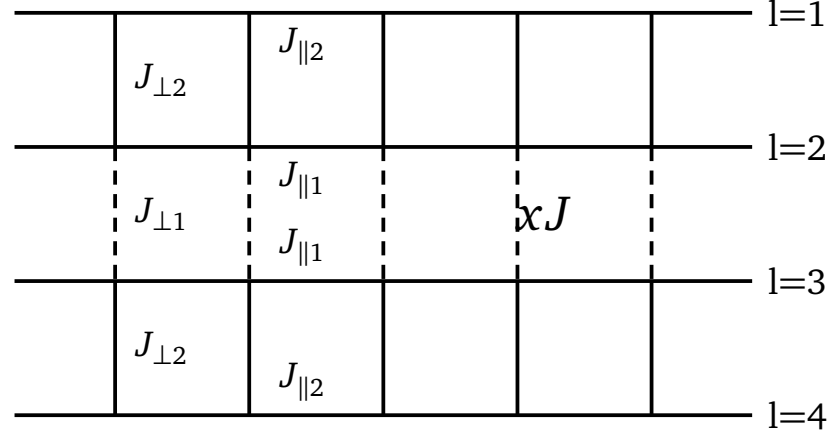


Figure 4.21.: Sketch of a 4-leg ladder system, showing four different couplings. In the case when $J = J_{\perp 2} = J_{\parallel 1} = J_{\parallel 2}$ and $J_{\perp 1} = xJ$ as written in eq. (4.5), two isotropic 2-leg ladders is obtained. As a function of x one can go from two independent 2-leg ladders to an isotropic 4-leg ladder. Adapted from [93]

directions and with a coupling ($J_{\perp 1} = xJ$), where x controls the strength of the coupling between the two 2-leg ladders [93]. The following equation gives such a model

$$H = J \sum_{l=1}^4 \sum_{i=1}^{N-1} \mathbf{S}_{l,i} \mathbf{S}_{l,i+1} + \sum_{i=1}^N [J \{ \mathbf{S}_{1,i} \mathbf{S}_{2,i} + \mathbf{S}_{3,i} \mathbf{S}_{4,i} \} + xJ \mathbf{S}_{2,i} \mathbf{S}_{3,i}], \quad (4.5)$$

where $\mathbf{S}_{l,i}$ is the spin-1/2 operator at leg index l and rung index i and can be seen in fig. 4.21.

In Nunner [93], the optical conductivity of the 4-leg ladder system was explored via exact diagonalization and DMRG methods for a 4×5 and a 4×16 ladder, respectively. As shown in fig. 4.22 for an isotropic 4×16 -site, the out-of-phase Cu–O bond stretching along the leg direction ($p_y = \pi$ open square) mode shows a broad and asymmetric contribution with a maximum at about $3.5J$. In the 2-leg ladder, the $p_y = \pi$ mode gives rise to the continuum sector and is slightly different, peaking at about $3J$ and showing a relatively symmetric profile (see fig. 4.11). The DMRG result for the in-phase Cu–O bond stretching along the leg direction ($p_y = 0$ filled circle) shows a prominent peak at about $2.4J$ plus a strong peak at about $2J$, which is located at slightly higher energy than the 2-triplon bound state of the 2-leg ladder.

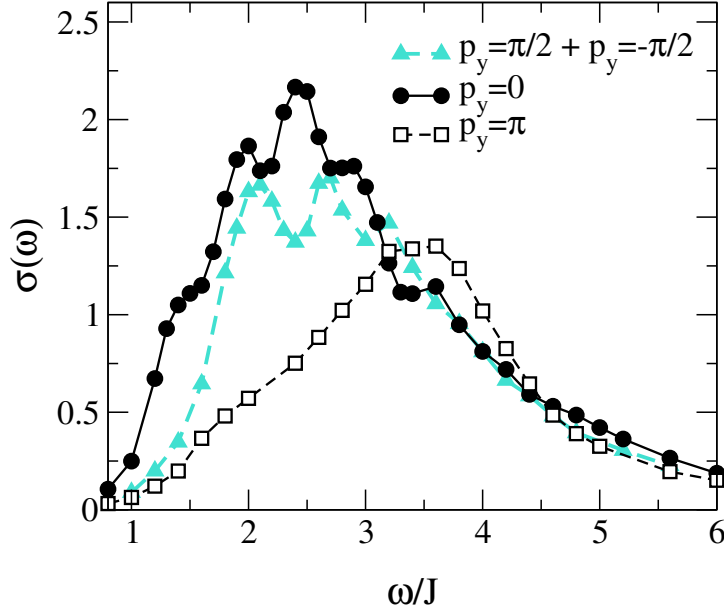


Figure 4.22.: Optical conductivity of an isotropic 4×16 -site 4-leg ladder obtained by DMRG method. $p_y = 0$ (filled circle), $p_y = \pi$ (open square), and $p_y = \pi/2 + -\pi/2$ (filled triangle). Reproduced from [93].

There are more features in the $p_y = 0$ mode of the 4-leg ladder than for the 2-leg ladder. Some of these observed features could arise from finite-size effects, particularly due to an expected relevance of it due to a reduced spin gap and enhanced correlation length when compared with the 2-leg ladder¹².

Tentatively, the interpretation given by Nunner [93] to the peak found at about $2J$ is as a 2-triplon bound state-like feature, a remnant of the 2-leg ladder. In comparison, the peak at about $2.4J$ is interpreted as a precursor of the bimagnon resonance of the 2D $S = 1/2$ square antiferromagnet. Thus, the $2J$ and the $2.4J$ features are assigned to spin-flip processes at the edges and center of the 4-leg ladder. One way to view this is to consider that in the Ising limit, the cost of flipping two neighboring spins at the edge of the 4-leg ladder is $2J$, while for the center spin-flip, the cost is $3J$. Although $2.4J$ is considerably smaller than $3J$, in the case of the 2D square lattice, the bi-magnon resonance is also found at a lower energy of $2.7J$ due to magnon-magnon interactions. Simultaneously, quantum fluctuations are expected to be stronger in the 4-leg ladder pulling the value even lower in energy.

¹²For the 4-leg ladder spin gap Δ_s and correlation length ξ are 0.190 [59] and 10.3 [61], respectively. In comparison, the values are 0.504 and 3.19 for 2-leg ladder [59]

To further complement the interpretation of our data, we collaborated with K. Cöster and K. P. Schmidt, who performed perturbative Continuous Unitary Transformation (pCUT) calculations, and S. Wessel who performed Quantum Monte-Carlo simulations (QMC) on 4-leg ladder systems. These two techniques are complementary as they cover distinct regimes of the interladder coupling x with different resolutions. The main idea behind perturbative continuous unitary transformations is to transform, in a continuous fashion, the basis of the Hamiltonian to find a more straightforward representation of the problem [94]. pCUT cannot explore the case for an isotropic 4-leg ladder, and the isotropic case is investigated by QMC calculations but offers a more constrained resolution. In Cöster [90], the values for x equal to 0.1, 0.3, and 0.5 were explored with the pCUT method, but here we will focus only on the $x = 0.5$ and the isotropic QMC case.

Since the Hamiltonian commutes with the reflection operator along the centerline, there are eigenstates of the Hamiltonian with even or odd parity. This means that the 4-leg ladder has two 1-triplon branches, one with even (+) and one with odd (-) parity. In the 2-leg ladder, there is no connecting matrix element between even and odd channels meaning that 1-triplon cannot decay into the 2-triplon continuum. The situation is slightly different for the 4-leg ladder. There, matrix elements that connect the 1-triplon to the 2-triplon channel allow the 1-triplon to decay into the 2-triplon continuum. This decay is only possible when the continuum's quantum numbers coincide with those for the 1-triplon dispersion.

Figure 4.23 shows the calculated dispersions of the odd (red) and even (black) 1-triplon branches and boundaries of the 2-triplon continua for the 4-leg ladder for the case $x = 0.5$. Both 1-triplon dispersions have similar shapes, but the odd triplon is at lower energy and shows a maximum at about $k = 0.3\pi$. The odd 1-triplon has very similar behavior to the one observed for the 2-leg ladder in section 4.1.2. Both triplons enter the continuum, but only the even-parity triplon (black line) crosses into the same parity 2-triplon continuum (red line) close to $k = 0.5\pi$. This means, a decay of the triplon is expected, but no indication of decay is observed in pCUT. One possibility for this is that a much too small perturbation order of the calculation was used [90].

To obtain the infrared absorption, the two-particle spectral densities are needed. The observable used for the $S = 0$ channel is $\mathbf{S}_i \mathbf{S}_j$ where i and j are nearest-neighbor spins. This leads to 4 observables in leg and 3 in rung polarization for a 4-leg ladder. Since the Hamiltonian has a symmetry about the centerline, it is convenient to express the observables in question with respect to such symmetry by taking linear combinations of the original \mathbf{S}_i operators. In the leg direction, the four contributions are labeled from 1 to 4, where 1 and 3 are the even (+) parity

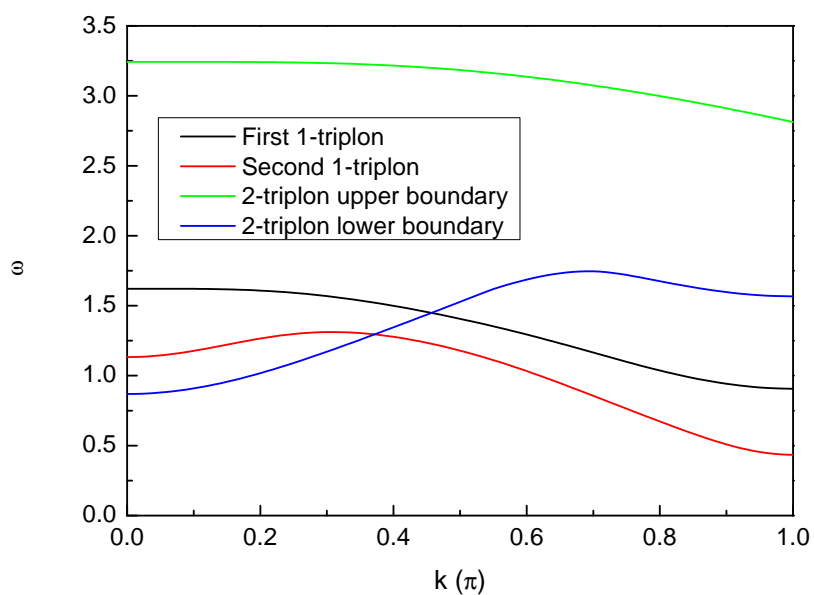


Figure 4.23.: Theoretical dispersion of the magnetic contributions of a 4-leg ladder with coupling $x = 0.5$. Due to symmetry, two different triplons are found with even (+) and odd (-) parity, shown in black and red, respectively. The green and blue lines are the 2-triplon upper and lower boundary, respectively, for the 2-triplon continuum for non-interacting triplons.

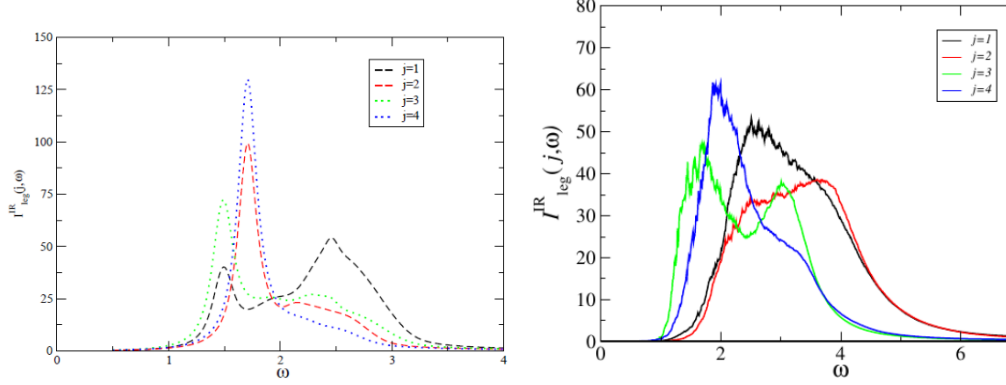


Figure 4.24.: Leg polarization IR spectra for pCUT $x = 0.5$ (left) and QMC $x = 1$ (right). The energy units are ω/J with $J = 1$. Reproduced from [90].

label (j)	parity	main contribution
1	+	continuum
2	-	
3	+	low-E bound state
4	-	high-E bound state

Table 4.2.: Summary of the spin observables along the legs, indicating their label, parity, and where their main contribution lays.

while 2 and 4 correspond to odd (-) parity states as summarized in table 4.2. This situation is radically different from the case of the 2-leg ladder.

Figure 4.24 shows the calculated contributions to the infrared absorption in leg polarization for each channel. For $x = 0.5$, the peaks between $1J$ to $2J$ arise from the 2-triplon bound state. The lower peak corresponds to even parity channels while the higher peak to the odd parity ones. The origin of the high-energy spectra is mostly arising from the 2-triplon continuum. When considering the QMC results for $x = 1$, a congruent picture emerges. There is a strong suppression of the 2-triplon bound states contribution for the inner operators while the spectral weight at higher energies is increased. Both channels show some structure, with a feature below $3J$ and another at about $4J$. The outer operators continue contributing as sharp features while also showing a marked (subtle) contribution at about $3J$.

Based on the pCUT, QMC, and DMRG results, our interpretation of the observed optical spectra for the 4-leg ladder in leg polarization is that the lowest-energy

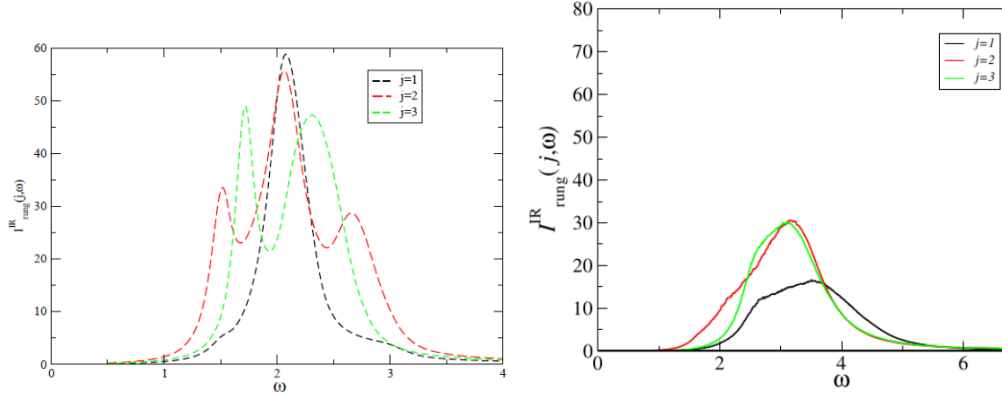


Figure 4.25.: Rung polarization IR spectra for pCUT $x = 0.5$ (left) and QMC $x = 1$ (right). The energy units are ω/J with $J = 1$. Reproduced from [90].

peak corresponds to a 2-triplon quasi-bound state. In contrast, the one above $4J$ corresponds to the continuum of excitations. The feature in between could arise from a high-energy quasi-bound state contribution as in the 2-leg ladder plus an incipient response from a bimagnon excitation.

The theoretical analysis shows that the 2-triplon bound state is more like a resonant or quasi-bound state that survives in the continuum, unlike the proper bound state in the 2-leg ladder. Thus the difference in the strength of the low-energy feature observed between the 2- and 4-leg ladders can be tentatively understood as a consequence of the resonant nature of the bound state in the latter.

Rung direction shows a more ambiguous situation as the evolution from pCUT to QMC is less clear. Shortcomings of the pCUT method like not considering higher particle channels, which are considered in QMC, could be a possible origin¹³. Regardless of this, the QMC result shows a high degree of resemblance with the observed data. The $j = 1, 2, 3$ channels show mostly contributions from the continuum while the $j = 2$ channel shows a shoulder at about $\omega = 2J$.

4.5. Discussion

As already discussed in section 4.1.3, the high-energy spectral weight in 2D at about $4J$ and above is still not well understood. Figure 4.26 shows the optical con-

¹³Already in the 2-leg ladder, the pCUT method is not capable of describing all the spectral weight of the triplon continuum since it only takes 2-triplon contributions into account whereas the continuum also shows contributions of all other $S = 0$ multiple-triplon excitations.

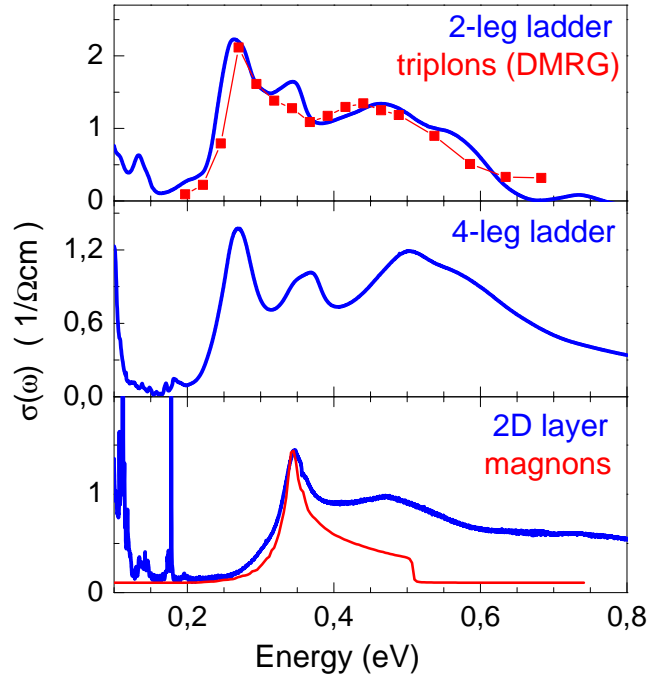


Figure 4.26.: Optical conductivity for a 2-leg, 4-leg ladder, and a 2D square layer. The energy is shifted by the phonon's energy involved in the bi-magnon-plus-phonon (BIMP) process and scaled by the effective exchange coupling. The contribution from the continuum stays roughly constant at about $2\nu SJ$. Adapted from [81].

ductivity of three different low-dimensional cuprates, namely, the 1D spin chain CaCu_2O_3 (top panel), 2-leg ladder $\text{La}_{5.2}\text{Ca}_{8.8}\text{Cu}_{24}\text{O}_{41}$ for leg polarization (middle panel), and 2D square layer $\text{YBa}_2\text{Cu}_3\text{O}_6$ (bottom panel) [81] together with their theoretical description based on a two-"magnon"-plus-phonon absorption process. The magnetic excitation corresponds to a spinon, triplon, and magnon for chain, ladder, and square layer, respectively. The spectra are shifted by the phonon frequency and scaled to make their comparison easier. The observed trend is that as the dimensionality increases from the chain to the square layer, the spectral weight is transferred to higher frequencies reflecting the increase in the number of nearest-neighbors spins ν in each of these system¹⁴. Grüninger et al. [81] observe that the chain, the 2-leg ladder, and the 2D square lattice all show a contribution from an incoherent continuum located at about $2\nu SJ$. Furthermore, they suggest that *"the position of the continuum thus may reflect the rather local nature of the incoherent excitations"*.

¹⁴For chain, 2-leg ladder, and 2D square layer there are 2, 3, and 4 nearest neighbors, respectively.

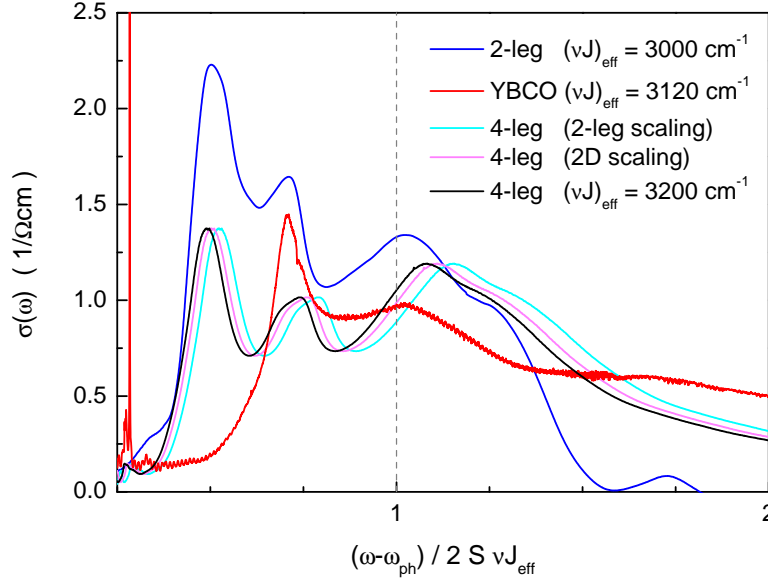


Figure 4.27.: Comparison of the optical conductivity for the 4-leg ladder, 2-leg ladder (blue), and 2D square lattice (red). The phonon shift for the 4-leg ladder is 0.071 eV (570 cm^{-1}), while three different scalings are shown. $(\nu J)_{eff} = 3000 \text{ cm}^{-1}$, 3120 cm^{-1} , and 3200 cm^{-1} . The 2-leg ladder and 2D square lattice are the same as shown in fig. 4.26.

In fig. 4.27, we compare the shifted and scaled optical spectra of the 4-leg ladder, 2-leg ladder, and 2D square lattice. For the 4-leg ladder, we have difficulty determining which values for ν and J should be chosen since both parameters are expected to lay somewhere between the values for the 2-leg ladder and the 2D square lattice. The 2-leg ladder has an effective νJ of 3000 cm^{-1} whereas the 2D square lattice has a value of 3120 cm^{-1} . Lines in cyan and pink in fig. 4.27 show the 4-leg ladder scaled by the effective νJ of the 2-leg ladder and the 2D square lattice, respectively. We can observe that the stronger scaling provided by $(\nu J)_{eff} = 3120 \text{ cm}^{-1}$ provides a better match of the pattern observed but is far from being satisfactory. Considering an even stronger scaling, $(\nu J)_{eff} = 3200 \text{ cm}^{-1}$, we observe a very good alignment, particularly of the second peak at about 0.37 eV with the bimagnon resonance of the 2D square lattice. Also, as seen for the other two cuprates, for the 4-leg ladder, we find a broad spectral weight at about $2\nu SJ$. If we assume that for the 4-leg ladder $J_{eff} \approx 900 \text{ cm}^{-1}$, slightly smaller to the one for the 2-leg ladder, then the effective ν would be of the order of 3.55.

Trying to extract detailed quantitative results from the comparison between

the measured spectra and the calculated one is not feasible. We have to keep in mind that the theoretical model used in DMRG, pCUT, and QMC is based on an isotropic ladder, which is a somewhat unrealistic assumption for a real system. Already in the successful description of the 2-leg ladder shown in section 4.1.2, an anisotropic coupling was needed besides the inclusion of a cyclic exchange (J_{cyc}) interaction. Adding to the difficulty, in the 4-leg ladder, there is a distinction between inner and outer legs leading to different exchange interactions, respectively. In the 2-leg ladder, J_{cyc} renormalizes the exchange interactions (J_{\perp} and J_{\parallel}) and adds a repulsive interaction between triplons on neighboring rungs reducing the binding energy of the bound state [75]. Thus, a better model would yield different shapes of the dispersion of the triplons, and thus their (quasi)-bound states would lead to different details emerging from the calculated infrared absorption spectra.

4.6. Conclusions

We successfully measured the first optical spectra of a $S = 1/2$ four-leg ladder. Somewhat surprisingly, the obtained spectra have a high degree of resemblance to the 2-leg ladder ones, indicating that some 2-leg character survives when increasing the ladder's number of legs. The similitude between 2- and 4-leg ladders prompts us to interpret the observed features in similar terms. Noteworthy is the presence of a broad contribution at high-energy, stemming from the triplon continuum of excitations. This further supports the interpretation of the high-energy continuum found above $4J$ in the 2D square layer systems.

With the guidance of theoretical calculations, we can interpret the optical spectra's features as follows. The first peak originates from a 2-triplon quasi-bound state. The broad feature above 0.4 eV comes from the continuum of magnetic excitations. For the feature at about 0.37 eV, which shows a clear peak plus a shoulder to the left, the origin is less clear. It could be originating from a combination of a higher-energy bound state and an incipient *bimagnon*-like resonance.

Moreover, the theory provides a consistent picture where contributions to the magnetic excitations can be distinguished between outer and inner legs in origin as schematically shown in fig. 4.16. The calculations show that the bound state signal's contributions come primarily from the outer legs, while the contributions to the continuum stem from the inner legs. This distinction is very interesting since the inner response should be more closely related to the 2D behavior and growing in relevance as wider ladders are considered.

Chapter 4: $\text{La}_2\text{Cu}_2\text{O}_5$: a 4-Leg Spin-1/2 Ladder System

However, drawing too many conclusions from the theoretical work is challenging due to the assumption of isotropic exchange interactions. This assumption deviates from the reality of the physical system as it is expected that the exchange interactions at the outer legs of the ladder are different. Also, the inclusion of cyclic exchange interactions is expected to influence the results considerably. Certainly, computational studies can be highly time-consuming, but we could profit significantly from more refined models considering anisotropic and cyclic exchange interactions.

n -leg ladders with $n \geq 3$ are never isotropic in real materials due to the different crystallographic sites and thus the potentials involved. With increasing n , the edge states may remain quasi-1D or ladder-like, while the inner part will resemble 2D. Our measurement shows that the 2D situation is already closely realized with $n = 4$.

5. Revisiting Magnetite

MAGNETITE (Fe_3O_4) is a natural permanent magnet known for its magnetic properties since ancient times. One of the earliest uses of magnetite lodestones was in compasses for navigation. In more modern times, derived materials like $\gamma\text{-Fe}_3\text{O}_4$ were employed in transformers, inductors, and magnetic recording applications. Nowadays, polycrystalline thin films of magnetite are of interest for spin electronics applications because of their magnetoresistive properties [95] or in nanowires of $\text{Au-Fe}_3\text{O}_4\text{-Au}$ heterostructures [96]. Beyond physics, magnetite is also of interest in mineralogy, geophysics, and biology. Magnetite is also a *biomineral* present in certain animals, providing a mechanism of magnetic sensing [97]. Small single-domain permanently magnetized magnetite crystals of about 50 nm have been found in bacteria, honeybees, and birds, among other animals. If allowed to rotate freely, they can align with Earth's magnetic field, providing what would be an inbuilt compass!

In condensed matter physics, this material is one of the most studied ones in the family of transition-metal oxides. Modern interest in this ancient mineral started with the first observations of a first-order transition in the magnetic susceptibility of synthetic polycrystalline magnetite. Later on, magnetite gained traction, when Verwey [21] found an abrupt change, by two orders of magnitude, in its electrical resistivity upon cooling down below what is now known as the *Verwey temperature*, $T_V \sim 123\text{ K}$, as shown in fig. 5.1. The Verwey transition also shows abrupt changes in other physical properties of magnetite as heat capacity, magnetization, and coercivity [99–101]. These properties are being explored for possible applications, for example, resistive switching [102], Fe_3O_4 -based tunnel junctions [103], and solid-state energy conversion devices [104].

One of the main reasons behind the extensive studies of the Verwey transition in magnetite is that it does not involve changes in its spin ordering. This fact simplifies a great deal the situation allowing a study of the electronic and lattice degrees of freedom without considering the behavior of the spins. Thus, magnetite was thought to be a good starting point to understand the mechanisms behind the metal-insulator transition in a broad class of materials. However, in the end, mag-

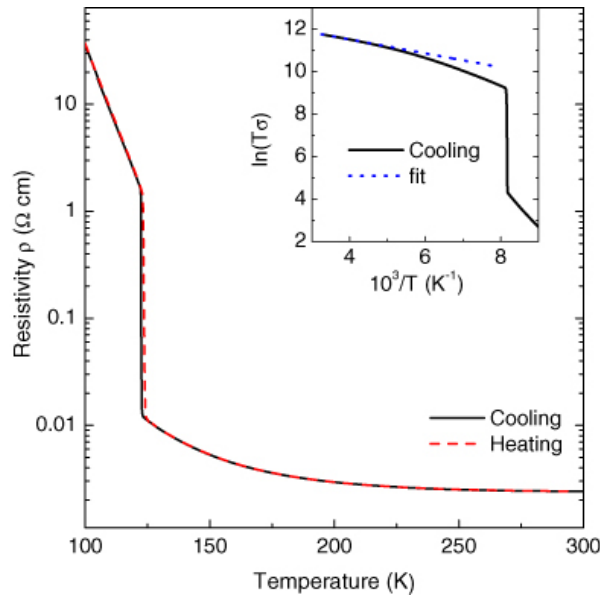


Figure 5.1.: The resistivity of magnetite shows a sharp change as a function of temperature at around 123 K. This temperature (T_V) marks the first-order metal-insulator transition, also known as the Verwey transition. Reproduced from [98].

netite is too complicated as a starting point to study the metal-insulator transition. The long history of the study of magnetite is summarized in a somewhat dated but very extensive review by Walz [105], which includes a particularly interesting historical perspective on the experimental and theoretical work accumulated over 90 years on this material.

The microscopic description of the mechanism behind this transition in magnetite has been a long-standing problem in condensed matter physics. Already in 1939, Verwey attempted a first microscopic description of this transition, arguing that a charge ordering takes place [21]. Since then, numerous theoretical and experimental studies have been performed to understand the mechanism behind the Verwey transition. Detailed investigations have shown a complex picture involving not only charge order but also orbital order in the low-temperature phase [106–114].

Quite recently [115], it has been suggested that originating from the charge and orbital order, a complex state that spreads over three neighboring sites emerges. These structures, called trimerons, form a network. Thus, the Verwey transition has been interpreted as a transition between a fixed trimeron network and a fluctuating one. The trimerons may be cataloged as *orbital molecules*, "locally coupled

5.1 Crystal, Magnetic, and Electronic Structure

orbital states on two or more metal ions within an orbitally ordered solid" [116]. Previously, two-electron "*orbital molecules*" have been found in compounds like CuIr_2S_4 [117] and MgTi_2O_4 [118]. Although charge and orbital orders are widely known in a broad range of transition-metal oxides, the inclusion of trimeron order turns magnetite into one of the most complex electron-ordered ground states known so far. This picture has rekindled the interest in studying this material.

Despite the relevance and long history of magnetite, precise and thorough optical investigations are still missing. Our motivation to study this material is threefold. First, it is triggered by a need for a solid starting point for non-equilibrium measurements on the same batch of samples. Second, to obtain a precise temperature dependence around T_V , which is still missing, and understand how the electronic structure changes as a function of temperature. Third, we want to dispel the disagreement and challenge the peak assignment found in the published literature on the optical spectroscopy of this venerable material.

As it will be shown in section 5.2, the temperature dependence of the features observed via optical spectroscopy has been addressed only on a qualitative level at the phase transition. Moreover, the literature disagrees regarding the behavior of the optical conductivity above 1.5 eV [30, 119]. This means that the temperature dependence, particularly around T_V is not clear. This chapter will present an overview of this material before showing detailed temperature-dependent optical spectroscopy results published in Randi et al. [120].

5.1. Crystal, Magnetic, and Electronic Structure

Magnetite crystallizes in an inverse spinel structure with space group $Fd\bar{3}m$ and formula AB_2O_4 with a lattice constant of 8.394 Å [121]. The inverse-spinel chemical formula consists of two different iron sublattices, A and B, distinguished by their point symmetry and their averaged Fe-O distance. Moreover, its chemical formula can be written as $\text{Fe}^{3+}[\text{Fe}^{2+}\text{Fe}^{3+}]\text{O}_4$ to show the nominal valence state of the A and B sites explicitly, mainly the mixed-valence state on the B site. The iron ions in the A and B sublattices form highly frustrated diamond and pyrochlore lattices with an average Fe-O distance of 1.8885(2) Å and 2.0582(1) Å in the cubic phase at 130 K, respectively [115].

The iron ions on the B sites are octahedrally coordinated (D_{3d}) by six oxygen ions and shown in blue in fig. 5.2, with a formal average valence $\text{Fe}_B^{2.5+}$ through an equal proportion of randomly distributed 2+ and 3+ iron cations. The ones on the A sites are tetrahedrally coordinated (T_d) by four oxygen ions and shown

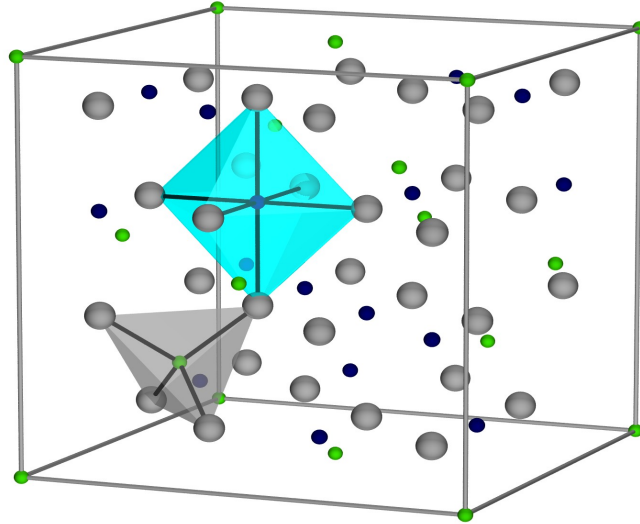


Figure 5.2.: Room-temperature unit cell of magnetite (cubic inverse spinel $Fd\bar{3}m$). Following the chemical formula of an inverse spinel AB_3O_4 , there are two iron sublattices, A and B, with point symmetries T_d and D_{3d} , respectively. The gray spheres are oxygen, green spheres are trivalent tetrahedrally coordinated iron Fe_A^{3+} , and blue spheres are octahedrally coordinated iron $Fe_B^{3+/2+}$. By David Schrupp, CC BY-SA 2.0 DE.

in green in fig. 5.2, with a formal valence Fe^{3+} . The electronic configuration of the Fe^{2+} ion is $t_{2g}^4 e_g^2$ with spin $S = 2$, while for the Fe^{3+} ions the electronic configuration is $t_{2g}^3 e_g^2$ with spin $S = 5/2$ as shown in fig. 5.3.

At the Néel temperature of ~ 858 K [122], magnetite goes through a transition between the para and ferrimagnetic states. Within the B sublattice Fe^{3+} and Fe^{2+} ions couple ferromagnetically, through a double exchange mechanism, whereas the Fe ions between A and B sites have an antiferromagnetic coupling through a common oxygen ion. Thus, for the total magnetic moment, only the unpaired spins in the Fe^{2+} in B sites result in ferrimagnetism, as exemplified in fig. 5.3. The extra minority-spin electron in the octahedral B sites (red arrow) delocalizes as illustrated in fig. 5.3 shown by the gray arrow. This delocalization renders the B sites structurally and spectroscopically equivalent and leads to a minority-spin-polarized electrical conductivity with a resistivity of about $4 \text{ m}\Omega \text{ cm}$ at 300 K as shown in fig. 5.1 [98].

The Verwey transition at about 123 K is a first-order phase transition as observed in heat capacity, conductivity, magnetization, and other measurements [3]. Early on, Verwey, Haayman and Romeijn [123] interpreted this transition as a

5.1 Crystal, Magnetic, and Electronic Structure

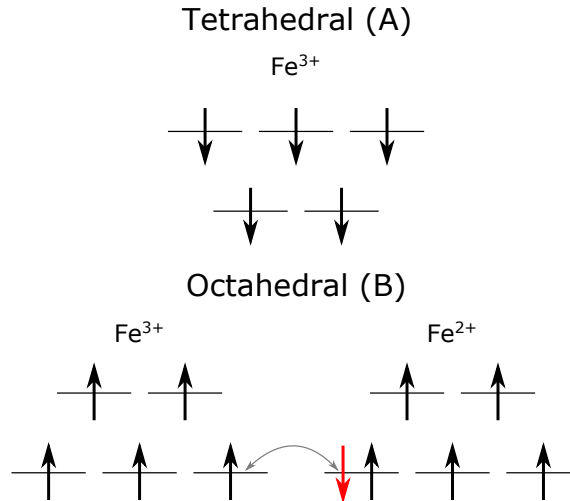


Figure 5.3.: The magnetic moments on the A site couple antiferromagnetically to the B site magnetic moments, whereas between B sites the coupling is ferromagnetic. These couplings give rise to ferrimagnetic ordering with a magnetic moment of about $4 \mu_B$. The extra minority-spin electron in the Fe_B^{2+} site, shown in red, delocalizes above T_V as shown by the light grey arrow, giving magnetite its half-metallic state with a resistivity of about $4 \text{ m}\Omega \text{ cm}$ at room temperature.

charge order-disorder transition of the Fe^{2+} and Fe^{3+} ions on the B sites, where the minority spin electron localizes. In this interpretation, the high-temperature metallic phase shows an equal number of Fe_B^{3+} and Fe_B^{2+} ions randomly distributed on the B sites. Upon cooling down, Fe_B^{3+} and Fe_B^{2+} layers were thought to stack in an alternating fashion along the $[001]$ direction to minimize Coulomb interaction leading to a charge-order scenario in agreement with the Anderson criterion¹ [124]. This interpretation had to be discarded as experimental evidence piled contradicting it, *e.g.*, observation of half-integer extra reflections at $(h,k,l+1/2)$ indicating a doubling of the unit cell along the c direction [125]. Nevertheless, it has been found that Verwey's hypothesis "*is correct to a useful first approximation*" [116]. Since the Fe_B ions form a frustrated pyrochlore lattice, the resulting charge-order superstructure is highly complex. This complexity reflects the competition between Coulomb interactions and the coupling to both lattice and orbital degrees of freedom [24, 126].

The low-temperature ground state has been a long-standing problem, mainly due to the difficulty of determining the crystal structure because of microtwin-

¹The *Anderson* criterion refers to minimizing electrostatic repulsion which in this case leads to a short-range charge order pattern.

ning² and the tremendous complexity of the crystals [115, 127]. For a long time, it has been known that below T_V , the crystal undergoes a complex lattice distortion showing a monoclinic $\sqrt{2} \times \sqrt{2} \times 2$ superstructure of the cubic room-temperature lattice [106] where the cubic cell is elongated and tilted along the $[111]_c$ direction³. The resulting supercell contains 224 atoms and belongs to the Cc space group. It contains eight crystallographically independent tetrahedral A sites and 16 octahedral B sites. The lattice parameters for the low-temperature structure are $a = 11.8802(24)$, $b = 11.8389(25)$, $c = 16.7671(29)$ Å, and $\beta = 90.167(5)^\circ$ [126].

Quite recently, Senn, Wright and Attfield [115] reported a high-quality X-ray refinement of the full low-temperature structure by using a small, almost single-domain⁴ grain of the order of 40 μm . They propose that $\text{Fe}^{2+}/\text{Fe}^{3+}$ charge ordering and Fe^{2+} t_{2g} orbital ordering due to the Jahn-Teller distortions of the Fe^{2+}O_6 octahedra explain the observed interatomic distances, consistent with previous calculations [128, 129]. Furthermore, they estimate that the formal oxidation states for the eight Fe^{2+} and Fe^{3+} ions on the B sites are 2.47 and 2.75, respectively. This means that the disproportion of charge is $0.28 e$ in agreement with the value of $0.23 e$ as found by Leonov et al. [130] via LSDA+U method.

Moreover, they argue that a network of three-Fe-site distortions emerges. In these three-site distortions called *trimerons*⁵, due to anomalously shortened Fe-Fe-Fe structures, the single minority \downarrow electron of a central Fe_B^{2+} ion delocalizes over the neighboring outer Fe_B^{3+} sites, forming a linear object [115, 116]. Since only two B site Fe ions per minority-spin electron are available, trimerons are forced to share sites and thus form a network. This trimeron lattice tends to equalize the charges on the Fe_B sites and increases the polarizability [131].

Concerning the band structure and total density of states, the result of a self-consistent calculation using LSDA+U for a tentative $P2/c$ low-temperature structure of magnetite with parameters $U = 5$ eV and $J_H = 1$ eV is shown in fig. 5.4. It reproduces the expected insulating behavior correctly. The calculated band gaps in the minority (indirect) and majority (direct) spin bands are 0.18 eV and 2 eV, respectively. For the chosen parameters, the 0.18 eV gap agrees well with experimentally determined values, as discussed below [130]. In the minority spin band (upper panel of fig. 5.4), just below the Fermi level, a predominately Fe_B^{2+} t_{2g}

²In contrast to the cubic axes of the high-temperature phase, the low-temperature Cc cell has 24 unique domain orientations.

³The subscript c refers to the high-temperature cubic unit cell.

⁴In the best quality sample measured, Senn, Wright and Attfield [115] report 89% scattering from a single orientation.

⁵A trimeron is a highly structured three-site polaron. They can be regarded as orbital molecules.

5.1 Crystal, Magnetic, and Electronic Structure

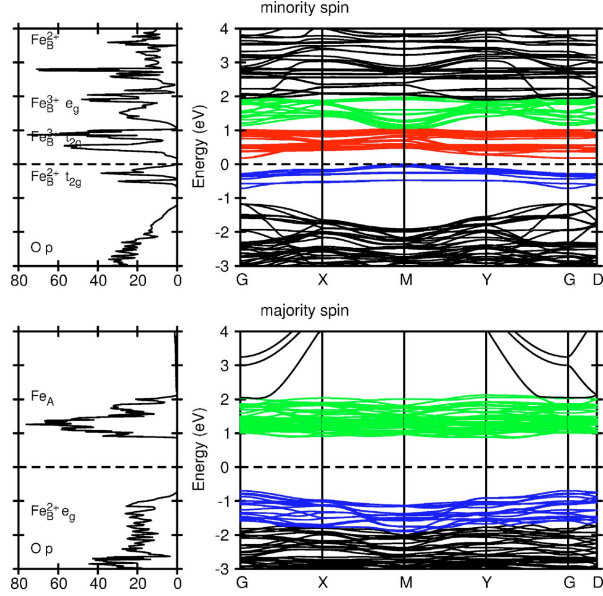


Figure 5.4.: Total density of states (left panels) and band structure (right panels) of the tentative $P2/c$ low-temperature phase. A bandgap of 0.18 eV and 2 eV is obtained for the minority and majority spins, respectively. The horizontal dashed line indicates the Fermi level, designed as zero energy. Upper: minority spin. Red and green bands originate primarily from $\text{Fe}_B^{3+} t_{2g}$ and e_g states, whereas the bands in blue come from $\text{Fe}_B^{2+} t_{2g}$ states. The gap opens between Fe_B^{3+} and $\text{Fe}_B^{2+} t_{2g}$ bands. Lower: majority spin. In blue, the $\text{Fe}_B^{2+} e_g$ state bands, and in green, the ones for Fe_A are shown, where a gap between both states opens. Among the occupied states, the minority electron in the t_{2g} level of a Fe_B^{2+} site is the closest to the Fermi level. In contrast, the lowest unoccupied states were identified as the empty $t_{2g} \downarrow$ states of Fe_B^{3+} sites. Reproduced from [130].

band is found (blue), while above it $\text{Fe}_B^{3+} t_{2g}$ (red) and e_g (green) bands are found. When using the Cc refined structure, a similar result for the band structure and density of states is found [116]. Furthermore, Senn et al. [116] find that the spatial distribution of the minority spin is consistent with charge ordering and orbital ordering at the Fe_B^{2+} sites. They further support the trimeron formation picture by observing a significant transfer of the minority-spin electron density to Fe^{3+} together with variations in the density between neighboring B site ions.

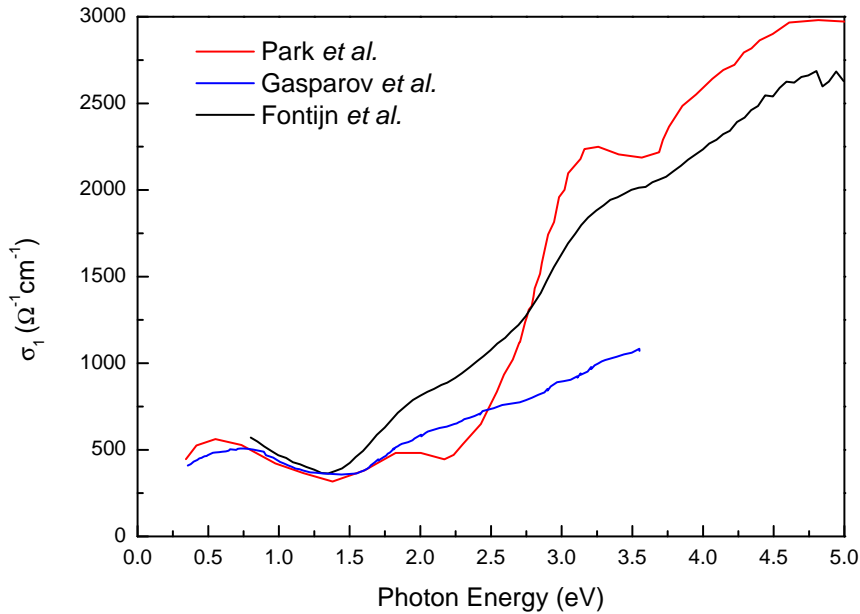


Figure 5.5.: The real part of the optical conductivity of Fe_3O_4 at room temperature. The three measurements show a similar behavior below 1.5 eV, where a broad mid-infrared feature is observed. Adapted from [30, 119, 132].

5.2. Optical Spectroscopy

The optical spectra of magnetite have been studied via spectroscopic ellipsometry [132] and via Kramers-Kronig analysis of reflectivity data [30, 119, 133]. Figure 5.5 shows the real part of the optical conductivity $\sigma_1(\omega)$ for all three measurements at 300 K. Park, Ishikawa and Tokura [30] (fig. 5.5 in red) report that, below 2.5 eV, σ_1 is dominated by two distinguishable features at about 0.6 eV and 1.9 eV. Fontijn et al. [132] (fig. 5.5 in black) also find features at 0.6 eV and 1.9 eV, although the second one is more subtle and with a larger spectral weight. In contrast, Gasparov et al. [119] (fig. 5.5 in blue) discern only the 0.6 eV feature, whereas the second one is mostly lost in the background of higher-energy excitations and not addressed. Above 2.5 eV, Park, Ishikawa and Tokura [30] and Fontijn et al. [132] show strong absorption originating from charge-transfer excitations but again reflectivity provides more marked features, e.g., at about 3.2 eV.

The temperature-dependent optical spectra obtained by Park, Ishikawa and Tokura [30] and Gasparov et al. [119] are shown in figs. 5.6 and 5.7. Both studies use a Kramers-Kronig analysis of reflectivity data and display a broad Drude re-

sponse above T_V , *i.e.*, a metallic phase with delocalized carriers. Below the metal-insulator transition temperature T_V , both figures show a strong suppression of this Drude response in agreement with DC resistivity measurements [30].

Regarding the first feature at about 0.6 eV, its spectral weight increases when decreasing the temperature from 490 K to 290 K (see fig. 5.6). Upon further decrease, this feature sharpens while the low-energy spectral weight diminishes. Figure 5.7 shows qualitative agreement with this behavior.

The second feature at about 1.9 eV presents some differences between the two reflectivity measurements. Park, Ishikawa and Tokura [30] observe that the feature shows a shift to higher energies while also lowering the total spectral weight as the temperature is decreased, and they assign it to a $\text{Fe}^{3+} \rightarrow \text{Fe}^{2+}$ between A and B sites. However, Gasparov et al. [119] find no clear temperature dependence as this feature is virtually non-existent. Moreover, there is not only a temperature dependence across T_V but also above it, for both features shown in fig. 5.6.

Thus, the open question is what exactly is the origin of these features in the optical conductivity spectra.

5.3. Measurements and Results

A Fe_3O_4 sample⁶ was oriented in a [100] direction and prepared as described in section 3.2. Optical spectroscopic data were acquired in the range 0.75 eV to 3.5 eV as a function of temperature with a particular focus around the phase transition at T_V . For the analysis of the ellipsometry data, cubic symmetry was considered. Concerning the surface roughness, an independent estimate of it was not possible to obtain because the sample did not show any non-absorbing region in the measured range. The ellipsometric result for ϵ_2 at 300 K as obtained by a point-by-point fit of the data and considering different thicknesses for the surface roughness are shown in fig. 5.8. Regardless of the thickness used, a strong absorption at the low-energy side, a shoulder at about 2 eV, and a broad feature at about 3.2 eV are observed. With increasing thickness, the valley at about 1.5 eV deepens while shifting to higher energies. Likewise, the feature at about 2 eV also shifts to higher energies and is pulled down. At about 2.8 eV, the trend changes and the absorption is enhanced. For reference, the data for undoped Fe_3O_4 and slightly Al-doped samples from Fontijn et al. [132] are also shown. For the remainder of the analysis, a surface roughness of 4 nm was used as a

⁶Same sample as used in non-equilibrium optical studies [120, 134].

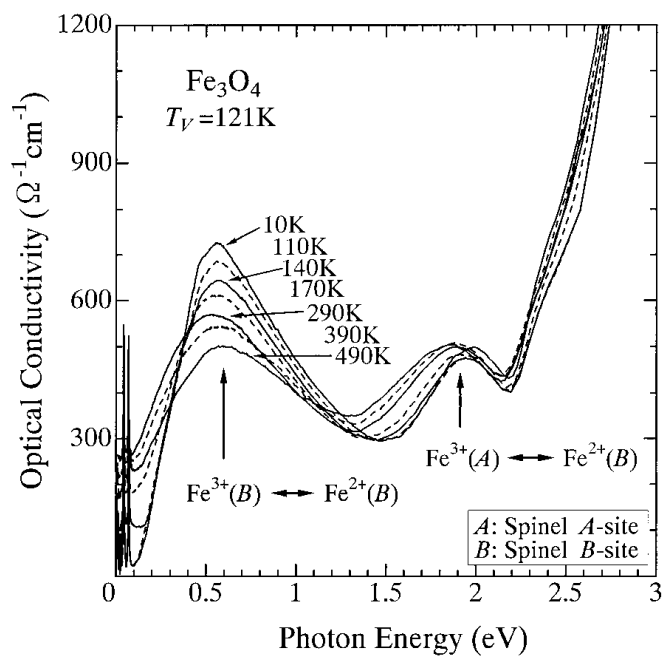


Figure 5.6.: Temperature dependence of the optical conductivity of Fe_3O_4 in the region below 3 eV as obtained through Kramers-Kronig analysis of reflectivity data. The features are interpreted as intersite transitions originating from the $\text{Fe } t_{2g}$ electrons on the B sites, for the one at 0.6 eV, and between the A and B sites for the one at 1.9 eV. Reproduced from [30].

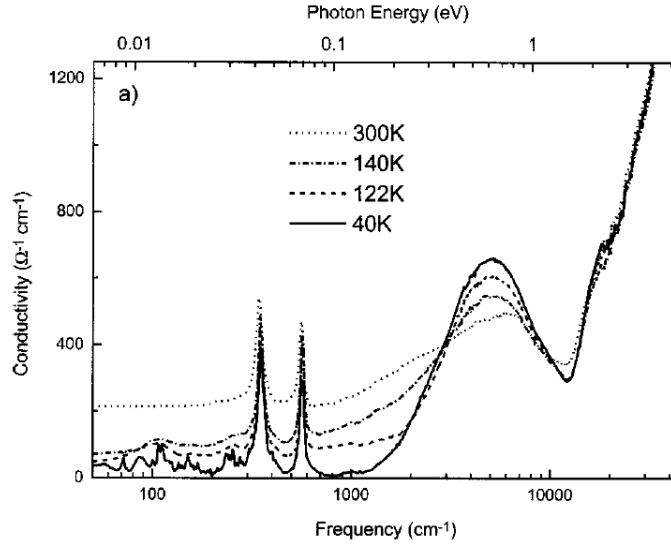


Figure 5.7.: The optical conductivity of Fe_3O_4 shows a broad temperature-dependent feature peaking at about 0.62 eV (5000 cm^{-1}). The measurement shows clearly the suppression of the conductivity below 0.12 eV (1000 cm^{-1}) at temperatures below T_V . Reproduced from [119].

conservative value that shows a reasonable match with the data of Fontijn et al. [132] and also aligns with values used in previous research [31, 135].

Figure 5.8 also shows the dielectric function reported by Fontijn et al. [132] for undoped Fe_3O_4 (black dashed line) and for 2% Al substitution at the Fe_B^{3+} site (black dotted line). Both measurements qualitatively agree in their significant features. However, for the undoped sample in the range 1.5 eV to 3 eV Fontijn et al. [132] report a more moderate absorption and show more prominent features at around 2 eV and 3.2 eV .

Even though the ellipsometry data shows some uncertainty concerning the precise absolute value of the spectral weight due to the sensitivity to the surface roughness, it provides an excellent determination of the temperature dependence. The temperature dependence of the optical spectra, fig. 5.9 shows the result of a point-by-point fit of the ellipsometric data in the form of σ_1 and ε_1 for selected temperatures between 15 K and 300 K using a 4 nm surface roughness layer. A clear distinction between high- and low-temperature phases is observed. In particular, an abrupt change occurs across T_V . This change is most clearly visible in the sharp upturn in ε_1 for the low-temperature phase at the spectra's low-energy side. Broadly, there is good agreement with previous temperature-dependent results based on Kramers-Kronig analysis of reflectivity measurements [30], as shown in

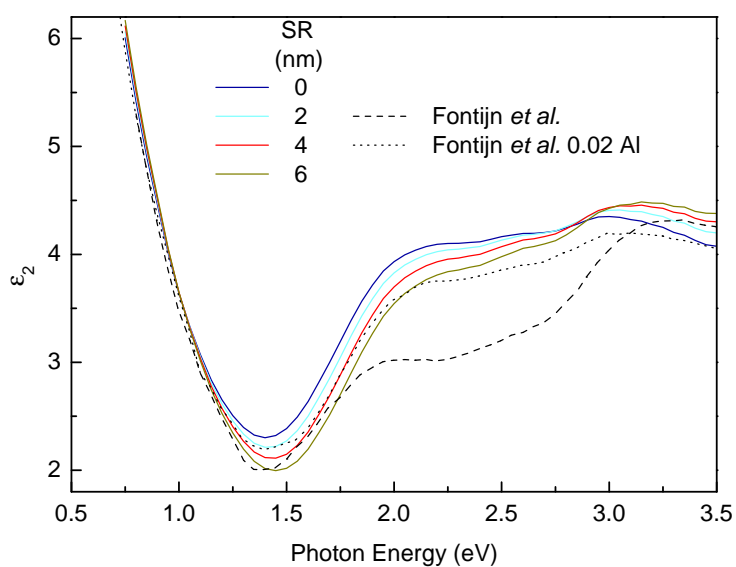


Figure 5.8.: The imaginary part of the dielectric function of Fe_3O_4 at room temperature obtained by a point-by-point fit with different thickness of the surface-roughness layer. Two higher-energy features can be discerned at about 2 eV and 3.2 eV. For comparison the results by Fontijn et al. [132] for undoped Fe_3O_4 (black dashed line) and a slightly Al-doped sample (black dotted line) are also shown. The difference between both measurements is most pronounced at around 2.0 eV until about 3.0 eV, where the undoped sample shows a reduced absorption and more prominent features.

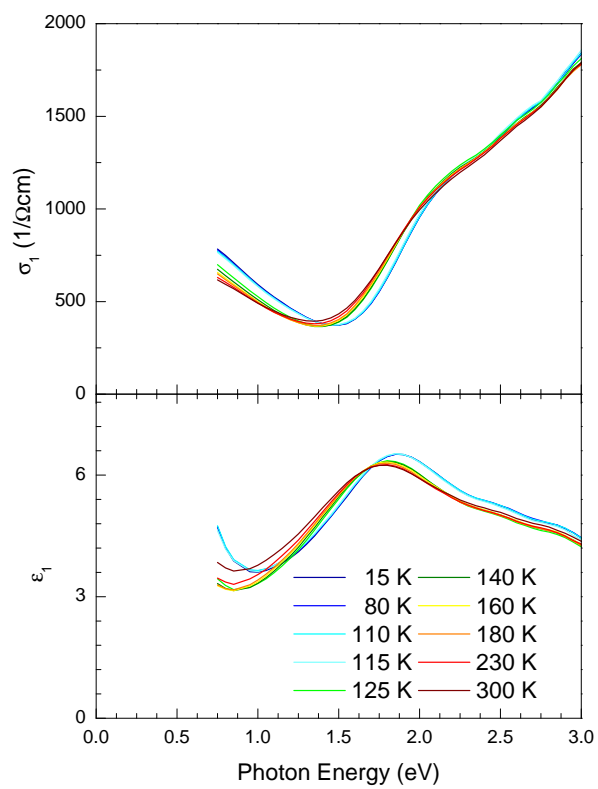


Figure 5.9.: Real parts of the optical conductivity (top) and the dielectric function (bottom) of Fe_3O_4 for selected temperatures. Most of the changes occur below 2.5 eV.

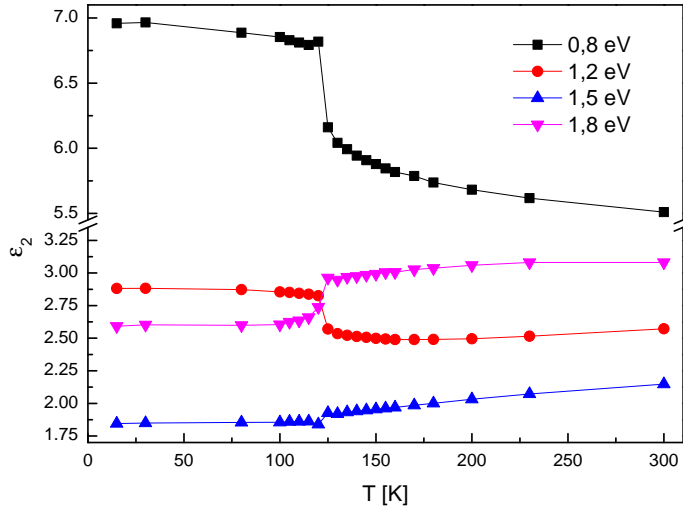


Figure 5.10.: Constant-energy cuts of the measured imaginary part of the dielectric function obtained by a point-by-point fit shown for all measured temperatures. At T_V a kink is observed in all 4 curves clearly indicating the change of the electronic structure at the metal-insulator transition.

fig. 5.6, where most of the changes with temperature happen below 2.5 eV.

To better get a grasp of the temperature dependence, fig. 5.10 plots $\sigma_1(T, \omega_0)$ at four selected energies (ω_0) showing an evident steplike change at T_V , a fingerprint of a change in the electronic structure across the Verwey transition. This pronounced effect of the phase transition on the electronic structure has not been revealed in previous optical studies with very coarse temperature steps. Besides the step-like change, the optical conductivity keeps evolving as the temperature is increased above T_V , particularly noticeable at 0.8 eV.

We want to better interpret and understand the observed features and the temperature dependence, and to this effect, we build an optical model. Moreover, since the low-energy excitation at 0.6 eV (compare fig. 5.8 with figs. 5.6 and 5.7) is only partially covered by the measurement, an optical model enables us to estimate values of the optical constants at lower energy. These were relevant for the non-linear experiments described in [120].

To construct the optical model, we consider the results for the DC measurements to set a Drude contribution. We constrain the parameters of the Drude contribution by using published DC conductivity data to set the amplitude of the oscillator. As for the oscillator used to describe the main feature at about 0.6 eV, early modeling efforts showed a strong asymmetry of this feature, which made it challenging to describe reliably with two Gaussian or Lorentzian oscillators. Such

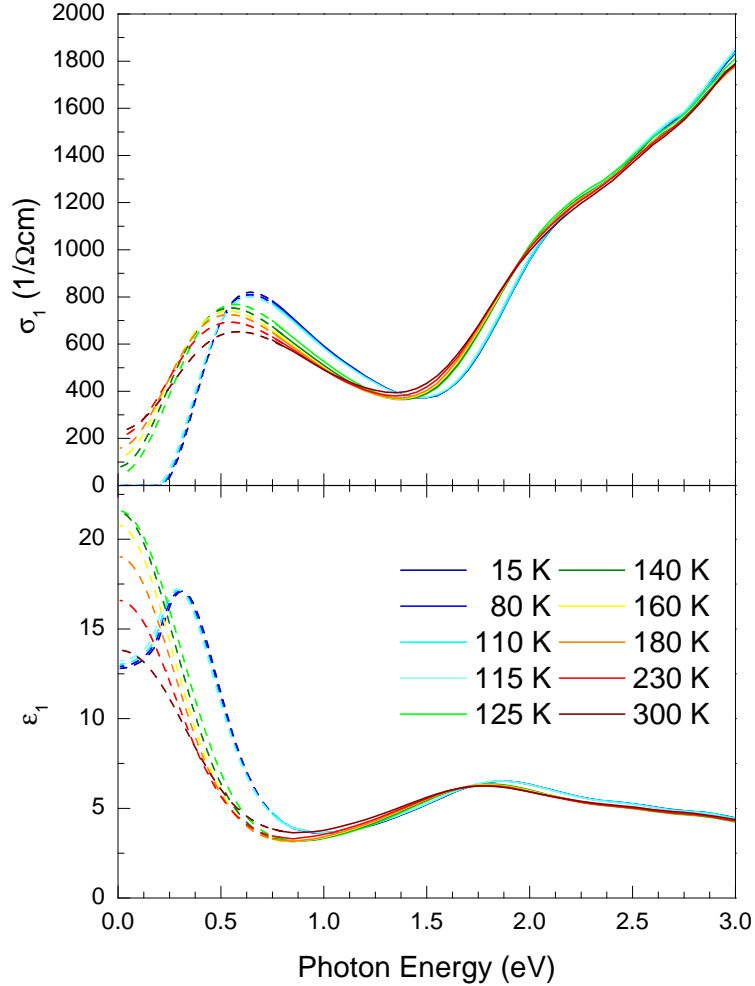


Figure 5.11.: Real parts σ_1 (top) and ϵ_1 (bottom) of Fe_3O_4 for selected temperatures obtained by direct inversion (continuous lines) of the measured data. Additionally we plot the low-energy extension by an optical model (dashed lines). The opening of a gap below T_V gives rise to a peak in ϵ_1 at about 0.3 eV. The model contains a Drude contribution above T_V , a Tauc-Lorentz oscillator describing the 0.6 eV feature, and several Gaussians describing the shoulder at about 2 eV as well as other charge-transfer transitions. Due to the availability of two Kramers-Kronig-related measured values and the knowledge of the DC properties, a reliable fit of partially measured features can be achieved (see main text).

a scenario would yield six highly coupled parameters. Moreover, since the 0.6 eV feature corresponds to the gap in the insulating phase, a Tauc-Lorentz lineshape was used to describe it, reducing from six to four parameters the modeling of the feature. The fact that the feature has a large contribution in the measured range and that we obtain ε_1 and ε_2 makes it possible to derive reasonable results with this (see section 3.4.3).

In fig. 5.11, the real parts of the optical conductivity (σ_1) and of the dielectric function (ε_1) are shown for selected temperatures, extended at the low-energy side with the result of an oscillator-based model. Due to the lack of far-infrared data, the Drude contribution parameters were fixed at each temperature as follows. Above T_V , the reported DC conductivity σ_{DC} of about $270 \Omega^{-1} \text{cm}^{-1}$ for the room-temperature data of Park, Ishikawa and Tokura [30] and a suitable temperature-independent value for the scattering time τ were chosen. Below T_V , the Drude contribution's spectral weight was set to zero in agreement with the insulating behavior.

Figure 5.12 shows the profound effect that the Tauc-Lorentz oscillator has in the optical spectra of the 300 K measurement. Even when such an oscillator is partially located below the experimental window, it strongly influences the optical properties within the measured range.

At 1.9 eV, a Gaussian oscillator describes the upturn in the optical spectra, while at energies above 2 eV, a collection of four Gaussian oscillators describes higher-energy contributions to the optical absorption located at 2.29 eV, 2.6 eV, 2.89 eV, and 3.69 eV. In the optical model, a pole at 7 eV with a magnitude of 87 eV, a Gaussian at 6 eV describing the background, and $\varepsilon_\infty = 1$ were kept fixed during all the fitting procedures.

Figure 5.13 shows the spectral weight for some of the oscillators used in the model. With increasing temperature above T_V , the spectral weight of the Drude contribution associated with the delocalized carriers (downward red triangles) increases following the change in DC resistivity, whereas the spectral weight of the 0.6 eV Tauc-Lorentz feature decreases (upward red triangles). The loss of spectral weight in the Tauc-Lorentz oscillator is mostly compensated by the increase in the Drude one, as shown for the sum of both spectral weights (open squares) as it shows no temperature dependence. This is in agreement with the Kramers-Kronig results of Gasparov et al. [119], who report that the spectral weight is relatively independent of temperature below 0.8 eV, further confirming the reliability of our model. The continuous evolutions of both the Drude and the Tauc-Lorentz oscillators spread to temperatures far above T_V . This behavior has been attributed to short-range charge order [30]. Concerning the 1.9 eV feature (green squares), its

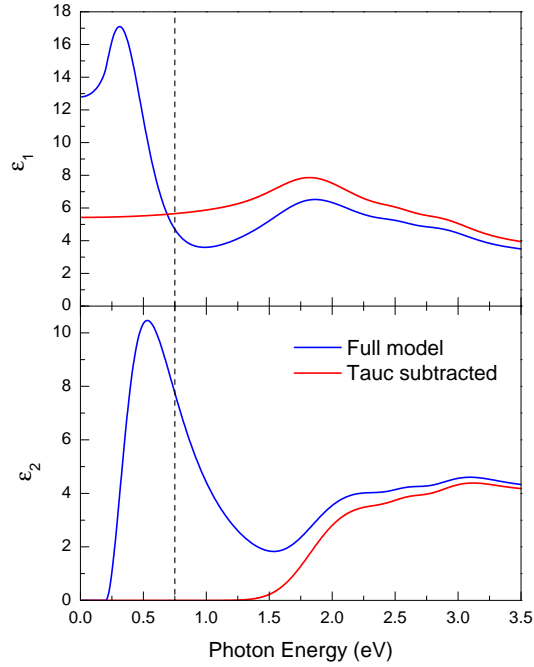


Figure 5.12.: Full model (blue line) compared to the same model but with the Tauc-Lorentz contribution removed (red line) based on the 300 K measurement. The dashed line indicates the lower limit of the measured data.

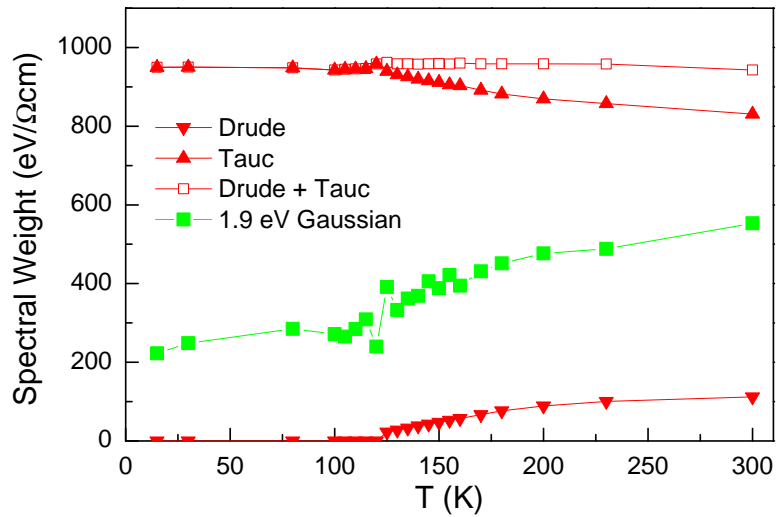


Figure 5.13.: Above T_V , some carriers become delocalized, which leads to an increase of the low-energy spectral weight of the Drude oscillator (downward triangles) and a reduction of the spectral weight of the Tauc-Lorentz oscillator (upward triangles). The sum of the Drude and Tauc-Lorentz spectral weights (open squares) is nearly temperature independent.

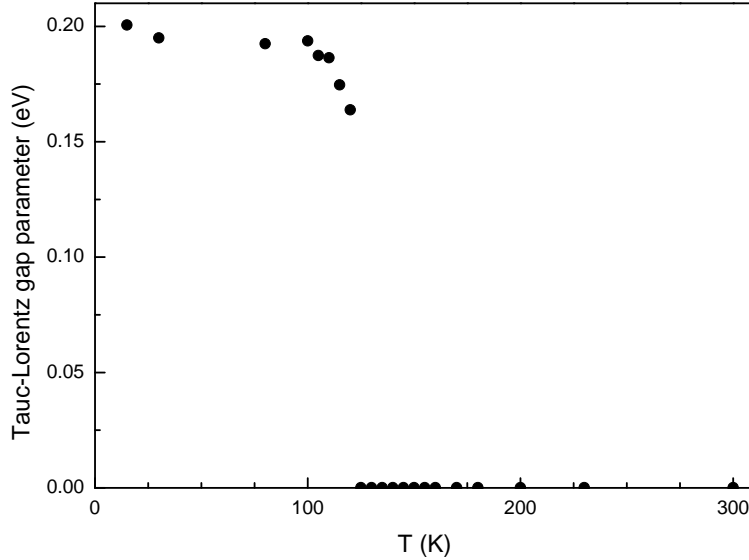


Figure 5.14.: Estimated band gap of the Tauc-Lorentz oscillator as a function of temperature. At 15 K, a value of $\Delta = 0.2$ eV is obtained in agreement with experimental [30, 119] and theoretical [130] results. Above T_V , the fit yields a gap of 0 eV as expected for the metallic phase of magnetite.

spectral weight shows a steady increase as a function of temperature in agreement with the behavior observed by Park, Ishikawa and Tokura [30].

The Tauc-Lorentz oscillator used in the model to account for the 0.6 eV feature estimates the value of the bandgap deep in the insulating phase at about $\Delta_{15K} = 0.2$ eV (see fig. 5.14). This value is in agreement with the values reported by Gasparov et al. [119], Park, Ishikawa and Tokura [30], and Leonov et al. [130] namely, 0.18 eV, 0.19 eV, and 0.14 eV. At T_V , the fitted band gap parameter goes to zero as expected for the metallic behavior in the high-temperature phase.

Now, we address the assignment of the features observed in the optical spectra to electronic transitions. For charge-transfer excitations ($O_{2p} \rightarrow Fe_{3d}$), the spectral weight tends to be bigger than the one originating from excitations between Fe_{3d} states. In magnetite, these strong excitations set in at about 2.5 eV [30, 130]. This leads to attribute the observed features at 0.6 eV and 1.9 eV to excitations between Fe_{3d} states. Due to two different sites, A and B, and two iron oxidation states ($2+/3+$) on the B sites, a multitude of excitations is possible. Considering first intersite excitations of the type $3d_i^5 3d_j^5 \rightarrow 3d_i^4 3d_j^6$, the high spin $S = 5/2$ $3d^5$ configuration is very stable such that those excitations are commonly found above 3 eV [135]. Hence, the features observed at 0.6 eV and 1.9 eV can be reasonably identified as $3d_i^6 3d_j^5 \rightarrow 3d_i^5 3d_j^6$ excitations.

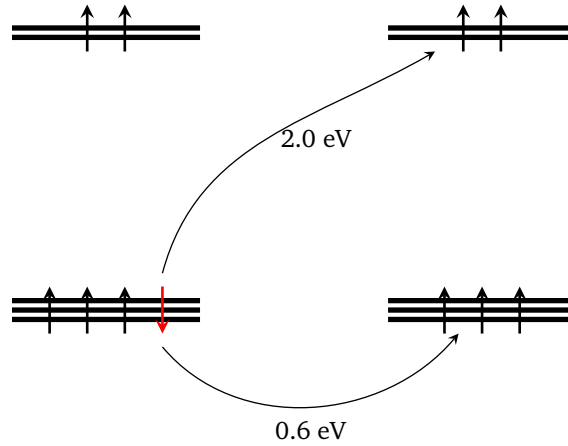


Figure 5.15.: Sketch of the assignments of the two intersite excitations observed at 0.6 eV and 2.0 eV, originating from the minority spin electron in the Fe_B^{2+} as shown in red, as observed in the optical spectra.

As described earlier, Leonov et al. [130] find (see fig. 5.4) that the minority electron in the t_{2g} level of the Fe_B^{2+} site is the closest to the Fermi level whereas the lowest empty one is identified as a $t_{2g} \downarrow$ state on Fe_B^{3+} . Thus, the peak at 0.6 eV can be assigned to the intersite excitation between those two states, in agreement with previous reports [30, 119, 130].

Since in magnetite, neighboring Fe_B sites are connected via 90° Fe-O-Fe bonds, not only the intersite $t_{2g} \rightarrow t_{2g}$ hopping is allowed but also the intersite $t_{2g} \rightarrow e_g$ hopping is allowed [24], as sketched in fig. 5.15. Again, Leonov et al. [130] find a minority spin $\text{Fe}_B^{2+} t_{2g}$ electron excitation to an empty e_g state on an Fe_B^{3+} site at about 2 eV. This assignment is different than the one in Park, Ishikawa and Tokura [30], which assigns this peak in the optical conductivity to a $\text{Fe}^{3+} \rightarrow \text{Fe}^{2+}$ transition within A and B sites

Since both features originate from the excitation of a minority electron on an Fe_B^{2+} site to an Fe_B^{3+} site, the expectation is that both excitations show the same temperature dependence regarding their spectral weight. Our experimental result disagrees with this expectation, as the two features show an opposite behavior in their temperature dependence (see fig. 5.13). However, Leonov et al. [130] find that below T_V , Fe_B^{3+} sites have an enhanced occupation of the $e_g \downarrow$ arising from hybridization with O_{2p} states. This means that a change of covalency strongly screens the charge order below T_V . Therefore, the spectral weight for excitations into the e_g levels diminishes in the charge-ordered state, in agreement with our observation.

5.4. Conclusions

We performed temperature-dependent measurements of the equilibrium optical properties of magnetite in a broad spectral range. The optical spectra show good qualitative agreement with previously reported optical data [30, 119, 132, 133] but offer more insight into the temperature dependence. Like those previous reports, we observe that the two lowest-energy electronic absorption features⁷ are located at 0.6 eV and 1.9 eV.

A detailed measurement of the optical response around the Verwey transition temperature, *i.e.*, across the charge-ordered and charge-disordered phases, shows a steplike behavior. Our temperature-dependent measurements permitted us to determine the behavior of the spectroscopic features at 0.6 eV and 1.9 eV, which was unclear from previous optical studies [30, 119]. We observe that the two features show an opposite temperature dependence, in agreement with what was reported by Park, Ishikawa and Tokura [30].

By considering their temperature-dependent behavior, we interpret those excitations in a new fashion that differs from previous reports. Our interpretation of both features is as intersite transitions of minority spins from the $\text{Fe}_B^{2+} t_{2g}$ levels to the t_{2g} and e_g levels of Fe_B^{3+} sites, respectively. The spectral intensity of the first excitation, $\text{Fe}_B^{2+} t_{2g} \rightarrow \text{Fe}_B^{3+} t_{2g}$, grows upon cooling, *i.e.*, upon increasing charge disproportionation, as expected. In contrast, the temperature dependence of the second excitation, $\text{Fe}_B^{2+} t_{2g} \rightarrow \text{Fe}_B^{3+} e_g$, goes in the opposite direction. The 1.9 eV feature decreases upon cooling as the hybridization of $\text{Fe}_B^{3+} e_g$ with O_{2p} orbitals gets enhanced by the charge ordering, thus increasing the occupation of minority spin \downarrow of the $\text{Fe}_B^{3+} e_g$ states.

In the literature, there is a discrepancy concerning the 1.9 eV feature found in reflectivity measurements [30, 119]. While in Park, Ishikawa and Tokura [30], the 1.9 eV feature is a prominent and well resolved one, in Gasparov et al. [119] it is essentially non-existent and not even mentioned. From the LSDA+U calculation, Leonov et al. [130] find that the contribution of the t_{2g} to e_g minority electron excitation has a minimal intensity, in disagreement with Park, Ishikawa and Tokura [30]. To amend the discrepancy between theory and experiment, they argue that using an averaged $P2/c$ structure for the low-temperature phase while neglecting dynamical correlations results in a small calculated intensity. When comparing theory [130], other optical spectroscopy data [132, 133], and our results, the existence of the 1.9 eV feature is unambiguous.

⁷Beyond the Drude peak in the metallic phase.

The data obtained via spectroscopy ellipsometry was subsequently used as a solid base for a non-equilibrium study⁸. Below T_V , the out-of-equilibrium spectra show three different regimes depending on the pump's fluence, demonstrating that the photoexcitation process can trigger an out-of-equilibrium response analogous to the Verwey phase transition. In the low-fluence regime, the observed response corresponds to the one associated with a warmer charge-ordered system. In the intermediate-fluence regime, nucleation of high-temperature phase with isolated patches of the low-temperature charge-ordered phase is observed. Finally, in the high-fluence regime, the system is instantly homogeneously driven into the high-temperature phase, and no nucleation process can be observed. Above T_V , the response as a function of fluence is linear, with no evidence of a photoinduced phase transition. ferromagnetic/

⁸The non-equilibrium part was measured and analyzed in Randi et al. [120].

6. Mott-Hubbard excitations in Ca_2RuO_4

Ruthenates of the family $\text{Ca}_{2-x}\text{Sr}_x\text{RuO}_4$ [136], a $4d$ electron system with nearly degenerate t_{2g} orbitals, are single-layered transition-metal oxides with a complex phase diagram. Moreover, this family is isostructural to the $\text{La}_{2-x}\text{Sr}_x\text{CuO}_4$ high-temperature superconducting cuprates. The rich physics they show, the potential role of the spin-orbit coupling, together with the structural similarity with the high-temperature cuprate-based superconductors, have given a strong research push to this $4d$ transition-metal oxide family of compounds.

On the $x = 2$ end of the family, Sr_2RuO_4 (SRO) with critical temperature of 1.35 K [137]. Although the superconducting phase transition temperature of SRO is considerably low, its relevance resides in the differences it presents compared to the cuprate-based superconductors. For example, in SRO, the superconducting phase exists only in undoped samples, whereas some doping is needed in cuprates. Moreover, the T_c shows no significant dependence on oxygen content [138], but it displays a strong dependence on non-magnetic impurities.

On the other end of the family, at $x = 0$, Ca_2RuO_4 (CRO) is a Mott insulator with a metal-insulator transition at about 357 K [139, 140]. The root of this transition has been the object of extensive studies [136, 137, 139, 141], for the most part agreeing that its origin lies in strong correlations and structural changes. Below 110 K the spins order antiferromagnetically at the level of the RuO_2 layer. By the application of small electric fields of the order of 40 V cm^{-1} or current Ca_2RuO_4 can undergo a insulator-to-metal transition into a conducting non-equilibrium phase [142–145]. Moreover, a close relationship between electrical, magnetic, and structural properties exists [136, 146–150].

In contrast with the cuprates, where just a single active electronic band plays a role, ruthenates, like most other transition-metal oxides, are multiband materials. Particularly evasive has been the understanding of the orbital degree of freedom in the ground state of Ca_2RuO_4 . Early experimental and theoretical work suggests an important role of the orbital degree of freedom [141, 151–156]. Thus, Ca_2RuO_4

provides an excellent opportunity to study the interplay between spin and orbital degrees of freedom.

In contrast to LCO, an effectively half-filled single 3d band electron system where the Mott transition arises due to a high U/W ratio, CRO presents a more complex situation. Because of the 2/3-filling of the t_{2g} level for $4d^4\text{Ru}^{4+}$, the Hund coupling becomes a relevant energy scale to consider [157], but it has been widely neglected.

Overall, the $\text{Ca}_{2-x}\text{Sr}_x\text{RuO}_4$ family shows multi-orbital Mott physics and superconductivity while having a strong spin-orbit coupling and therefore is of high current interest. Furthermore, recently, the interest in 4d electron systems has been focused on the role of the spin-orbit coupling in their physical properties.

For example, in layered t_{2g}^5 5d iridates [158], spin-orbit coupling presents a new type of Mott insulating state. It has also been proposed that doping the effective $j = 1/2$ Mott insulating state could lead to an exotic type of superconductivity [159], where Cooper pairs are composed of spin-orbit coupled electrons. This is also relevant in t_{2g}^5 $\alpha - \text{RuCl}_3$, highly debated as a proximate Kitaev spin-liquid [160]. In Ca_2RuO_4 , the central question concerns the ratio of the crystal field splitting (Δ_{CF}) to the spin-orbit coupling (2λ). This ratio affects directly, for example, the character of magnetic moments and of the magnetic excitations [161–170].

6.1. Physical Characterization

Similar to the layered cuprates, Ca_2RuO_4 is based on RuO_2 layers of corner-sharing RuO_6 octahedra, belonging to a distorted K_2NiF_4 structure [139]. Structural distortions are not uncommon in perovskite-related compounds. In most cases they arise due to a rotation and/or tilt of the octahedra as seen in similar compounds Sr_2IrO_4 [171, 172] and Sr_2RhO_4 [173]. The isostructural compound La_2CuO_4 also presents a similar distortion but with a smaller orthorhombic splitting. Figure 6.1 shows the crystal structure of the unit cell of Ca_2RuO_4 with in-plane O(1) and apical O(2) ions in red, the Ca ions are in light blue, and Ru^{4+} ions in grey. At room temperature its lattice constants are $a = 5.4097(3)\text{\AA}$, $b = 5.4924(4)\text{\AA}$, and $c = 11.9613(6)\text{\AA}$ in space group Pbca^1 [147, 174].

When compared to its Sr_2RuO_4 sibling, Ca_2RuO_4 naively may be expected to show metallic behavior due to the increased bandwidth arising from a shorter

¹In this space group, the octahedra combine a rotation around the c axis and a tilt around a parallel axis to an in-plane edge.

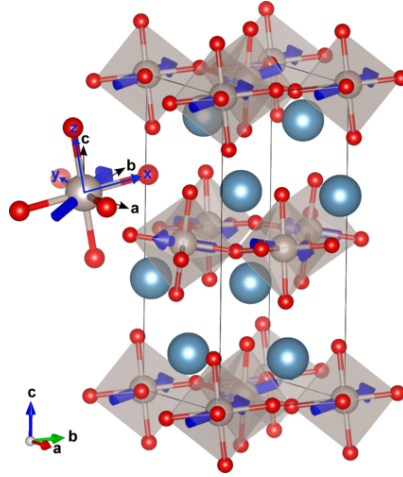


Figure 6.1.: Ca_2RuO_4 crystal structure in the low-temperature phase. The gray spheres denote the octahedral Ru^{4+} sites, the light blue spheres denote Ca, and the red ones denote O. The blue arrows on each Ru site show the magnetic moment on that site. In the inset, the local xyz frame around Ru_1 is shown. The RuO_6 octahedra show tilting, rotation, and a contraction along the local c axis. CC licensed from [175].

Ru-O distance. However, distortions from the K_2NiF_4 type structure lead instead to a substantial reduction in bandwidth, making Ca_2RuO_4 an insulator. Ca_2RuO_4 undergoes a first-order metal-insulator (MI) transition at about 357 K [140]. This MI phase transition is accompanied by a tetragonal to orthorhombic structural transition, as evidenced in the two leftmost panels in fig. 6.2. The orthorhombicity gets enhanced as the temperature is further reduced. Below $T_N \sim 110$ K, the spins order antiferromagnetically aligned parallel to the layers in the b direction which corresponds to the tilt axis [174, 176]. A finite Dzyaloshinsky-Moriya interaction originating from the crystal structure's low symmetry produces canting of the magnetic moments around the a direction. The rotation of the RuO_6 octahedra around the c axis (ϕ) is 11.8° showing no temperature dependence, while the tilt angle varies from 11.2° to 12.7° between room temperature and 11 K [147].

Above T_{MI} , the RuO_6 octahedra are elongated in the perpendicular direction to the RuO_2 layers. As the temperature is reduced and T_{MI} is crossed, the octahedra flattens as evidenced by the reduction of Ru-O(2) bond length shown in fig. 6.3. This flattening continues until close to the onset of the magnetic ordering temperature [147, 174].

Due to the substantial change in the lattice parameters at T_{MI} , in particular for the c axis, the crystals tend to crack and break while cooling down after growing.

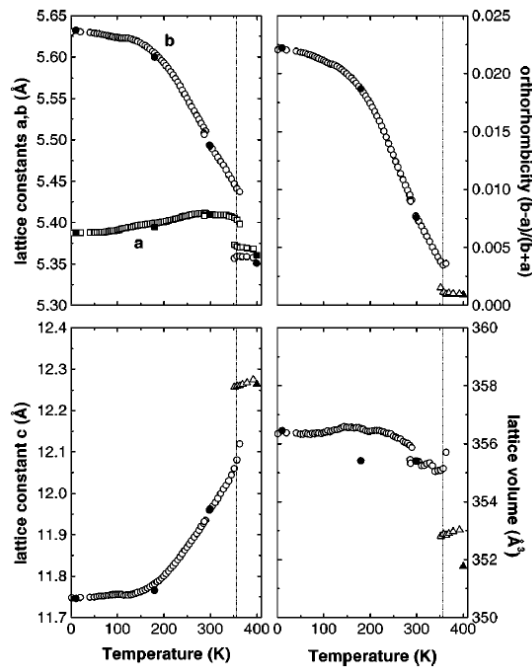


Figure 6.2.: Temperature dependence of the lattice parameters a , b , c (left panels). At $T_{MI} \sim 357$ K, Ca_2RuO_4 undergoes a tetragonal to orthorhombic structural transition. The orthorhombicity (top right) and unit cell volume (bottom right) increase as the temperature is reduced. Open and closed symbols correspond to high-flux and high-resolution experiments, respectively. The observed changes in the physical properties are evidence of the strong correlation between charge, spin, orbitals, and lattice degrees of freedom. Adapted from [147].

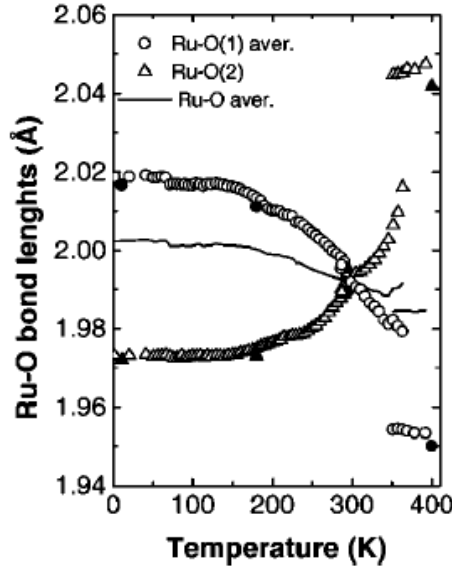


Figure 6.3: The RuO_6 octahedra octahedra flatten with decreasing temperature leading to a tetragonal distortion below 300 K. The flattening continues until the onset of the magnetic ordering. At about 300 K the octahedra show a cubic symmetry. Adapted from [147].

This renders the crystals unusable for many experiments, like inelastic neutron scattering. A minor substitution of 1% of Ti for Ru ameliorates this issue, allowing for bigger crystals to be obtained [164]. The introduction of the smaller Ti diminishes the amount of distortion in the structure, where at 10% substitution, the tilt and rotation angles are slightly reduced [163].

Physical characterization of $\text{Ca}_2\text{Ru}_x\text{Ti}_{1-x}\text{O}_4$ for $x = 0.01$ and $x = 0.1$ Ti substituted samples is shown in fig. 6.4. For the 1% substitution, resistivity measurements find a slight shift of the MIT temperature where it is slightly lowered by 4 K, while magnetization measurements find no change in its Néel temperature (T_N). At a substitution of 10%, the Néel temperature shifts to a lower temperature (107.2 K) while the MIT is destroyed, resulting in insulating behavior up to at least 700 K.

As discussed earlier, in Ca_2RuO_4 , there is a crossover from elongated to contracted octahedra happening close to room temperature upon cooling, see fig. 6.3. The introduction of Ti also affects the temperature where this crossover happens, placing it somewhere between 100 K and 300 K, as shown in fig. 6.5-a). Also, the distortion of the RuO_6 octahedra is suppressed by 10% Ti substitution as shown by the ratio of O-O bond lengths² on the edges of the RuO_6 octahedra parallel to a and b directions in fig. 6.5-b). The suppression of the distortions in the RuO_6 octahedra with the inclusion of 10% Ti^{+4} with an empty 3d shell supports the orbital ordering character of these distortions. However, Kunkemöller et al. [164]

²This ratio is related to the orthorhombic splitting $\epsilon = (b - a)/(a + b)$

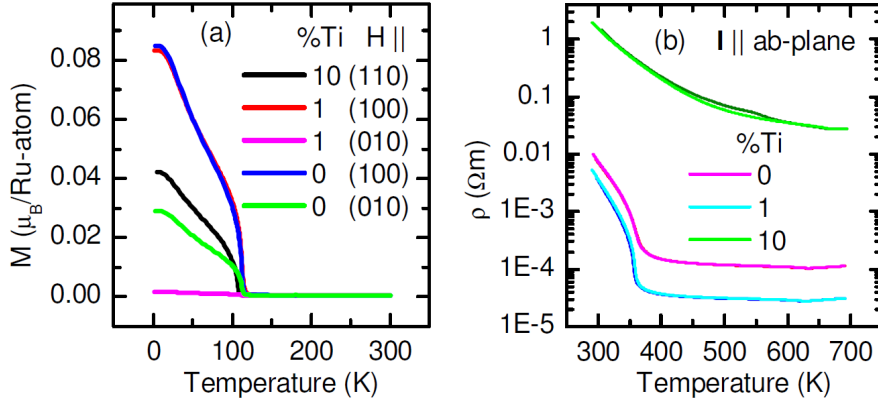


Figure 6.4.: Magnetization (left) and resistivity (right) as a function of temperature for different Ti content. The magnetic ordering temperature slightly shifts with increased Ti content while the MIT is completely suppressed for a 10% substitution. Adapted from [164].

observe that the average in-plane parameter increases while the c parameter decreases with increasing Ti substitution, a behavior that is the crucial element of the insulating state in Ca_2RuO_4 .

Regarding the electronic structure of Ca_2RuO_4 , the oxidation state of Ru is +4. When compared to the $3d$ transition metal oxides, the on-site Coulomb interaction is weaker due to the more extended nature of the $4d$ orbitals. This increased extension also leads to an enhanced t_{2g} - e_g crystal field splitting arising from a more considerable overlap of those $4d$ orbitals and the $2p$ ones from the ligand oxygen. Fatuzzo et al. [177] suggest a splitting of about 2 eV and 3 eV–4 eV for t_{2g} - $d_{3z^2-r^2}$ and t_{2g} - $d_{x^2-y^2}$, respectively. Hence the low-spin state $S = 1$ (t_{2g}^4) is favored instead of the high-spin one as in the case of the isoelectronic $3d$ LaMnO_3 .

6.1.1. Crystal-field splitting vs. spin-orbit coupling

At the core, the question resides on the precise character of the local electronic state of the four electrons within the t_{2g} shell. This local state depends on the non-cubic distortions splitting the t_{2g} level together with the spin-orbit coupling. The roles that the non-cubic distortions and the spin-orbit play, and their competition, has been discussed already for a long time. Thus we start our discussion by addressing first the effect of the crystal field while neglecting the spin-orbit coupling. Jung et al. [155], by using LDA+U calculations, suggest that in the low-temperature structure and AFM order, one electron occupies each one of the

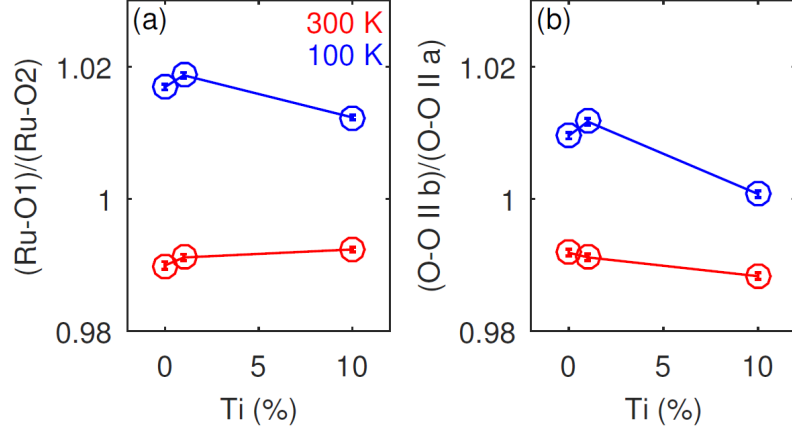


Figure 6.5.: a) Out-of-plane to in-plane Ru–O bond length ratio. b) Ratio of two O–O bond lengths. Adapted from [164].

three t_{2g} orbitals with majority spin and the remaining electron predominantly occupies the minority spin in the d_{xy} orbital resulting in ferro-orbital ordering, as depicted in fig. 6.6. LDA+DMFT results with and without spin-orbit coupling, Zhang and Pavarini [167] and Gorelov et al. [178], agree that in the insulating state, the orbital ordering is xy -like and when considering the AFM spin order the predominantly xy orbital order is maintained. Fang, Nagaosa and Terakura [156] identify three main factors responsible for the xy orbital stabilization. The first one is a geometrical factor due to the 2D nature of the crystal field and the subsequent energy-level splitting. The second factor relates to the Jahn-Teller compression along the c axis, which lowers the energy of the xy orbital. The third one is due to an orbital-dependent intersite hybridization between occupied and unoccupied orbitals pushing the yz/zx orbitals up. Now, due to the radial extension of the $4d$ orbitals, hybridization with the O $2p$ orbitals alters this situation. In another LDA+U study, Fang, Nagaosa and Terakura [156] find the orbital populations as $n_{xy}^{\uparrow} = 0.86$, $n_{yz/zx}^{\uparrow} = 0.87$, $n_{xy}^{\downarrow} = 0.79$, $n_{yz/zx}^{\downarrow} = 0.28$, where \uparrow (\downarrow) indicates majority (minority) spin.

As discussed in section 2.4, in $4d$ systems, the spin-orbit coupling can become relevant. Particularly for Ru the spin-orbit coupling is of the order of 0.1 eV. In heavy ions with t_{2g}^4 occupation (e.g., Re^{3+} , Ru^{4+} , Os^{4+} , and Ir^{5+}), under the strong spin-orbit coupling, in a local picture, the ground state should be a non-magnetic $j = 0$ singlet where the magnetism arises from virtual transitions to higher levels with finite j [162]. Such a ground state has been considered for Ca_2RuO_4 , reproducing the observed magnetic order while predicting some unusual magnetic features [161, 162]. An X-ray absorption study [152] agrees that spin-orbit coup-

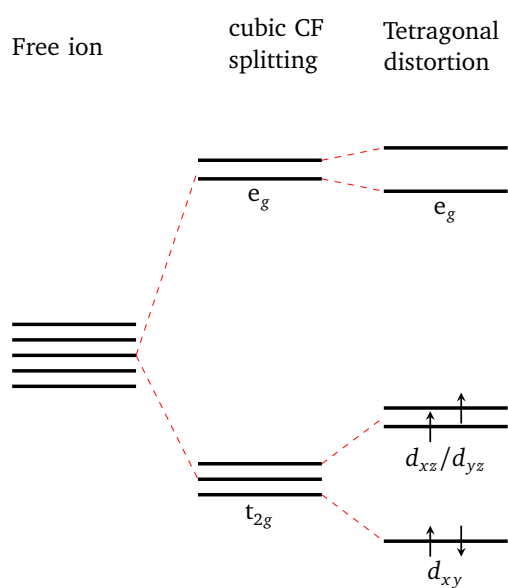


Figure 6.6.: The octahedral crystal field splits the $4d$ states in an upper e_g and a lower t_{2g} level. Due to the contraction of the octahedron along the c -axis, the tetragonal distortion lifts the degeneracy in the t_{2g} level, lowering the d_{xy} orbital. Naively, the four electrons in Ru^{4+} occupy the d_{xy} level with two electrons, and one in d_{xz} and another in d_{yz} . Theoretical and experimental studies refine this picture [152, 155, 156, 177] where it is found that the orbital occupation is temperature-dependent, as is also the structure (see fig. 6.2).

ling plays an important role suggesting a mixing of the t_{2g} orbitals leading to a partial occupation of each t_{2g} orbital. However, they argue that the SOC present in Ca_2RuO_4 is not strong enough to stabilize the $j = 0$ state. A similar x-ray absorption study [177] also supports this mixing of the t_{2g} orbitals due to the spin-orbit coupling. However, via inelastic neutron scattering (INS) Kunkemöller et al. [163] have shown that a conventional exchange Hamiltonian that considers the spin-orbit coupling through a single-site anisotropy term describes the observed dispersion, which features a sizeable in-plane spin gap of about 13 meV. This is further supported by the sign of the distortion (contraction) observed, indicating that the Jahn-Teller effect is stronger than the spin-orbit coupling.

In SRO and CRO, crystal-field splitting plus spin-orbit coupling has been necessary in describing the band structure. In an LDA+U+SO study [179], it has been suggested that the Mott insulating state present in CRO can be understood as being caused by a Coulomb-enhanced spin-orbit coupling. Recent LDA+DMFT calculations [167] that explicitly consider spin-orbit coupling and anisotropic Coulomb interaction find that the introduction of spin-orbit coupling does not lead to a $j = 0$ ground state and that the d_{xy} orbital order persists, and that the contraction of the c axis is the most critical factor driving the metal-insulator transition. Furthermore, the study reproduces the magnon dispersion found in Kunkemöller et al. [163]. Moreover, recent dynamical mean-field theory calculations on the Sr_2RuO_4 structure [180] find that the spin-orbit coupling does not affect much, supporting that they are Hund's metals.

6.2. Optics on Ca_2RuO_4

Moving onto optical spectroscopy, fig. 6.7 shows the Ca_2RuO_4 temperature-dependent optical conductivity obtained via Kramers-Kronig analysis of the reflectivity of the (a) in-plane ($E \parallel ab$) and (b) out-of-plane ($E \parallel c$) polarizations as reported by Jung et al. [155]. Both polarizations show a strong feature at about 3 eV that broadens as the temperature is increased. For $E \parallel c$, this feature is reminiscent of the one of Sr_2RuO_4 [181]. As such, this feature can be interpreted as the charge-transfer excitation from O $2p$ to Ru $4d$. The small difference in energy of this charge excitation peak between in-plane and out-of-plane stems from the different basal and apical O $2p$ energy levels due to the distortion of the RuO_6 octahedra.

The temperature dependence of the in-plane optical spectra (fig. 6.7 a)) shows a metallic feature above T_{MI} . In contrast, below T_{MI} , the insulating nature of

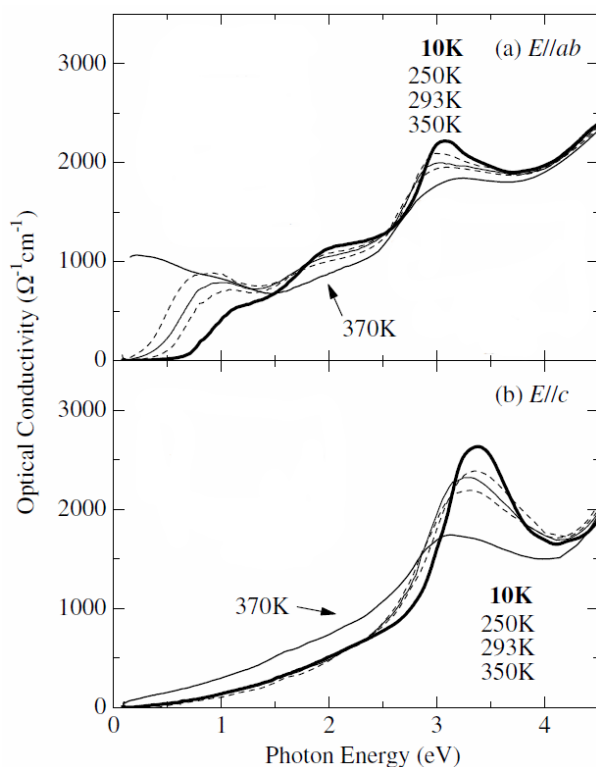


Figure 6.7.: Optical conductivity of Ca_2RuO_4 obtained via Kramers-Kronig analysis of broadband reflectivity measurement. a) In-plane ($E \parallel ab$): Two Mott excitation features below 2.5 eV and one charge-transfer excitation above 3 eV. The peak of the first feature shifts to lower energies as the temperature increases while also increasing its spectral weight. The second feature loses spectral weight as the temperature increases. b) Out-of-plane ($E \parallel c$): Charge-Transfer excitation without clear features below it, similar to the case of other layered oxides. Adapted from [155].

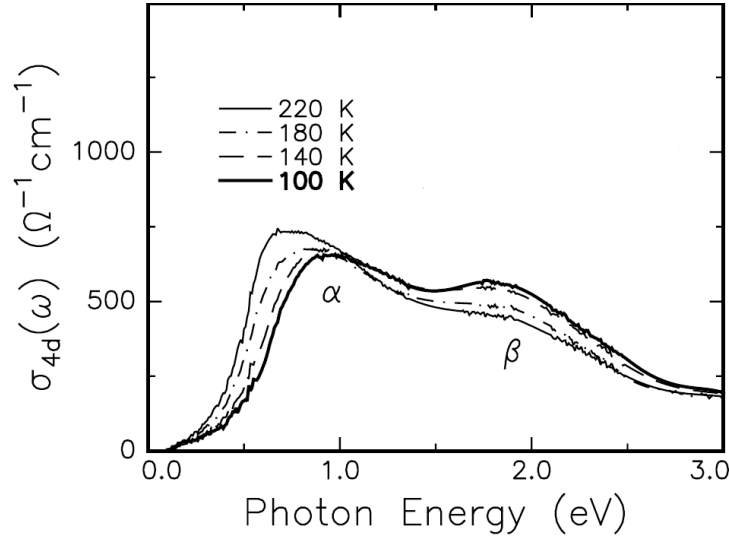


Figure 6.8.: Optical conductivity of $\text{Ca}_{2-x}\text{Sr}_x\text{RuO}_4$ for $x = 0.06$ obtained via Kramers-Kronig analysis of reflectivity measurement in the insulating state with the contributions of the phonons and charge-transfer excitations subtracted. The peaks at about 1 eV and 1.9 eV are labeled α and β , respectively. Adapted from [153].

this material with a gap below 1 eV is observed. The data seems to suggest a gap opening from about 250 K, which is much lower than the T_{MI} . Three principal features are observed at about 1.0 eV, 2.0 eV, and 3.2 eV. As the temperature decreases, the first feature's spectral weight diminishes while its energy shifts slightly to higher energies, whereas the spectral weight of the second feature increases.

Lee et al. [153] study the CSRO series from $x=2$ to $x=0$ via Kramers-Kronig analysis of the reflectivity measurements of the ab plane. For the $x = 0$ sample, they observe a strong peak at about 3.0 eV, which they assign to a charge-transfer excitation while assigning the features below 2.5 eV to Mott excitations, coinciding with the interpretation of Jung et al. [155]. The peaks at about 1 eV and 1.9 eV are labeled α and β , respectively. As a function of x , they observe that the peak at about 2 eV decreases in spectral weight and attribute this decrease to the reduction of U/W with increasing³ x . The nearest neighbor spin correlation below the Néel temperature (T_N) is, for the most part, antiferromagnetic (AFM). Following a simple representation of the electronic configuration based on a 3-orbital Hubbard model (see fig. 6.9), Lee et al. [153] expect excitations only arising from

³With decreasing x , the distortions increase, making the bandwidth (W) narrower.

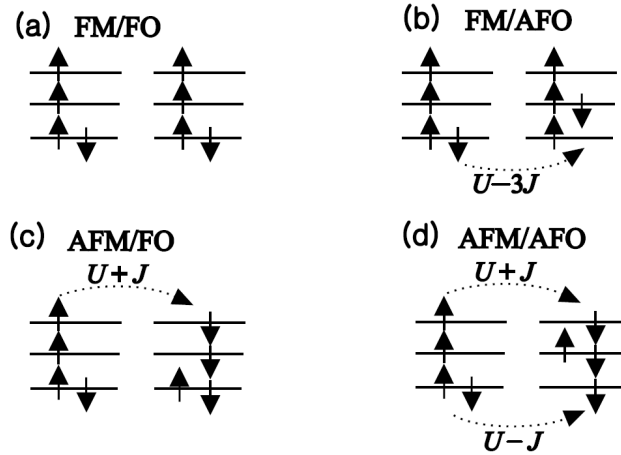


Figure 6.9.: Possible spin/orbit configurations for fully degenerate t_{2g} orbitals in a $4d$ system with two sites in a 3-orbital Hubbard model. The interaction energies involved are the Coulomb on-site U for electrons occupying the same orbital, U' for electrons in different orbitals but with opposite spin, and U'' for electrons in different orbitals and same spin. Considering the orbital rotational symmetry of the system, a simplification is obtained as $U' = U - 2J$, and $U'' = U - 3J$, where J is the Hund's exchange interaction between two electrons in the t_{2g} orbitals [182]. a) ferromagnetic/ferro-orbital (FM/FO), b) ferromagnetic/antiferro-orbital (FM/AFO), c) antiferromagnetic/ferro-orbital (AFM/FO), and d) antiferromagnetic/antiferro-orbital (AFM/AFO). In panel a) no transition can take place due to Pauli's exclusion principle. In panels b) to d) the possible excitations are indicated with dotted arrows plus with the energy involved. Only for panel d) two transitions are allowed with energies $U - J$ and $U + J$, leading to an experimental value of $2J$ of about 1.0 eV. Adapted from [153].

spin/orbital configurations of the type AFM paired with antiferro-orbital ordering since it is the only spin/orbital configuration where two optical transitions are allowed. However, this sketch does not describe the physics of the system correctly as it neglects rotation and tilts of the octahedra which enable other excitations.

Lee et al. [153] also report the temperature dependence, where they report that "... exist systematic spectral changes between peaks α and β even in the insulating state.". They find that the spectral weight of the first peak decreases with decreasing temperature. In contrast, the spectral weight for the second peak increases with decreasing temperature. Thus, Lee et al. [153] argue that given the temperature dependence of both features (see in fig. 6.10), that the relevance of ferro-orbital (FO) correlation increases with decreasing temperature.

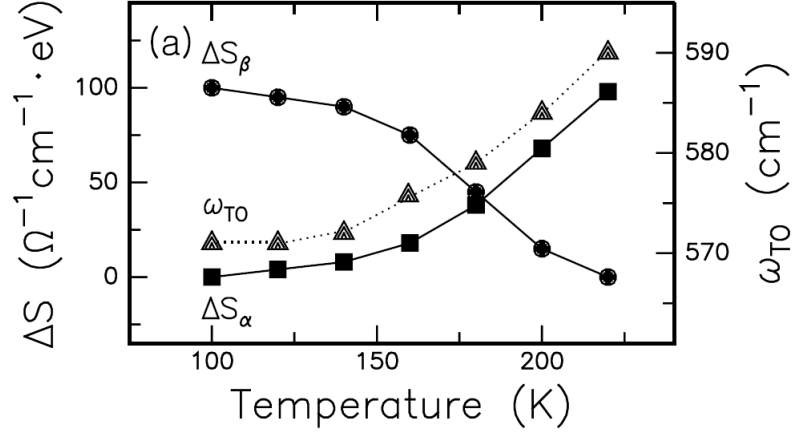


Figure 6.10.: Temperature dependence of the difference in spectral weight for peaks α and β ($\Delta S_\alpha(T) = S_\alpha(T) - S_\alpha(T = 100\text{K})$ and $\Delta S_\beta(T) = S_\beta(T) - S_\beta(T = 220\text{K})$). Reproduced from [153].

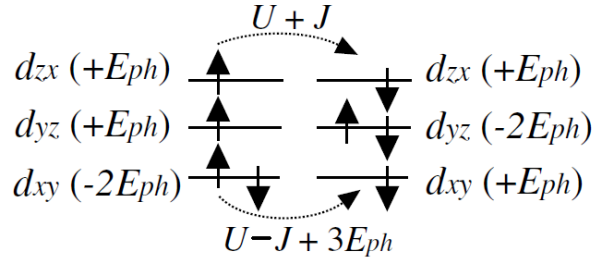


Figure 6.11.: Schematic of the energy level for the antiferromagnetic/antiferro-orbital ordered state with doubly occupied d_{xy} and d_{yz} orbitals and Jahn-Teller-like distortions of the octahedra which gives rise to a $U - J + 3E_{ph}$ excitation. Adapted from [153].

Furthermore, they also observe a shift of about 0.24 eV of the α peak between 100 K to 250 K, whereas the β peak shows no significant shift. To explain this shift in one of the peaks, they argue that it has to do with electron-phonon coupling arising from a Jahn-Teller distortion that lifts the degeneracy of the t_{2g} orbitals changing their energies by $-2E_{ph}$ and E_{ph} for double and single occupancy, respectively, adding an energy cost of $3E_{ph}$ to the lowest excitation in the AFM/AFO configuration as schematically shown in fig. 6.11. Taking $E_{ph} \approx \omega_{\text{TO}} \approx 600 \text{ cm}^{-1}$, the shift of the peak is about 0.22 eV which they claim it agrees with the observed shift of 0.24 eV.

Comparisons of the experimental optical conductivity with the one obtained through LDA+U [155] and LSDA+U [156] show, in both cases, a good agree-

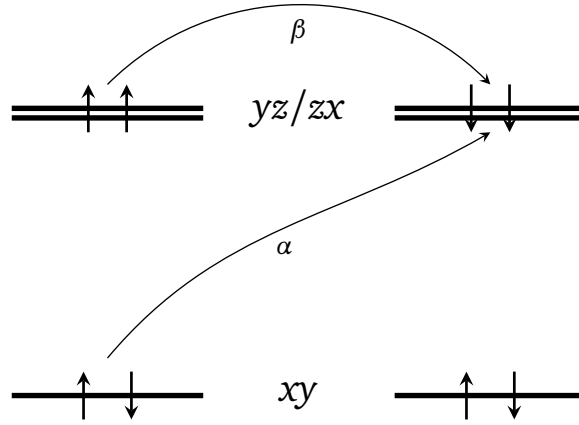


Figure 6.12.: Single particle picture of the low-energy excitations in Ca_2RuO_4 as suggested for the interpretations of optical data and complementary LDA+U and LSDA+U calculations [155, 156]. Note the antiferro alignment of the magnetic moments on adjacent sites.

ment. Based on the calculated density of states, Jung et al. [155] attribute the origin of each feature in the optical conductivity as follows: the first two features at about 1.0 eV and 2.0 eV come primarily from excitations between lower and upper Hubbard bands of the Ru $4d$ electrons. The first feature (α) is a $d_{xy,i} \rightarrow d_{xz/yz,j}$ excitation, whereas the second feature (β) is a transition from an occupied majority spin on site i to an unoccupied d_{xz}/d_{yz} orbital on site j , as shown in fig. 6.12. Above 3.0 eV, charge-transfer excitations from occupied O $2p$ to unoccupied Ru t_{2g} states are located. By comparing the spectra calculated for the 11 K AFM and the 295 K FM states, the changes in the first peak are related to the increased d_{xy} hole population and the decrease of the Jahn-Teller splitting, whereas for the second peak, they are related to the change of the relative orientation between the moments on neighboring sites, comparing the ferromagnetic and antiferromagnetic states.

6.3. Results

As mentioned earlier, since significant lattice changes accompany the metal to insulator transition in Ca_2RuO_4 , the crystal tends to break apart into small pieces not suitable for many experiments. A 1% Ti doping stabilizes the sample during cooling after the growing process [163]. Besides the 1% Ti substituted Ca_2RuO_4 , a second sample with a 10% Ti substitution was also investigated.

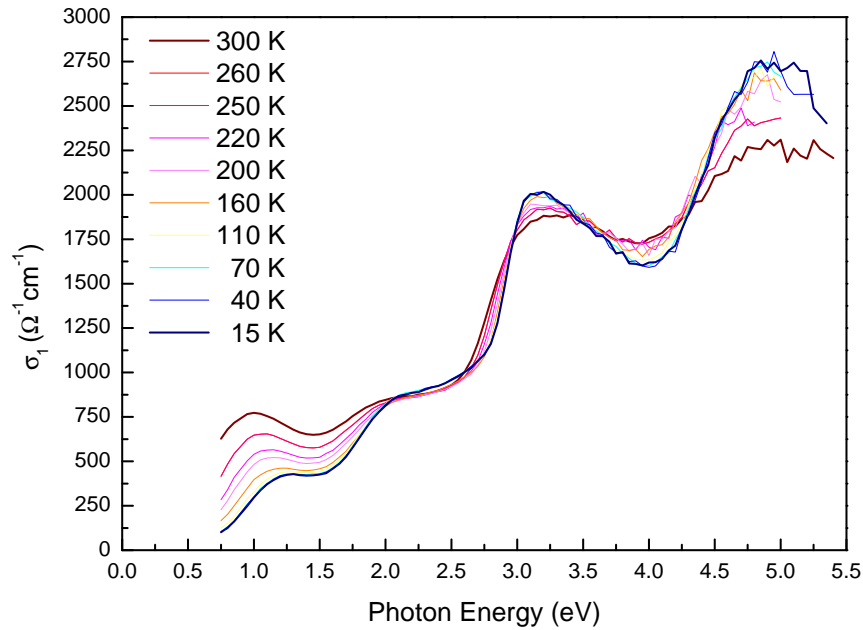


Figure 6.13.: Temperature-dependent in-plane optical conductivity of the 1% Ti substituted Ca_2RuO_4 calculated from the psuedo dielectric function.

6.3.1. 1% Ti doped

The temperature-dependent optical spectra of Ca_2RuO_4 with 1% Ti are shown in fig. 6.13. The measurement has considerable noise at high energy due to the lower light intensity from the source and the small sample size. We can observe four clear features at about 1.2 eV, 2.0 eV, 3.2 eV, and 4.9 eV. The data at 15 K exhibit good qualitative agreement with those measured by Jung et al. [155] shown in fig. 6.7. Here, we observe how the feature at about 1 eV shifts towards lower energies with an increase in spectral weight as the temperature is increased. The feature at about 2 eV also shows a slight shift towards lower energies plus a notorious broadening. For the 3.2 eV feature, we observe that it broadens without showing signs of much shift in energy, leading to a reduction of the optical conductivity at the peak. The highest energy feature at about 5.0 eV shows a similar behavior as the previous one, but with a more substantial reduction of the optical conductivity value as a function of temperature. Overall, qualitatively, the measured optical spectra's temperature dependence agrees with the previously reported data by Jung et al. [155].

6.3.2. 10% Ti doped

The temperature-dependent optical spectra are shown in fig. 6.14. Below 2.7 eV, the optical conductivity shows a very similar structure compared to the measurement of the 1% doped sample shown in fig. 6.13 displaying two features at about 1 eV and 2 eV. The lowest energy feature shows mostly the same behavior as in the 1% Ti substituted sample, the peak shifting to lower energies. The second feature shows a more pronounced change as a function of temperature than in the 1% substituted sample, keeping the energy mostly fixed and primarily showing a broadening and a monotonous reduction of the optical conductivity at the peak.

At high energies, there is a substantial reduction of the optical conductivity as a function of temperature. The peak found at 3.2 eV in the undoped sample is now much sharper and at lower energy than the equivalent one in the undoped sample, while the higher feature, at about 4.5 eV, is very much broadened and lower in energy. The high-energy features show an evident broadening with an increase of the optical conductivity's peak value as the temperature increases until about 310 K. There is a sudden drop in the optical conductivity in the high-energy region of the measured spectra at higher temperatures.

6.4. Analysis

To get further insight into the optical spectra as a function of temperature of both samples, particularly for the low-energy features, we built an optical model for each one of them. The optical model includes a surface roughness layer. Since the sample does not have a transparent region in the measured spectra which was set at 4 nm as a value representative of what we have encountered previously in modeling similar materials.

6.4.1. 1% Ti doped

The optical model for the 1% Ti sample consists of six oscillators in total. Four Gaussian oscillators with two of them below 2.1 eV and the other two above 4.5 eV, and two Tauc-Lorentz in between both groups of Gaussians. The full set of fitted parameters is shown in table 6.1 for the 15 K measurement. Besides the oscillator parameters, the magnitudes of a low- and a high-energy pole plus ϵ_∞

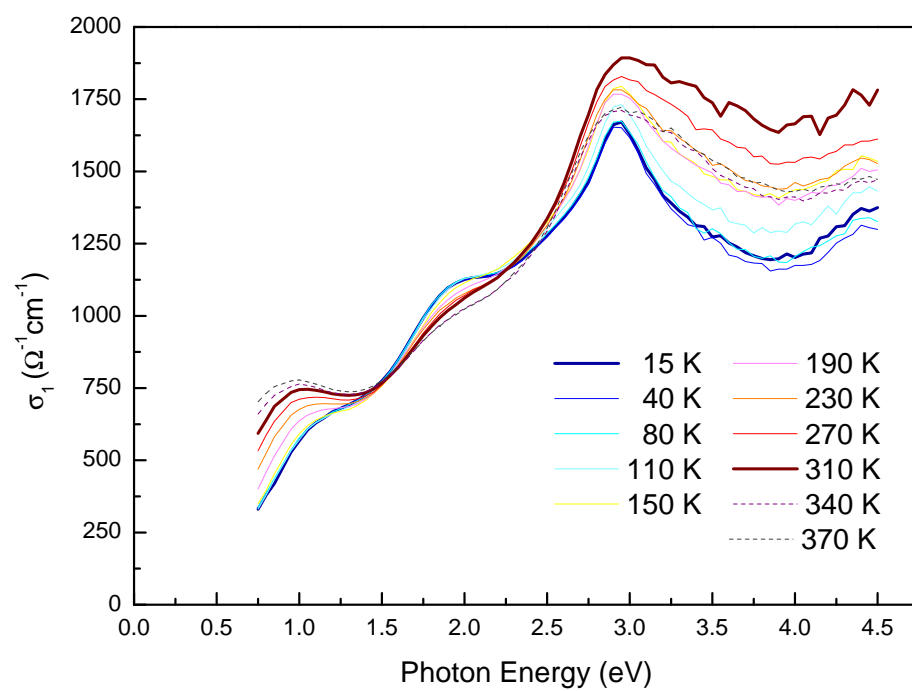


Figure 6.14.: Temperature dependent in-plane optical conductivity of 10% Ti substituted Ca_2RuO_4 from the pseudo dielectric function. Above 310K, the high-energy data suffer a significant drop. Thick lines correspond to 15 K and 310 K.

Chapter 6: Mott-Hubbard excitations in Ca_2RuO_4

Oscillator #	Energy (eV)	Amplitude (eV)	Width (eV)	Gap (eV)
1	1.13	2.33	0.65	-
2	2.06	3.05	0.91	-
3	2.64	63.06	1.58	2.07
4	2.92	99.53	0.42	2.74
5	4.59	1.12	0.63	-
6	5.15	2.24	0.96	-

Table 6.1.: Set of oscillators and their fit parameters used in the optical model for Ca_2RuO_4 with % doping at 15 K. The entries with a value in the gap column correspond to Tauc-Lorentz oscillators.

were set as parameters to be fitted. The positions of the poles were fixed⁴ at 0.1 eV and 6.7 eV, respectively, for all temperatures.

The two oscillators below 2.5 eV are the ones we will focus on through the analysis, located at 1.13 eV and 2.06 eV at 15 K, respectively. Figure 6.15 shows, as a function of temperature, the energy, amplitude, width, and the normalized spectral weight at 15 K of both oscillators. The energy of both Gaussian oscillators (fig. 6.15 a)) shows a shift to lower energies as temperature increases, where the lowest energy oscillator shows the largest shift. More change happens in the fitted amplitude (fig. 6.15 b)), particularly for the first oscillator, which shows an almost 140% increase between 15 K and 300 K. The width (fig. 6.15 c)) for both of the oscillators increases with increasing temperature, more noticeable for the second one where there is an increase of 50%. In summary, the first oscillator increases considerably in amplitude while the second oscillator primarily broadens as a function of temperature.

Ultimately, the physical behavior of the oscillators is encoded in the spectral weight (fig. 6.15 d)), which is shown normalized by its value at 15 K. We can observe an increase in the spectral weight as a function of temperature for both oscillators. For the first oscillator, most of the increase in spectral weight comes from the increase in its amplitude, whereas for the second oscillator the increase is closely related its broadening. Interestingly, there is no noticeable change across the Néel temperature of the sample.

In the previous analysis, there is an issue. Ca_2RuO_4 is not a cubic sample, this

⁴We kept them fixed since the position and magnitude of a pole are highly correlated while making the fit numerically better due to an extra parameter.

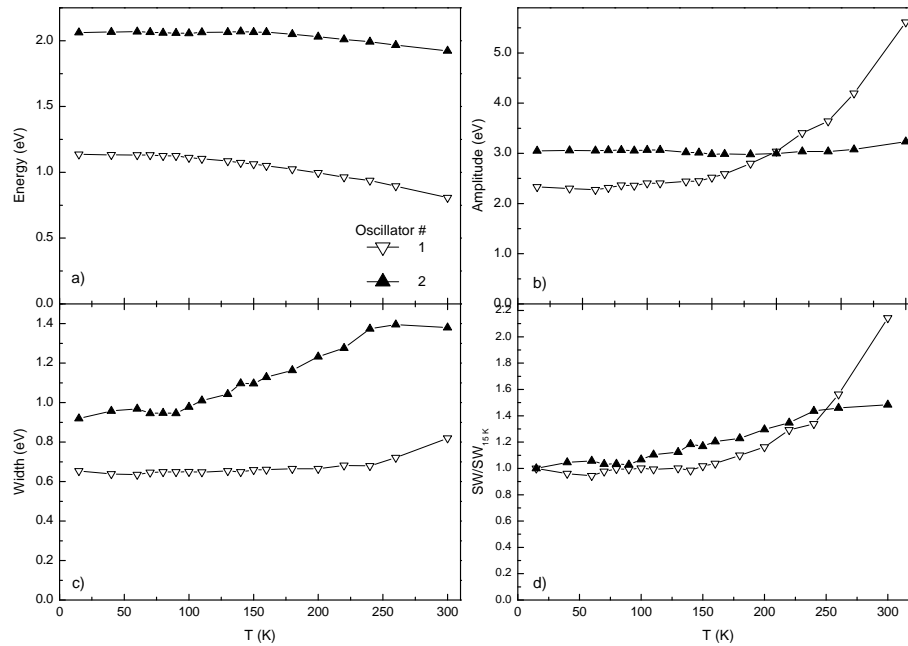


Figure 6.15.: Fitted parameters (a) - c)) and normalized spectral weight (d)) as a function of temperature of the first two oscillators used in the optical model for the 1% Ti substituted Ca_2RuO_4 .

Osc. #	Temperature (K)	Energy (eV)	Amplitude (eV)	Width (eV)
1	15	1.14	2.33	0.65
	300	0.81	5.61	0.82
2	15	2.06	3.05	0.92
	300	1.92	3.23	1.38

Table 6.2.: Fit parameters of the two lowest energy Gaussian oscillators for 15 K and 300 K for 1% Ti substituted Ca_2RuO_4

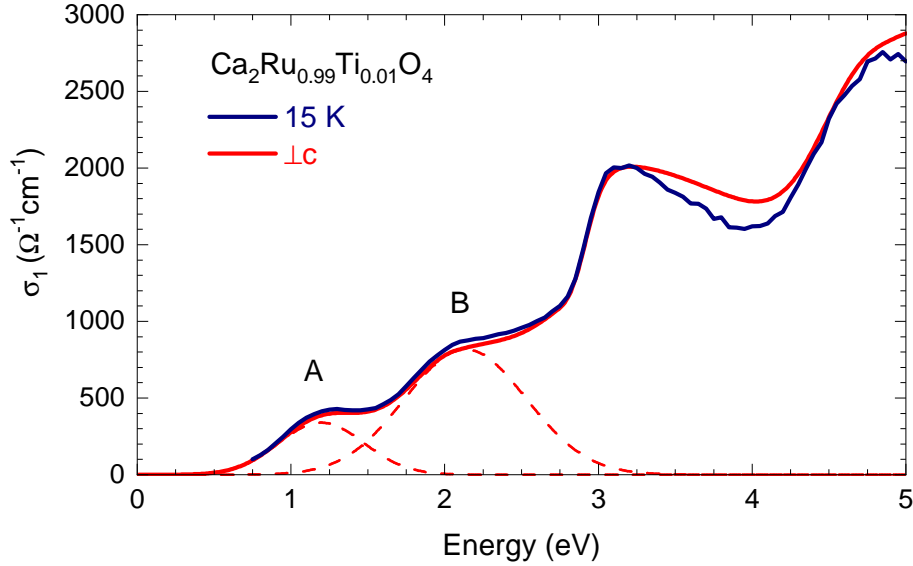


Figure 6.16.: Comparison of the pseudo-dielectric point-by-point (blue) to the uniaxial model (red) results of the optical conductivity at 15K for the 1% Ti doped Ca_2RuO_4 . For the uniaxial model, the c -axis data from Jung et al. [155] is employed to be able to account for effects stemming from the anisotropy of the sample.

means that eq. (3.26) is not strictly correct as it assumes an isotropic sample. In this case, multiple orientations should be measured and modeled considering the anisotropic nature of the sample. Unfortunately, the available samples did not allow the measurement of the optical spectra along the c axis. However, the pseudo-dielectric function serves us well in our purpose of analyzing the Mott-Hubbard excitations which do not contribute to the c -axis response. The agreement between our experimental data as analyzed with eq. (3.26) and the data from reflectivity-based measurements [153, 155] serves as extra support. Furthermore, to further validate the decision to use the pseudo-dielectric function we used a second model where we analyzed our measured data together with the c -axis data from Jung et al. [155] to be able to explicitly take into consideration the anisotropy of the sample. As seen in fig. 6.16, this new model (red) produces a very similar fit to the one ignoring anisotropic effects (blue), particularly for both Mott-Hubbard peaks of interest. For the relevant measure we are interested in, namely the ratio of their spectral weight, we find that the anisotropy-based model produces a value of 0.29 in agreement with what we already calculated.

6.4.2. 10% Ti doped

For the 10% doped sample, the optical model used to fit the observed data consist of four Gaussian oscillators, two Tauc-Lorentz ones, together with the amplitudes of two poles located at 0.1 eV and 6.7 eV, respectively. The value of ϵ_{∞} was kept fixed at 1 because otherwise, it did fit to values lower than 1, which is a nonphysical result.

Analogous to the 1% Ti doped sample, we will focus on the two lowest-energy oscillators, as shown in fig. 6.17. Concerning the high-energy oscillators, since the optical spectra show broad and incomplete features, the uncertainty of the fit parameters is relatively high. Thus, they have to be taken with caution. This will not be a big issue since we are primarily interested and will be focusing on the low-energy features, which are well defined.

The energies (fig. 6.17 a)) of the first three oscillators at 15 K are 0.98 eV, 1.83 eV, and 2.5 eV, respectively, see table 6.3. Similar to the 1% doped sample, the energy of the two lowest oscillators show changes as a function of temperature, where the first one shifts monotonously to lower energies. The second one slightly shifts down, reaching a minimum at about 200 K, to then increase again.

The amplitude (fig. 6.17 b)) increases as a function of temperature for both oscillators. Particularly interesting is that the oscillator centered at 0.9 eV at 15 K shows the increase mainly starting at about 110 K, while the second oscillator seems to reach a saturation value at that temperature. As for the width of the oscillators (fig. 6.17 c)), both oscillators have opposite tendencies becoming narrower and broader, for the first and second oscillators, respectively. At last, the spectral weight (fig. 6.17 d)) shows an interesting trend as a function of temperature. Whereas the first oscillator shows a rather constant value, the second oscillator shows a steady increase from about 110 K, reaching a plateau above 300 K following the amplitude and width behavior.

With increasing Ti content, we expect to lose spectral weight as there are fewer electrons available. We can observe this at the high energy part of the spectra but not at low energy. The Ti ions may be affecting the Ru–O energy in their neighborhood, which could shift the weight of the charge-transfer excitations to lower energies.

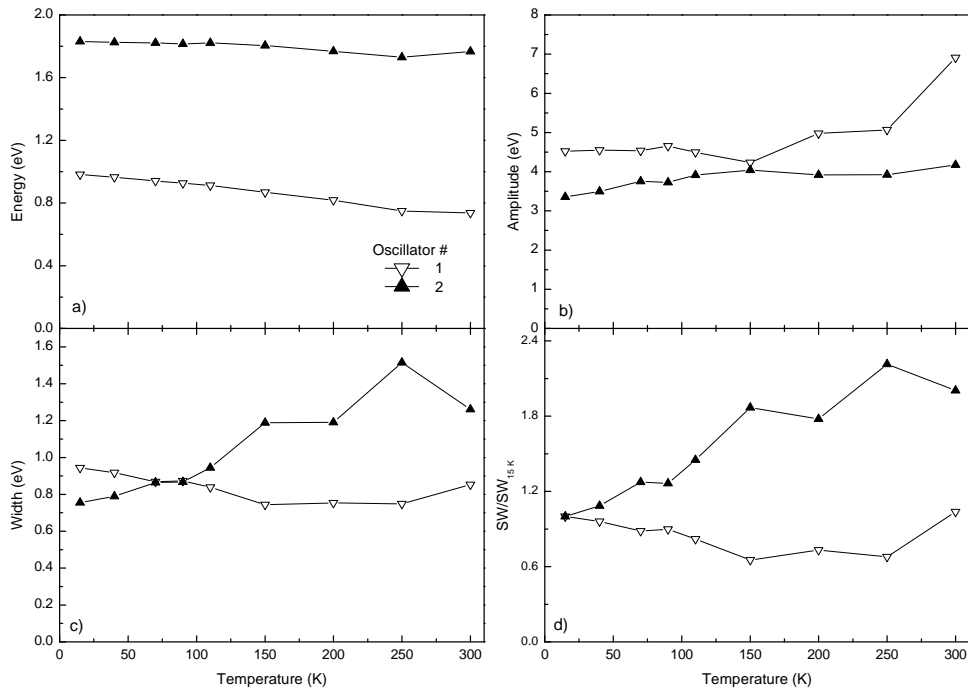


Figure 6.17.: Fitted parameters (a - c)) and normalized spectral weight (d)) as a function of temperature of the first two oscillators used in the optical model for the 10% Ti substituted Ca_2RuO_4 .

Oscillator #	Energy (eV)	Amplitude (eV)	Width (eV)	Gap (eV)
1	0.98	4.52	0.94	-
2	1.83	3.36	0.76	-
3	2.5	2.49	0.76	-
4	2.89	2.98	0.47	1.54
5	3.28	3.7	1.06	1.13
6	4.45	1.20	1.52	-

Table 6.3.: Fit parameters for the 10% Ti substituted Ca_2RuO_4 at 15 K. The entries with a value in the gap column correspond to Tauc-Lorentz oscillators.

Osc. #	Temperature (K)	Energy (eV)	Amplitude (eV)	Width (eV)
1	15	0.98	4.52	0.94
	300	0.74	6.91	0.85
2	15	1.83	3.36	0.76
	300	1.77	4.17	1.26

Table 6.4.: Summary of the first two oscillators for the 10% Ti substituted Ca_2RuO_4 at 15 K and 300 K.

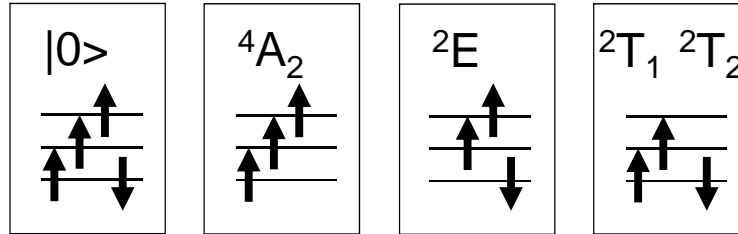


Figure 6.18.: Sketch of the t_{2g}^4 ground-state multiplet as well as of the different t_{2g}^3 multiplets available. The nomenclature refers to the idealized case of a cubic crystal field. From [135].

6.4.3. Peak assignment

Focusing on the two lowest energy features for the 1% doped sample observed at about 1 eV and 2 eV, we concur in the assignment of them to Mott-Hubbard excitations between neighboring Ru sites i and j ($|4d_i^4 4d_j^4\rangle \rightarrow |4d_i^3 4d_j^5\rangle$) as previously done [153, 155]. As discussed previously, given the large cubic crystal field, the 4 available electrons occupy the t_{2g} shell in the ground state. Furthermore, this large crystal field allows us to neglect the e_g orbitals when discussing the lowest excitations. As with previous reports [153, 155], strong charge-transfer excitations of the type $|\text{Ru } 4d^4, \text{O } 2p^6\rangle \rightarrow |\text{Ru } 4d^5, \text{O } 2p^5\rangle$ set in at about 3 eV (see fig. 6.7).

We analyze the local multiplet scenario for a t_{2g}^4 electronic configuration in the idealized case of a cubic crystal field and without spin-orbit coupling. In this scenario, the energy difference between excitations across the Mott gap originates only from the multiplets within the t_{2g}^3 sector because all six t_{2g}^5 configurations have the same energy forming a 2T_2 multiplet. The t_{2g}^3 sector has $6 \cdot 5 \cdot 4/6 = 20$ states, being classified into the multiplets 4A_2 , 2E , 2T_1 , and 2T_2 which are shown in fig. 6.18 in a simple single particle picture. Thus, the energies of the possible

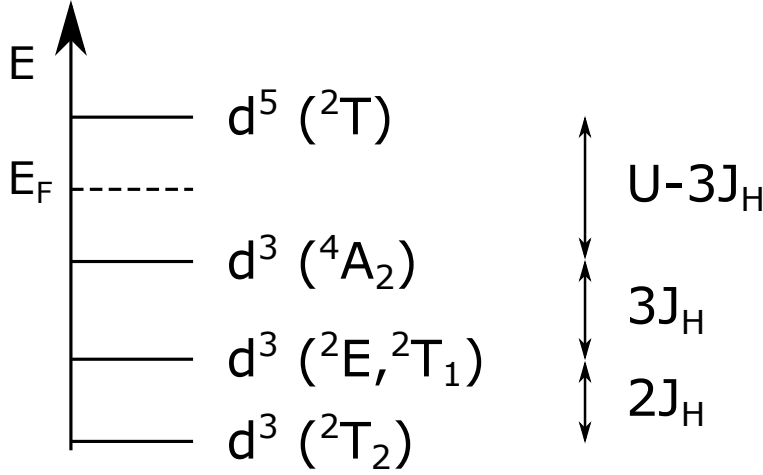


Figure 6.19.: Local picture of the energy levels of the d^3 and d^5 excited states of a t_{2g}^4 system.

Mott-Hubbard excitations are given by

$$\Delta E = E(5) + E(3) - 2E(4) \quad (6.1)$$

which leads to $U - 3J_H$ for 4A_2 , U for 2E , 2T_1 , and $U + 2J_H$ for 2T_2 , where U and J_H are the on-site Coulomb repulsion and the Hund coupling, respectively (see fig. 6.19). LDA+DMFT calculations performed by Zhang and Pavarini [167] show a good agreement with experimental results when using either $U = 2.3\text{eV}$ and $J_H = 0.4\text{eV}$, or $U = 3.1\text{eV}$ and $J_H = 0.7\text{eV}$ as parameters. Thus, in a local picture, this set of parameter values describes the observed energies of the first two peaks well.

The multiplets arising from a cubic scenario are a good starting point to estimate the energies involved. However, to make a reasonable comparison with experimental results, additional effects like a tetragonal crystal-field splitting Δ_{CF} , spin-orbit coupling λ , and band-structure effects have to be eventually considered.

When the spin-orbit coupling $\lambda \approx 0.1\text{eV}$ [167] is compared to the other parameters, it is rather small and thus can be neglected for the peak assignment. Note that the crystal-field splitting is the only parameter that can be expected to have a pronounced temperature dependence arising from the temperature-induced change in the crystal structure as described previously. First-principles calculations presented by Zhang and Pavarini [167] display a temperature-induced shift of Δ_{CF} of about 0.2eV between the insulating phase at 180K ($\Delta_{\text{CF}} = 0.3\text{eV}$) and the metallic phase at 400K ($\Delta_{\text{CF}} = 0.1\text{eV}$). Resonant inelastic x-ray scat-

tering experiments [183] estimate that for Ca_2RuO_4 at 15 K the parameters are $\Delta_{\text{CF}} = 0.25$ eV, $\lambda = 0.13$ eV, and $J_H = 0.34$ eV. When we calculate the shift of the energy of the lowest oscillator used in the modeling (table 6.2) between the highest (300 K) and lowest (15 K) temperatures, we obtain the value of 0.31 eV.

In principle, there are four possible d^3 multiplets that should give rise to three different excitation energies, but with optical spectroscopy, only two of them are observed. ARPES measurements [184] on Ca_2RuO_4 in its insulating phase at 150 K show two rather flat Ru bands, called A and B, respectively. These two flat bands give rise to two peaks in the energy-distribution curves, located at 0.8 eV and 1.7 eV below the Fermi level⁵. The data also shows a third low-energy band, called C, with a larger dispersion that is shifted by about 1.2 eV with respect to the lowest band and by 0.3 eV with respect to the second one. The split observed between the A and B bands, by about 0.9 eV, agrees well with the splitting of the features in our optical data (table 6.2). A comparison with LDA+DMFT calculations leads to the assignment of peak A to the 4A_2 multiplet and peak B to the 2T_1 multiplet, namely removing an electron from the d_{xz} or d_{yz} orbitals. Above, we discussed the energies of possible multiplets in a local picture leading to an energy splitting between the 2T_1 and 2T_2 multiplets to the 4A_2 one of $3J_H - \Delta_{\text{CF}}$ and $5J_H - \Delta_{\text{CF}}$, respectively. This suggests that peak B should be assigned to the 2T_1 multiplet and to argue that the 2T_2 one might be hidden under the stronger charge-transfer excitations.

The larger dispersion of the C band suggests an xy character since, due to the layered nature of Ca_2RuO_4 , the xy bandwidth should be about twice as large as the xz or yz bandwidth. Thus, this broad band can be assigned to the 2E multiplet, and then the energy shift between the lowest 4A_2 band and this one is 1.2 eV = $3J_H$ allowing an estimation of $J_H = 0.4$ eV [184]. The splitting observed in ARPES, between the B (2T_1) and the C (2E) bands is 0.3 eV, which can be associated with Δ_{CF} which is in line with previous estimations and our data, where we estimate $\Delta_{\text{CF}@15\text{K}} = 0.3$ eV and $\Delta_{\text{CF}@300\text{K}} = 0.1$ eV. The results obtained by ARPES map directly to optical spectroscopy, the flat dispersion of the bands A and B gives rise to clear peaks in the optical conductivity. In contrast, the large dispersion of band C explains the absence of a well-resolved peak in the optical conductivity.

To summarize, the peak assignment we describe agrees with the results of Jung et al. [155], which uses optical spectroscopy and a LDA+U study while neglecting spin-orbit coupling. On the other hand, the assignment reported by Lee et al. [153], where they neglect rotation and tilt of the octahedra leading to

⁵The ARPES experimental technique measures the electron removal states, *i.e.*, the d^3 sector, which in this case dominates the multiplet splitting in Ca_2RuO_4 .

vanishing matrix elements for peak A, is different.

6.4.4. Transition matrix elements

To further interpret the measured spectra, we calculate the transition matrix elements of the excitations involved and then the ratio of the intensities between low- and high-temperature states to estimate the change in spectral weight. For such calculation, one has to sum over all bonds available. In our case, it means to sum all the excitations from a single site to its four neighbors in the ab plane. The hopping matrix elements might differ among the bonds when tilts and rotations of the participating octahedra are involved, but to make this simpler, we will assume that the four bonds on the ab plane are the same. This is motivated by the absence of any difference between polarizations parallel to a or b in our optical data.

Neglecting spin-orbit coupling, the ground state of Ca_2RuO_4 can be approximated in the conventional xy orbital order by the d^4 states given by

$$|d^4 \uparrow\rangle = c_{yz\uparrow}^\dagger c_{xz\uparrow}^\dagger c_{xy\uparrow}^\dagger c_{xy\downarrow}^\dagger |0\rangle \quad (6.2a)$$

$$|d^4 \downarrow\rangle = c_{yz\downarrow}^\dagger c_{xz\downarrow}^\dagger c_{xy\uparrow}^\dagger c_{xy\downarrow}^\dagger |0\rangle \quad (6.2b)$$

for the $S_z = \pm 1$ components and

$$|d^4, S_z = 0\rangle = \frac{1}{\sqrt{2}} \left(c_{yz\uparrow}^\dagger c_{xz\downarrow}^\dagger + c_{yz\downarrow}^\dagger c_{xz\uparrow}^\dagger \right) c_{xy\uparrow}^\dagger c_{xy\downarrow}^\dagger |0\rangle \quad (6.3)$$

for the $S_z = 0$ one. Here, $|0\rangle$ is the state with no electrons, and where $c_{\alpha\sigma}^\dagger$ and $c_{\alpha\sigma}$ are the annihilation and creation operators for an electron in orbital α with spin σ . Notice that here we are omitting the site indexing label. The $S_z = 0$ component describes, at 0 K, a magnetic excitation (magnon). For the calculation of the transition matrix elements, this magnon can be neglected in the low-temperature phase but not in the high-temperature disordered phase.

Now, we discuss the possible d^5 and d^3 excited states. For the d^5 state, we have the following possible configurations,

$$|d^5, yz \uparrow\rangle = c_{yz\uparrow}^\dagger c_{xz\uparrow}^\dagger c_{xz\downarrow}^\dagger c_{xy\uparrow}^\dagger c_{xy\downarrow}^\dagger |0\rangle \quad (6.4a)$$

$$|d^5, yz \downarrow\rangle = c_{yz\downarrow}^\dagger c_{xz\uparrow}^\dagger c_{xz\downarrow}^\dagger c_{xy\uparrow}^\dagger c_{xy\downarrow}^\dagger |0\rangle, \quad (6.4b)$$

and likewise with a doubly occupied yz instead of the xz . In principle, the d^5 configurations with a singly occupied xy orbital given by

$$|d^5, xy \uparrow\rangle = c_{yz\uparrow}^\dagger c_{yz\downarrow}^\dagger c_{xz\uparrow}^\dagger c_{xz\downarrow}^\dagger c_{xy\uparrow}^\dagger |0\rangle \quad (6.5a)$$

$$|d^5, xy \downarrow\rangle = c_{yz\uparrow}^\dagger c_{yz\downarrow}^\dagger c_{xz\uparrow}^\dagger c_{xz\downarrow}^\dagger c_{xy\downarrow}^\dagger |0\rangle, \quad (6.5b)$$

could be considered, but those states cannot be reached with a single transition from the d^4 states described in eq. (6.2) or eq. (6.3) and thus are not observable with optical spectroscopy. Thus, we will not consider them in the calculation of the spectral weight. Eventually, these states might be somewhat relevant if one considers that the xy orbital is not fully occupied.

Now, focusing on the d^3 states, we have the 4A_2 , 2E , and 2T_1 multiplets that have been discussed previously as the most prominent ones.

The 4A_2 multiplet has states with $|S_z| \pm 3/2$ and $\pm 1/2$ given by

$$|d^3, {}^4A_2, 3/2\rangle = c_{yz\uparrow}^\dagger c_{xz\uparrow}^\dagger c_{xy\uparrow}^\dagger |0\rangle \quad (6.6a)$$

$$|d^3, {}^4A_2, 1/2\rangle = \frac{1}{\sqrt{3}} \left(c_{yz\uparrow}^\dagger c_{xz\uparrow}^\dagger c_{xy\downarrow}^\dagger + c_{yz\uparrow}^\dagger c_{xz\downarrow}^\dagger c_{xy\uparrow}^\dagger + c_{yz\downarrow}^\dagger c_{xz\uparrow}^\dagger c_{xy\uparrow}^\dagger \right) |0\rangle, \quad (6.6b)$$

where the states with $S_z = -\frac{3}{2}$ and $-\frac{1}{2}$ are omitted.

At $T = 0$, the ground state is antiferromagnetic. In a two-site scenario, the ground state is a spin singlet. However, on a square lattice, the AFM ground state is a total singlet and not a singlet on a particular given bond. Thus, when considering two adjacent sites in the AFM ordered state, we use the Néel state as the ground state, which is given by a product of the states described by eq. (6.3) of the form $|d_i^4 \uparrow\rangle |d_j^4 \downarrow\rangle$. The contribution of excitations from this ground state to $d^3 d^5$ states involving the $|d_i^3, {}^4A_2, 3/2\rangle$ state is zero. This is the case because, if we consider the spin selection rule for optical spectroscopy, i.e., only spin-conserving hopping allowed, the $|d_i^3, {}^4A_2, 3/2\rangle$ state cannot be reached because on site j ($|d_j^4 \downarrow\rangle$) all down-spin states are occupied. On the other hand, transitions to the $|d_i^3, {}^4A_2, 1/2\rangle$ state are not spin-forbidden in the AFM ground state. This can be easily seen by checking that the hopping of a $xy \uparrow$ electron on site i to the $xz \uparrow$ on site j is allowed⁶ and connects the $|d_i^4 \uparrow\rangle |d_j^4 \downarrow\rangle$ ground state to

⁶This is the case because of rotations and tilt of the octahedra. It is not the case in a cubic situation with 180° bonds. The latter had been assumed by [153]. In the present case, neglecting the rotations and tilts hence yields an erroneous peak assignment.

Chapter 6: Mott-Hubbard excitations in Ca_2RuO_4

$|d_i^3, {}^4A_2, 1/2\rangle |d_j^5 yz \downarrow\rangle$. Writing this last statement in an equation form we get the transition matrix element

$$M = \langle d_i^3, {}^4A_2, 1/2 | \langle d_j^5, yz \downarrow | t_{xy,xz} c_{xz\uparrow,j}^\dagger c_{xy\uparrow,i} | d_i^4 \uparrow \rangle | d_j^4 \downarrow \rangle. \quad (6.7)$$

and when considering the prefactor for $|d_i^3, {}^4A_2, 1/2\rangle$ in eq. (6.6b) we obtain that the transition matrix element is

$$M = t_{xy,xz} / \sqrt{3} \quad (6.8)$$

thus giving an intensity of

$$I = M^2 = t_{xy,xz}^2 / 3 \quad (6.9)$$

Now, we have to consider the related excited state $|d_i^3, {}^4A_2, 1/2\rangle |d_j^5, xz \downarrow\rangle$. Following the same argument, this state can be reached from an AFM ground state with a matrix element given by $t_{xy,yz} / \sqrt{3}$ and intensity $t_{xy,yz}^2 / 3$. This is a different final state but sharing the same energy as the process shown in eq. (6.7), and the resulting intensities must be added.

If we swap i and j in the previous argument, we obtain two more contributions to the intensity. Thus, ultimately, four orthogonal final states can be reached from $|d_i^4 \uparrow\rangle |d_j^4 \downarrow\rangle$ given by

$$|d_i^3, {}^4A_2, 1/2\rangle |d_j^5, yz \downarrow\rangle \quad (6.10a)$$

$$|d_i^3, {}^4A_2, 1/2\rangle |d_j^5, xz \downarrow\rangle \quad (6.10b)$$

$$|d_i^5, yz \uparrow\rangle |d_j^3, {}^4A_2, -1/2\rangle \quad (6.10c)$$

$$|d_i^5, xz \uparrow\rangle |d_j^3, {}^4A_2, -1/2\rangle \quad (6.10d)$$

and resulting in a total intensity for the 4A_2 multiplet for two sites in the antiferromagnetic ordered state as

$$I_{T=0,\uparrow\downarrow}({}^4A_2) = \frac{2}{3} \left[t_{xy,xz}^2 + t_{xy,yz}^2 \right]. \quad (6.11)$$

Considering ferromagnetic order instead, the situation is reversed, and it can be easily checked that only the $|{}^4A_2, 3/2\rangle$ state is part of the transition. Thus, for

ferromagnetic order as the ground state given by $|d_i^4 \uparrow\rangle |d_j^4 \uparrow\rangle$ the transition matrix element to a final state $|{}^4A_2, 3/2\rangle$ reads

$$M = \langle d_i^3, {}^4A_2, 3/2 | \langle d_j^5, yz \uparrow | t_{xy,xz} c_{xz\downarrow,j}^\dagger c_{xy\downarrow,i} | d_i^4 \uparrow \rangle | d_j^4 \uparrow \rangle$$

and since the prefactor of the $|{}^4A_2, 3/2\rangle$ state is 1 (see eq. (6.6)a), the transition matrix element is given by

$$M = t_{xy,xz} \quad (6.12)$$

As in the previous case, it is possible for both xz and yz orbitals and in both directions, i to j or vice versa. Thus, from $|d_i^4 \uparrow\rangle |d_j^4 \uparrow\rangle$ we ultimately obtain again four orthogonal final states with the same energy given by

$$|d_i^3, {}^4A_2, 3/2\rangle |d_j^5, yz \uparrow\rangle \quad (6.13a)$$

$$|d_i^3, {}^4A_2, 3/2\rangle |d_j^5, xz \uparrow\rangle \quad (6.13b)$$

$$|d_i^5, yz \uparrow\rangle |d_j^3, {}^4A_2, 3/2\rangle \quad (6.13c)$$

$$|d_i^5, xz \uparrow\rangle |d_j^3, {}^4A_2, 3/2\rangle \quad (6.13d)$$

where we have to add their intensities, yielding a total intensity of

$$I_{T=0,\uparrow\uparrow}({}^4A_2) = 2 \left[t_{xy,xz}^2 + t_{xy,yz}^2 \right] \quad (6.14)$$

for two sites with parallel moments.

We proceed to calculate the situation at high temperatures, where no magnetic order is present. For the sake of simplicity, we will consider the $S_z = 0$ states later and first will focus on the case when the ground state has only the $S_z = \pm 1$ components. In this case, the magnetically disordered state at high temperature is a mix of four configurations, $(\uparrow\uparrow + \downarrow\downarrow + \uparrow\downarrow + \downarrow\uparrow)$ with a probability of $1/4$ each. As we saw before, the final states are orthogonal for $T = 0$ in AFM and FM order. Thus we have to add the intensities originating from each configuration weighted by $1/4$. With this, we have all the pieces to obtain the intensity at high tempera-

ture for two sites which is given by

$$\begin{aligned}
 I_{high}({}^4A_2) &= \frac{1}{4} [I_{T=0,\uparrow\uparrow}({}^4A_2) + I_{T=0,\uparrow\downarrow}({}^4A_2) \\
 &\quad + I_{T=0,\downarrow\uparrow}({}^4A_2) + I_{T=0,\downarrow\downarrow}({}^4A_2)] \\
 &= \frac{1}{2} [I_{T=0,\uparrow\uparrow}({}^4A_2) + I_{T=0,\uparrow\downarrow}({}^4A_2)] \\
 &= \frac{4}{3} [t_{xy,xz}^2 + t_{xy,yz}^2]
 \end{aligned}$$

Now, the ratio of the intensities, which is directly related to the ratio of spectral weight, between the high- and low-temperature states for the 4A_2 multiplet is given by

$$\frac{I_{high}({}^4A_2)}{I_{T=0,\uparrow\downarrow}({}^4A_2)} = 2, \quad (6.15)$$

and thus we expect that the spectral weight of the peak associated with the multiplet 4A_2 to double from low to high temperature when neglecting the $S_z = 0$ states.

It is worthy to note, that in the ideal cubic case, the hopping $t_{xy,xz}$ vanishes, but it is finite when tilts and rotations of the octahedra are in play, which is the case for Ca_2RuO_4 as we have already seen previously when discussing the crystal structure. However, structural changes will affect the hopping and thus also the temperature dependence of the spectral weight.

We continue with the 2E multiplet, once again taking into account only the $S_z = \pm 1$ components and following the same kind of argument as with the 4A_2 multiplet.

$$|{}^2E, a\rangle = \frac{1}{\sqrt{6}} \left(-2c_{yz\uparrow}^\dagger c_{xz\uparrow}^\dagger c_{xy\downarrow}^\dagger + c_{yz\uparrow}^\dagger c_{xz\downarrow}^\dagger c_{xy\uparrow}^\dagger + c_{yz\downarrow}^\dagger c_{xz\uparrow}^\dagger c_{xy\uparrow}^\dagger \right) |0\rangle, \quad (6.16a)$$

$$|{}^2E, b\rangle = \frac{1}{\sqrt{2}} \left(c_{xz\uparrow}^\dagger c_{yz\downarrow}^\dagger - c_{xz\downarrow}^\dagger c_{yz\uparrow}^\dagger \right) c_{xy\uparrow}^\dagger |0\rangle \quad (6.16b)$$

As with the previous case, the calculation of the transition matrix elements is straightforward to perform. Transitions from the ground state (eq. (6.2)) into states in the d^3 sector can be reached only when the spins on the xz and yz

orbitals are parallel. Thus, when the ground state has AFM order, the first term of eq. (6.16)a) can be reached with a matrix element of $-\sqrt{2/3}t_{xy,xz}$. This matrix element is $\sqrt{2}$ larger than the one for the 4A_2 multiplet. Thus, we expect a factor of 2 in the intensity compared to the 4A_2 multiplet. For FM order, the matrix element is 0, indicating that this excitation is not possible. This leads to the expectation of a drop in intensity by a factor of 2 from the low- to the high-temperature phase.

$$\begin{aligned} I_{high}({}^2E) &= \frac{1}{4} [I_{T=0,\uparrow\uparrow}({}^2E) + I_{T=0,\uparrow\downarrow}({}^2E) \\ &\quad + I_{T=0,\downarrow\uparrow}({}^2E) + I_{T=0,\downarrow\downarrow}({}^2E)] \\ &= \frac{1}{2} I_{T=0,\uparrow\downarrow}({}^2E) \end{aligned}$$

Unfortunately, this value does not bring us very far because the peak originating from the 2E multiplet is from a very broad band which overlaps with charge-transfer excitations, thus making this very difficult to corroborate experimentally.

At last, we have the 2T_1 multiplet. As described above, we hence assign the second peak in $\sigma_1(\omega)$ at about 2 eV to the 2T_1 multiplet. This multiplet is given by

$$|{}^2T_1, xz \uparrow\rangle = \frac{1}{\sqrt{2}} (c_{xz\uparrow}^\dagger c_{xy\uparrow}^\dagger c_{xy\downarrow}^\dagger - c_{yz\uparrow}^\dagger c_{yz\downarrow}^\dagger c_{xz\uparrow}^\dagger) |0\rangle, \quad (6.17a)$$

$$|{}^2T_1, yz \uparrow\rangle = \frac{1}{\sqrt{2}} (c_{xy\uparrow}^\dagger c_{xy\downarrow}^\dagger - c_{xz\uparrow}^\dagger c_{xz\downarrow}^\dagger) c_{yz\uparrow}^\dagger |0\rangle, \quad (6.17b)$$

where the singly occupied xy orbital is omitted due to the impossibility of reaching it from the xy ordered ground state.

Extracting from the appendix the allowed transitions for the AFM ground state, we obtain the intensity as

$$I_{T=0,\uparrow\downarrow}({}^2T_1) = [t_{yz,yz}^2 + t_{yz,xz}^2 + t_{xz,xz}^2 + t_{xz,yz}^2]. \quad (6.18)$$

When considering a ferromagnetic ground state, excitations to the 2T_1 multiplets are forbidden, which can be quickly corroborated by checking the tables in the appendix, thus

$$I_{T=0,\uparrow\uparrow}({}^2T_1) = 0. \quad (6.19)$$

This means that when we calculate the total intensity for the 2T_1 multiplet in the high-temperature state, we obtain

$$\begin{aligned} I_{high}({}^2T_1) &= \frac{1}{4} [I_{T=0,\uparrow\uparrow}({}^2T_1) + I_{T=0,\uparrow\downarrow}({}^2T_1) \\ &\quad + I_{T=0,\downarrow\uparrow}({}^2T_1) + I_{T=0,\downarrow\downarrow}({}^2T_1)] \\ &= \frac{1}{2} I_{T=0,\uparrow\downarrow}({}^2T_1) \end{aligned}$$

namely, the intensity related to the 2T_1 multiplet shows a reduction by a factor of 2 when neglecting the S_z states.

6.4.5. $S_z = 0$ states

The calculation considering only the $S_z = \pm 1$ components already gives the correct order of magnitude and direction of the change in the spectral weight as a function of temperature in line with what we observed in our measurements only for the lowest energy peak. Although this straightforward estimation points us in the right direction, at high temperature, the $S_z = 0$ component of the d^4 configurations also should be taken into account to get a more complete picture.

When considering contributions stemming from the $S_z = 0$ component of the ground state (eq. (6.3)), for a nearest-neighbor pair, we obtain $3 \cdot 3 = 9$ different states represented as

$$|\uparrow\uparrow\rangle, |\downarrow\downarrow\rangle, |\uparrow\downarrow\rangle, |\downarrow\uparrow\rangle, |\uparrow 0\rangle, |0 \uparrow\rangle, |\downarrow 0\rangle, |0 \downarrow\rangle, |00\rangle \quad (6.20)$$

At high enough temperatures far above T_N , the $S_z = 0$ component has the same probability as the $S_z = \pm 1$ components, *i.e.*, $1/9$ each. Now, we only have to compute the contributions of the states that include the $S_z = 0$ component, namely, the last 5 terms of eq. (6.20) since the first four states were already calculated. As done in the case where we only considered the $S_z = \pm 1$ components, the intensities also must be added. Since the density of magnons is temperature dependent, it is clear that more care has to be taken with the probabilities of each state for intermediate temperatures closer to the magnetic ordering. For our purposes, it is enough to focus on high temperature, the fully disordered state.

As in the previous case, we can use a symmetry argument to simplify the calculation by noting that the matrix elements for the 4 states $|\uparrow 0\rangle, |0 \uparrow\rangle, |\downarrow 0\rangle, |0 \downarrow\rangle$

are identical.

Starting with the 4A_2 multiplet and using the transition matrix elements calculated in the appendix, we obtain the intensity for the transition $d_0^4 d_{\uparrow}^4$

$$I({}^4A_2)_{0\uparrow} = \frac{2}{3} \left[t_{xy,xz}^2 + t_{xy,yz}^2 + t_{xz,xy}^2 + t_{yz,xy}^2 \right]. \quad (6.21)$$

Then, the only one missing from the nine possible ground states is the $d_0^4 d_0^4$ one. Again, consulting the summary table in the appendix, we obtain for the 4A_2 multiplet

$$I({}^4A_2)_{00} = \frac{2}{3} \left[t_{xy,xz}^2 + t_{xy,yz}^2 + t_{xz,xy}^2 + t_{yz,xy}^2 \right] \quad (6.22)$$

With all the pieces calculated, we can sum them all up

$$\begin{aligned} I({}^4A_2) &= \frac{1}{9} \left(4I({}^4A_2)_{0\uparrow} + I({}^4A_2)_{00} + 4I_{high}({}^4A_2)_{S_z=1} \right) \\ &= \frac{1}{9} \left[4\frac{2}{3} + \frac{8}{3} + \frac{2}{3} \right] \left(t_{xy,xz}^2 + t_{xy,yz}^2 + t_{xz,xy}^2 + t_{yz,xy}^2 \right) \\ &= \frac{2}{3} \left(t_{xy,xz}^2 + t_{xy,yz}^2 + t_{xz,xy}^2 + t_{yz,xy}^2 \right) \end{aligned}$$

and then divide by the intensity for this multiplet in the ground state at low-temperature

$$\frac{I({}^4A_2)}{I({}^4A_2)_{\uparrow\downarrow}} = 2 \quad (6.23)$$

We hence obtain the same ratio as with the calculation that takes into account only the $S_z = \pm 1$ components.

We do the same for the 2T_1 multiplet. First, we obtain the intensity of the $d_0^4 d_{\uparrow}^4$ contribution to the intensity, which leads to

$$I({}^2T_1)_{0\uparrow} = \frac{1}{2} \left(t_{yz,xz}^2 + t_{yz,yz}^2 + t_{xz,xz}^2 + t_{xz,yz}^2 \right). \quad (6.24)$$

	1 eV	2 eV
Exp	~ 2.4	~ 1.3
$S_z = \pm 1$	2	0.5
$S_z = \pm 1, 0$	2	0.5

Table 6.5.: Summary of the ratio of the spectral weight between high and low temperature for both oscillators observed and the calculations considering only the $S_z = \pm 1$ component or including the $S_z = 0$ one too.

Then, we perform the same calculation for the $d_0^4 d_0^4$ ground state, obtaining

$$I(^2T_1)_{00} = \frac{1}{2} [t_{yz,xz}^2 + t_{yz,yz}^2 + t_{xz,xz}^2 + t_{xz,yz}^2]. \quad (6.25)$$

With all the pieces calculated, we can sum them all up

$$\begin{aligned} I(^2T_1)_{00} &= \frac{1}{9} (4I(^2T_1)_{0\uparrow} + I(^2T_1)_{00} + 4I_{high}(^2T_1)_{S=1}) \\ &= \frac{1}{9} \left(4\frac{1}{2} + \frac{1}{2} + 2 \right) [t_{yz,xz}^2 + t_{yz,yz}^2 + t_{xz,xz}^2 + t_{xz,yz}^2] \\ &= \frac{1}{9} \frac{9}{2} (t_{yz,xz}^2 + t_{yz,yz}^2 + t_{xz,xz}^2 + t_{xz,yz}^2), \end{aligned} \quad (6.26)$$

and then divide by $I(^2T_1)_{\uparrow\downarrow} = [t_{yz,xz}^2 + t_{yz,yz}^2 + t_{xz,xz}^2 + t_{xz,yz}^2]$. Then, the ratio between disordered and ordered states for the 2T_1 is

$$\frac{I(^2T_1)}{I(^2T_1)_{\uparrow\downarrow}} = \frac{1}{2}. \quad (6.27)$$

This value is the same as the one obtained with the calculation considering only the $S_z = \pm 1$ ground states. The same caveats apply, as factors like changes of tilts, distortions, and rotations are not being considered.

To summarize, in the case of the first peak, our calculated ratio is in the right direction and magnitude of what we experimentally estimate, recognizing an increase in the spectral weight as a function of temperature. However, our calculations expect a halving of the spectral weight for the second peak, which contradicts our experimental finding by a fair margin.

These results have to be taken with care, as we are neglecting how tilts, rotations, and distortions of the octahedra may change as a function of temperature. Moreover, we are using an effectively infinite temperature scenario where all the possible ground states contribute the same weight to the result. Furthermore, the spin-orbit coupling may affect the selection rules and thus how the transition matrix elements show up.

Furthermore, the absence of clear changes in the spectral weight in the vicinity of T_N suggests that the spin degree of freedom is not the dominant factor for the spectral weight. A more detailed analysis has to consider the role of spin-orbit coupling and its effect on the electronic states and the matrix elements.

6.5. Conclusion

We measured the linear optical response of two calcium ruthenate samples that differ in the amount of Ti doping. We aimed to map the temperature dependence of the optical conductivity in a more precise fashion. The 1% Ti in Ca_2RuO_4 is a necessity to stabilize the structure. Furthermore, the absence of clear changes of the spectral weight in the vicinity of T_N suggests that the spin degree of freedom is not the dominant factor for the spectral weight. A more detailed analysis has to consider the role of spin-orbit coupling and its effect on the electronic states and the matrix elements.

As with previous reports, we observe two main features in the low energy sector of the spectra. The first feature increases in spectral weight while shifting to lower energies as a function of temperature. The second feature's temperature behavior has not been unambiguously described in the literature. Based on our experimental data, we observe an increase in its spectral weight as a function of temperature.

A more detailed analysis of the optical properties is achieved by using an optical model fitted to the data. This step is enabled reliably by measuring both parts of the optical properties provided by spectroscopic ellipsometry. Focusing on the 1% doped sample, the best-constructed model to describe the features observed in the data consists of 5 Gaussian oscillators. From those, the first and second lowest energy oscillators are the most interesting ones since they correspond to inter-site Mott-Hubbard excitations. With the help of the oscillators defined in the model, we confirm the already mentioned behavior of the first and second features obtaining a change of ~ 2.4 and ~ 1.3 , respectively, in their spectral weights when going from 15 K to 300 K. Moreover, we do not observe a significant

change across T_N .

Our peak assignment, considering cubic approximation, results in the peaks at 1 eV and 2 eV to correspond to the excitations from the ground state to the $|d_i^3(^4A_2), d_j^5(^2T_2)\rangle$ and $|d_i^3(^2T_2/{}^2E), d_j^5(^2T_2)\rangle$, respectively. This assignment disagrees with the one by Lee et al. [153], who omits the tilt and rotation of the octahedra on top of neglecting spin-orbit coupling.

Furthermore, we attempted to estimate the magnitudes and direction of the change in spectral weight by calculating the matrix elements of the possible excitations. We compute the change of spectral weight between the antiferromagnetically ordered and fully disordered states in the scenarios of pure $S_z = \pm 1$ or with $S_z = 0, \pm 1$ components for the ground state of Ca_2RuO_4 which is summarized in table 6.5. We find the same values for both cases, namely, a ratio of 2 for the first oscillator and 0.5 for the second. The calculated ratio provides the correct direction and magnitude for the observed behavior in the optical conductivity of the 1 eV feature. Still, the magnitude falls a bit short. When considering the feature at about 2 eV, the situation is very different, and the opposite direction than the one found experimentally is to be expected. It is clear that our picture, even when considering the $S_z = 0$ states, is not enough to describe the behavior of both peaks fully, in particular, the second peak in the optical conductivity.

Considering only the spin takes us far into trying to understand this system, particularly the behavior of the first peak; however, it is clear that something is missing, namely the spin-orbit coupling to account for the observed data fully. More in-depth analysis of the role of the spin-orbit coupling ($\zeta = 2\lambda$) in this compound, based on these optical conductivity measurements [185], reveals that the optical spectral weight of the Mott-Hubbard excitations to be a direct measure of Δ_{CF}/ζ where it is estimated to have a lower bound of 2.4. As concluded in Vergara et al. [185] "*In the end, the captivating character of Ca_2RuO_4 is based on the competition of spin-orbit coupling and crystal field rather than on the dominance of one of them.*".

A few words on the 10% Ti doped sample. When comparing both samples' behavior, the temperature dependence of the oscillators' energy is very similar. This indicates that the basic energy levels do not change much with the distortion introduced by doping. The shift of the two lowest oscillators, by about 0.2 eV, may indicate a change in Δ_{CF} . Furthermore, the enhancement of the optical conductivity for the 10% doped sample compared to the 1% doped one may be explained by oscillator number 3, which has very different characteristics between the two samples. Such peak is possibly a charge-transfer excitation that is considerably lowered in energy due to the Ti doping.

7. Conclusion

You see, one thing is, I can live with doubt and uncertainty and not knowing. I think its much more interesting to live not knowing than to have answers which might be wrong.

Richard P. Feynman

In this work, different strongly correlated materials were investigated with optical spectroscopic tools, namely spectroscopic ellipsometry and Fourier spectroscopy. We studied three materials corresponding to three different systems: the classic magnetite (Fe_3O_4) as a bulk $3d^5/3d^6$ system, $\text{La}_2\text{Cu}_2\text{O}_5$ as a low-dimensional spin-1/2 ladder system, and Ca_2RuO_4 as a layered $4d^4$ system.

In all the studied systems, the biggest challenge was the construction of an optical model allowing us to describe and understand the system and the measurements, mainly while using ellipsometry. As discussed in this work, spectroscopic ellipsometry is a very powerful tool as it can measure enough information to construct the full dielectric function of the sample being studied and thus obtain the real and imaginary parts of the optical conductivity of the material. Having both parts tends to make the fitting of optical models more stable, or in some cases, even possible since the model has to be consistent for two different but highly correlated values.

The study of the low-dimensional system $\text{La}_2\text{Cu}_2\text{O}_5$, a 4-leg ladder, is strongly motivated by the particular physics found in other low-dimensional systems like the $S = 1/2$ chain or 2-leg spin ladder. Even more so, it is motivated by the puzzling emergence of superconductivity in two-dimensional cuprates and doped 2-leg cuprate spin ladders. In particular, the 4-leg ladder can be seen as a small step moving from an almost 1D system towards a quasi-2D system. Understanding the dimensional crossover could lead to a better understanding of the physics in the complex 2D layered cuprates.

Chapter 7: Conclusion

We successfully measured the first optical spectra of a 4-leg $S = 1/2$ ladder via Fourier spectroscopy. The obtained spectra have a strong resemblance to the 2-leg ladder ones, hinting that some 2-leg character still survives when going from 2 to 4 legs. This similitude in the spectra of 2- and 4-leg ladders leads to interpreting their features in similar terms. With the help of numerical calculations of two different theoretical models, we interpret the observed features as a low-energy peak stemming from a 2-triplon quasi-bound state and a broad feature arising from the continuum of magnetic excitations. Furthermore, there is one extra feature of a clear peak with a satellite shoulder. Its origin is not completely clear but could be from the combination of a higher-energy bound state and a bimagnon-like resonance which resembles the case of a 2D square lattice.

One extra insight from theory is that it provides a very plausible argument regarding the contributions to the magnetic excitations, which could be assigned to the outer and inner legs. Thus, from the outer legs come most of the contributions to the bound state signal, whereas from the inner legs originate mainly contributions to the continuum. Although this outcome would be challenging to test, particularly with static optical techniques, as an insight, it is very interesting since it makes sense that the response from the inner legs resembles the 2D behavior.

Magnetite is most likely one of the most studied materials in the field of correlated electron systems. Regardless of this fact, there are still controversies and open questions regarding its physics. What began as a collaboration to obtain this material's optical spectra to support non-linear reflectivity measurements ended up being an in-depth investigation with spectroscopic ellipsometry. In this work, we report the optical conductivity behavior as a function of temperature focusing on the magnetic phase transition.

The existing literature on magnetite's optical conductivity was unclear, particularly around the optical feature around 2 eV, as reported by reflectivity measurements performed via Fourier spectroscopy. In one case, this feature was not observed and, in other instances, showed different temperature-dependent behavior [30, 119]. Our ellipsometric measurements allowed us to clarify the discrepancy found in the literature. We clearly observe two features, sitting at 0.6 eV and 1.9 eV. Those features show opposite temperature dependence, where the first increases while the second one decreases as the temperature increases. The detailed temperature-dependent measurement displays a step-like behavior across the Verwey metal-insulator phase transition for these features. Furthermore, the interpretation of these features was controversial. We interpret the excitations as intersite transitions of minority spins from the $\text{Fe}_B^{2+} t_{2g}$ levels to the t_{2g} and e_g

levels of Fe_B^{3+} sites, respectively.

Our data was used to establish the baseline reflectivity of magnetite for a non-equilibrium study [120]. This study found that three different regimes of the out-of-equilibrium spectra can be triggered below T_V , which depends on the pump's fluence. This shows that a strong photoexcitation process can produce an out-of-equilibrium response analogous to the Verwey phase transition.

As with $\text{La}_2\text{Cu}_2\text{O}_5$, the last system studied is a layered bulk system that also has connections to superconducting materials. The ruthenates differ considerably from the cuprates since they belong to the $4d$ class of materials with significantly different physics than the $3d$ systems due to the larger electronic radius of the orbital and eventual spin-orbit coupling effects. Notably, the role of magnetism is more relevant in this class of materials, and the close relationship between this and superconductivity is not what is expected in classical superconductors.

The ruthenate studied here, Ca_2RuO_4 , has been studied previously but with contradicting optical spectra and interpretations. It is agreed that the two features observed at about 1 and 2 eV belong to $d^4d^4 \rightarrow d^3d^5$ Mott-Hubbard excitations. Still, the behavior of those features as a function of temperature was not clearly reported. We set to investigate in depth, with spectroscopic ellipsometry, the temperature-dependent optical spectra of Ca_2RuO_4 with 1% and 10% Ti doping. Since the 1% doped system is the closest one to the pure system, this one took most of our attention. The Ti doping of 1% is needed to ensure the sample's mechanical stability while cooling in the crystal growth process.

Our measurement and analysis allowed us to dispel the contradiction between previous reports, establishing that the first feature increases considerably in spectral weight as a function of temperature while the second one marginally increases. Furthermore, we performed a transition matrix element calculation to obtain the expected changes in spectral weight between the magnetically ordered ground state at low temperature and a fully disordered state at high temperature. From these results, only the one for the first feature shows a correct magnitude when contrasted with the experimental value obtained. As for the second transition, it shows the opposite behavior as what is experimentally observed, namely a reduction of the spectral weight as a function of temperature. It is important to mention that the calculation only considers spin changes, excluding orbitals and spin-orbit coupling. Given the results obtained, there are certainly some aspects of the system that our simple model doesn't cover, one that predominantly affects the 2 eV feature. In any case, we have to keep in mind that effects stemming from the temperature dependence of tilts, distortions, and rotations of the RuO_6 octahedra were not considered. Furthermore, we are also assuming that all possible

Chapter 7: Conclusion

$S_z = 0$ ground states contribute equally in the high-temperature situation.

A. Appendix

Two-site matrix elements elements like

$$\langle d_{i,s}^5 | \langle d_{j,s'}^3 | t_{k,k'} c_{i,k}^\dagger c_{j,k'} | d_{i,r}^4 \rangle | d_{j,r'}^4 \rangle \quad (\text{A.1})$$

with site i, j , and states distinguished by s, s', r, r' and orbitals k, k' , can be separated into one-site matrix elements

$$-t_{kk'} \langle d_{i,s}^5 | c_{i,k}^\dagger | d_{i,r}^4 \rangle \langle d_{j,s'}^3 | c_{j,k'} | d_{j,r'}^4 \rangle \quad (\text{A.2})$$

For the matrix elements in $\langle d_s^5 | c_k^\dagger | d_r^4 \rangle$, applying all possible c^\dagger on the doubly occupied xy orbital as initial $|d^4\rangle$ state, and accounting for the commutation rules for fermionic creation/annihilation operators we obtain

$$c_{xz\downarrow}^\dagger |d^4 \uparrow\rangle = c_{yz\uparrow}^\dagger c_{xz\uparrow}^\dagger c_{xz\downarrow}^\dagger c_{xy\uparrow}^\dagger c_{xy\downarrow}^\dagger |0\rangle = + |d_{yz,\uparrow}^5\rangle$$

$$c_{yz\downarrow}^\dagger |d^4 \uparrow\rangle = -c_{yz\uparrow}^\dagger c_{yz\downarrow}^\dagger c_{xz\uparrow}^\dagger c_{xy\uparrow}^\dagger c_{xy\downarrow}^\dagger |0\rangle = - |d_{xz,\uparrow}^5\rangle$$

$$c_{xz\uparrow}^\dagger |d^4 \downarrow\rangle = -c_{yz\downarrow}^\dagger c_{xz\uparrow}^\dagger c_{xz\downarrow}^\dagger c_{xy\uparrow}^\dagger c_{xy\downarrow}^\dagger |0\rangle = - |d_{yz,\downarrow}^5\rangle$$

$$c_{yz\uparrow}^\dagger |d^4 \downarrow\rangle = c_{yz\uparrow}^\dagger c_{yz\downarrow}^\dagger c_{xz\downarrow}^\dagger c_{xy\uparrow}^\dagger c_{xy\downarrow}^\dagger |0\rangle = + |d_{yz,\downarrow}^5\rangle$$

$$c_{xz\downarrow}^\dagger |d^4 0\rangle = \frac{1}{\sqrt{2}} c_{yz\downarrow}^\dagger c_{xz\uparrow}^\dagger c_{xz\downarrow}^\dagger c_{xy\uparrow}^\dagger c_{xy\downarrow}^\dagger |0\rangle = + \frac{1}{\sqrt{2}} |d_{yz,\downarrow}^5\rangle$$

$$c_{yz\downarrow}^\dagger |d^4 0\rangle = -\frac{1}{\sqrt{2}} c_{yz\uparrow}^\dagger c_{yz\downarrow}^\dagger c_{xz\downarrow}^\dagger c_{xy\uparrow}^\dagger c_{xy\downarrow}^\dagger |0\rangle = -\frac{1}{\sqrt{2}} |d_{xz,\downarrow}^5\rangle$$

$$c_{xz\uparrow}^\dagger |d^4 0\rangle = -\frac{1}{\sqrt{2}} - c_{yz\uparrow}^\dagger c_{xz\uparrow}^\dagger c_{xz\downarrow}^\dagger c_{xy\uparrow}^\dagger c_{xy\downarrow}^\dagger |0\rangle = -\frac{1}{\sqrt{2}} |d_{yz,\uparrow}^5\rangle$$

$$c_{yz\uparrow}^\dagger |d^4 0\rangle = \frac{1}{\sqrt{2}} c_{yz\uparrow}^\dagger c_{yz\downarrow}^\dagger c_{xz\uparrow}^\dagger c_{xy\uparrow}^\dagger c_{xy\downarrow}^\dagger |0\rangle = +\frac{1}{\sqrt{2}} |d_{xz,\uparrow}^5\rangle$$

This set of equations can be easily reused to obtain the matrix elements for initial states with double occupancy in xz or yz orbitals.

The same procedure can be performed for the matrix elements in $\langle d_s^3 | c_k | d_r^4 \rangle$

$$c_{xy\downarrow} |d^4 \uparrow\rangle = -c_{yz\uparrow}^\dagger c_{xz\uparrow}^\dagger c_{xy\uparrow}^\dagger c_{xy\downarrow}^\dagger |0\rangle = -|yz \uparrow \ xz \uparrow \ xy \uparrow\rangle$$

$$c_{xy\uparrow} |d^4 \uparrow\rangle = c_{yz\uparrow}^\dagger c_{xz\uparrow}^\dagger c_{xy\uparrow}^\dagger c_{xy\downarrow}^\dagger |0\rangle = +|yz \uparrow \ xz \uparrow \ xy \downarrow\rangle$$

$$c_{xz\uparrow} |d^4 \uparrow\rangle = -c_{yz\uparrow}^\dagger c_{xz\uparrow}^\dagger c_{xy\uparrow}^\dagger c_{xy\downarrow}^\dagger |0\rangle = -|yz \uparrow \ xy \uparrow \ xy \downarrow\rangle$$

$$c_{yz\uparrow} |d^4 \uparrow\rangle = c_{yz\uparrow}^\dagger c_{xz\uparrow}^\dagger c_{xy\uparrow}^\dagger c_{xy\downarrow}^\dagger |0\rangle = +|xz \uparrow \ xy \uparrow \ xy \downarrow\rangle$$

$$c_{xy\downarrow} |d^4 \downarrow\rangle = -c_{yz\downarrow}^\dagger c_{xz\downarrow}^\dagger c_{xy\uparrow}^\dagger c_{xy\downarrow}^\dagger |0\rangle = -|yz \downarrow \ xz \downarrow \ xy \uparrow\rangle$$

$$c_{xy\uparrow} |d^4 \downarrow\rangle = c_{yz\downarrow}^\dagger c_{xz\downarrow}^\dagger c_{xy\uparrow}^\dagger c_{xy\downarrow}^\dagger |0\rangle = +|yz \downarrow \ xz \downarrow \ xy \downarrow\rangle$$

$$c_{xz\downarrow} |d^4 \downarrow\rangle = -c_{yz\downarrow}^\dagger c_{xz\downarrow}^\dagger c_{xy\uparrow}^\dagger c_{xy\downarrow}^\dagger |0\rangle = -|yz \downarrow \ xy \uparrow \ xy \downarrow\rangle$$

$$c_{yz\downarrow} |d^4 \downarrow\rangle = c_{yz\downarrow}^\dagger c_{xz\downarrow}^\dagger c_{xy\uparrow}^\dagger c_{xy\downarrow}^\dagger |0\rangle = |xz \downarrow \ xy \uparrow \ xy \downarrow\rangle$$

$$c_{yz\downarrow} |d^4 0\rangle = \frac{1}{\sqrt{2}} c_{yz\downarrow}^\dagger c_{yz\downarrow}^\dagger c_{xz\uparrow}^\dagger c_{xy\uparrow}^\dagger c_{xy\downarrow}^\dagger |0\rangle = +\frac{1}{\sqrt{2}} |xz \uparrow \ xy \uparrow \ xy \downarrow\rangle$$

$$c_{yz\uparrow} |d^4 0\rangle = \frac{1}{\sqrt{2}} c_{yz\uparrow}^\dagger c_{yz\uparrow}^\dagger c_{xz\downarrow}^\dagger c_{xy\uparrow}^\dagger c_{xy\downarrow}^\dagger |0\rangle = +\frac{1}{\sqrt{2}} |xz \downarrow \ xy \uparrow \ xy \downarrow\rangle$$

$$c_{xz\downarrow} |d^4 0\rangle = -\frac{1}{\sqrt{2}} c_{yz\uparrow}^\dagger c_{xz\downarrow}^\dagger c_{xz\downarrow}^\dagger c_{xy\uparrow}^\dagger c_{xy\downarrow}^\dagger |0\rangle = -\frac{1}{\sqrt{2}} |yz \uparrow \ xy \uparrow \ xy \downarrow\rangle$$

$$c_{xz\uparrow} |d^4 0\rangle = -\frac{1}{\sqrt{2}} c_{yz\downarrow}^\dagger c_{xz\uparrow}^\dagger c_{xz\uparrow}^\dagger c_{xy\uparrow}^\dagger c_{xy\downarrow}^\dagger |0\rangle = -\frac{1}{\sqrt{2}} |yz\downarrow xy\uparrow xy\downarrow\rangle$$

$$\begin{aligned} c_{xz\downarrow} |d^4 0\rangle &= \frac{1}{\sqrt{2}} \left[-c_{yz\downarrow}^\dagger c_{xz\uparrow}^\dagger c_{xy\uparrow}^\dagger c_{xy\downarrow}^\dagger c_{xy\downarrow}^\dagger - c_{yz\uparrow}^\dagger c_{xz\downarrow}^\dagger c_{xy\uparrow}^\dagger c_{xy\downarrow}^\dagger c_{xy\downarrow}^\dagger \right] |0\rangle \\ &= -\frac{1}{\sqrt{2}} [|yz\downarrow xz\uparrow xy\uparrow\rangle + |yz\uparrow xz\downarrow xy\uparrow\rangle] \end{aligned}$$

$$\begin{aligned} c_{xz\uparrow} |d^4 0\rangle &= \frac{1}{\sqrt{2}} \left[+c_{yz\downarrow}^\dagger c_{xz\uparrow}^\dagger c_{xy\uparrow}^\dagger c_{xy\uparrow}^\dagger c_{xy\downarrow}^\dagger + c_{yz\uparrow}^\dagger c_{xz\downarrow}^\dagger c_{xy\uparrow}^\dagger c_{xy\uparrow}^\dagger c_{xy\downarrow}^\dagger \right] |0\rangle \\ &= -\frac{1}{\sqrt{2}} [|yz\downarrow xz\uparrow xy\downarrow\rangle + |yz\uparrow xz\downarrow xy\downarrow\rangle] \end{aligned}$$

With all these transition matrix elements, we can project onto the respective multiplets of interest, namely $|^4A_2\rangle$ and $|^2T_1\rangle$ (eqs. (6.6) and (6.17)) to obtain the transition matrix elements of interest.

To make use of tables A.1 and A.2, one has to find the entries of interest in each one of them and then multiply them following eq. (A.2) and remembering that we have spin conservation, namely that we can not have a transition involving a spin flip.

For example, we were interested in knowing which is the transition matrix element connecting $\langle ^4A_2, 1/2 | \langle d_j^5 yz \downarrow |$ with $|d_i^4 \uparrow\rangle |d_j^4 \downarrow\rangle$. First, we search for the entries $\langle ^4A_2, 1/2 |, |d_i^4 \uparrow\rangle$ in table A.1 obtaining $\frac{1}{\sqrt{3}} c_{xy\uparrow}$. Then, we do the same with $\langle d_j^5 yz \downarrow |, |d_j^4 \downarrow\rangle$, but looking in table A.2 instead, we obtain $-c_{xz\uparrow}^\dagger$. Since both are different orbitals and same spin, it's allowed and its value is

$$\langle ^4A_2, 1/2 | \langle d_j^5 yz \downarrow | \frac{1}{\sqrt{3}} c_{xy\uparrow} |d_i^4 \uparrow\rangle |d_j^4 \downarrow\rangle \cdot \langle ^4A_2, 1/2 | \langle d_j^5 yz \downarrow | c_{xz\uparrow}^\dagger \langle ^4A_2, 1/2 |, |d_i^4 \uparrow\rangle = -\frac{1}{\sqrt{3}} t_{xy,xz}. \quad (\text{A.3})$$

	$ d^4 \uparrow\rangle$	$ d^4 0\rangle$	$ d^4 \downarrow\rangle$
$\langle^4A_2, 3/2 $	$-xy \downarrow$	0	0
$\langle^4A_2, -3/2 $	0	0	$xy \uparrow$
$\langle^4A_2, 1/2 $	$\frac{1}{\sqrt{3}}xy \uparrow$	$-\sqrt{\frac{2}{3}}xy \downarrow$	0
$\langle^4A_2, -1/2 $	0	$\sqrt{\frac{2}{3}}xy \downarrow$	$-\frac{1}{\sqrt{3}}xy \downarrow$
$\langle^2T_1, xz \uparrow $	$\frac{1}{\sqrt{2}}yz \uparrow$	$\frac{1}{2}yz \downarrow$	0
$\langle^2T_1, xz \downarrow $	0	$\frac{1}{2}yz \uparrow$	$\frac{1}{\sqrt{2}}yz \downarrow$
$\langle^2T_1, yz \uparrow $	$-\frac{1}{\sqrt{2}}xz \uparrow$	$-\frac{1}{2}xz \downarrow$	0
$\langle^2T_1, yz \downarrow $	0	$-\frac{1}{2}xz \uparrow$	$-\frac{1}{\sqrt{2}}xz \downarrow$

Table A.1.: Summary of single-site transition matrix elements from d^4 initial states with doubly occupied xy orbital to $|^4A_2\rangle$ and $|^2T_1\rangle$ d^3 multiplets, where $xy \downarrow$ stands for $c_{xy\downarrow}$.

	$ d^4 \uparrow\rangle$	$ d^4 0\rangle$	$ d^4 \downarrow\rangle$
$\langle d^5 xz \downarrow $	0	$-\frac{1}{\sqrt{2}}yz \downarrow$	$yz \uparrow$
$\langle d^5 xz \uparrow $	$-yz \downarrow$	$\frac{1}{\sqrt{2}}yz \uparrow$	0
$\langle d^5 yz \downarrow $	0	$\frac{1}{\sqrt{2}}xz \downarrow$	$-xz \uparrow$
$\langle d^5 yz \uparrow $	$xz \downarrow$	$-\frac{1}{\sqrt{2}}xz \uparrow$	0

Table A.2.: Summary of single-site transition matrix elements from d^4 initial states with doubly occupied xy orbital to all available d^5 states, where $xy \downarrow$ stands for $c_{xy\downarrow}^\dagger$.

Bibliography

- [1] A P Ramirez. Colossal magnetoresistance. In: *J. Phys. Condens. Matter*, **9**:39 (1997), 8171 (see p. 1).
- [2] Y. Tokura. Metal-insulator phenomena in perovskites of transition metal oxide. In: *Phys. B Condens. Matter*, **237-238**: (July 1997), 1–5. DOI: 10.1016/S0921-4526(97)00009-4 (see p. 1).
- [3] Masatoshi Imada, Atsushi Fujimori and Yoshinori Tokura. Metal-insulator transitions. In: *Rev. Mod. Phys.*, **70**:4 (Oct. 1998), 1039–1263. DOI: 10.1103/RevModPhys.70.1039 (see pp. 1, 80).
- [4] J. G. Bednorz and K. A. Müller. Possible highTc superconductivity in the BaLaCuO system. In: *Zeitschrift für Phys. B Condens. Matter*, **64**:2 (1986), 189–193. DOI: 10.1007/BF01303701 (see pp. 2, 45).
- [5] Elbio Dagotto. Complexity in strongly correlated electronic systems. In: *Science (80-.)*, **309**:5732 (July 2005), 257–62. DOI: 10.1126/science.1107559 (see pp. 2, 49).
- [6] Su-Yang Xu, Ilya Belopolski, Nasser Alidoust, Madhab Neupane, Guang Bian, Chenglong Zhang, Raman Sankar, Guoqing Chang, Zhujun Yuan, Chi-Cheng Lee, Shin-Ming Huang, Hao Zheng, Jie Ma, Daniel S Sanchez, BaoKai Wang, Arun Bansil, Fangcheng Chou, Pavel P Shibayev, Hsin Lin, Shuang Jia and M Zahid Hasan. Discovery of a Weyl fermion semimetal and topological Fermi arcs. In: *Science (80-.)*, **349**:6248 (2015), 613–617. DOI: 10.1126/science.aaa9297 (see p. 2).
- [7] Frank Wilczek. Majorana returns. In: *Nat Phys*, **5**:9 (Sept. 2009), 614–618 (see p. 2).
- [8] Yoshinori Tokura, Masashi Kawasaki and Naoto Nagaosa. Emergent functions of quantum materials. In: *Nat. Phys.*, **13**:11 (2017), 1056–1068. DOI: 10.1038/nphys4274 (see p. 2).

Bibliography

- [9] Jan M. Tomczak and Silke Biermann. Optical properties of correlated materials - Or why intelligent windows may look dirty. In: *Phys. Status Solidi*, **246**:9 (Sept. 2009), 1996–2005. DOI: 10.1002/pssb.200945231 (see p. 2).
- [10] J M Daughton. GMR applications. In: *J. Magn. Magn. Mater.*, **192**:2 (1999), 334–342. DOI: [http://dx.doi.org/10.1016/S0304-8853\(98\)00376-X](http://dx.doi.org/10.1016/S0304-8853(98)00376-X) (see p. 2).
- [11] Shigehiro Nishijima, Steven Eckroad, Adela Marian, Kyeongdal Choi, Woo Seok Kim, Motoaki Terai, Zigang Deng, Jun Zheng, Jiasu Wang, Katsuya Umemoto, Jia Du, Pascal Febvre, Shane Keenan, Oleg Mukhanov, Lance D. Cooley, Cathy P. Foley, William V. Hassenzahl and Mitsuru Izumi. Superconductivity and the environment: a Roadmap. In: *Supercond. Sci. Technol.*, **26**: (2013), 113001. DOI: 10.1088/0953-2048/26/11/113001 (see p. 2).
- [12] J C Séamus Davis and Dung-Hai Lee. Concepts relating magnetic interactions, intertwined electronic orders, and strongly correlated superconductivity. In: *Proc. Natl. Acad. Sci. U. S. A.*, (Oct. 2013), 1316512110–. DOI: 10.1073/pnas.1316512110 (see p. 3).
- [13] B Keimer, S A Kivelson, M R Norman, S Uchida and J Zaanen. From quantum matter to high-temperature superconductivity in copper oxides. In: *Nature*, **518**:7538 (2015), 179–86. DOI: 10.1038/nature14165 (see p. 3).
- [14] P Lemmens, G. Güntherodt and C. Gros. Magnetic light scattering in low-dimensional quantum spin systems. In: *Phys. Rep.*, **375**:1 (2003), 1–103. DOI: 10.1016/S0370-1573(02)00321-6 (see p. 4).
- [15] H Bethe. Zur Theorie der Metalle. I. Eigenwerte und Eigenfunktionen der linearen Atomkette. In: *Z. Phys. A*, **71**: (1931), 205–226 (see pp. 7, 47).
- [16] F Bloch. Bemerkung zur Elektronentheorie des Ferromagnetismus und der elektrischen Leitfähigkeit. In: *Zeitschrift für Phys.*, **57**:7 (1929), 545–555. DOI: 10.1007/BF01340281 (see p. 7).
- [17] A Sommerfeld. Zur Elektronentheorie der Metalle auf Grund der Fermischen Statistik. In: *Zeitschrift für Phys.*, **47**:1 (1928), 1–32. DOI: 10.1007/BF01391052 (see p. 7).
- [18] A H Wilson. The Theory of Electronic Semi-Conductors. In: *Proc. R. Soc. London A Math. Phys. Eng. Sci.*, **133**:822 (1931), 458–491. DOI: 10.1098/rspa.1931.0162 (see p. 7).

- [19] J H de Boer, E J W Verwey, Sommerfeld A H, Bethe, Brillouin L, Mott N F H, Jones, Wilson A H, Wilson A H, Fowler R H, Fowler R H, Bacher R F S, Goudsmit, Gorter C J, Le Blanc M H, Sachse, Gudden B, Wagner C, Wagner C, Verwey E J W H, de Boer J, Wagner C E, Koch, Schottky W, Jette E R F, Foote, Klemm W K, Hass, Dünwald H C, Wagner, Schottky W F, Waibel, Schriel M, Dünwald H v Baumbach H H, Wagner C, Hund F, de Boer J H Ch, van Geel W, Jusé W P W, Kurtschatow B, Bädeker K, de Boer J H, de Boer J H, Hägg G, Verwey E J W and de Boer J H. Semi-conductors with partially and with completely filled 3 d -lattice bands. In: *Proc. Phys. Soc.*, **49**:4S (1937), 59–71. DOI: 10.1088/0959-5309/49/4S/307 (see p. 7).
- [20] N. F. Mott and R. Peierls. Discussion of the paper by de Boer and Verwey. In: *Proc. Phys. Soc.*, **49**: (1937), 72–73. DOI: 10.1088/0959-5309/49/4S/308 (see p. 7).
- [21] E. J. W. Verwey. Electronic Conduction of Magnetite (Fe₃O₄) and its Transition Point at Low Temperatures. In: *Nature*, **144**:3642 (1939), 327–328. DOI: 10.1038/144327b0 (see pp. 7, 77, 78).
- [22] J D Thompson and J Willis. Heavy-Electron Metals : New Highly States of Matter Correlated. In: *Science (80-.)*, **297**:1986 (1987), 33–42. DOI: 10.1126/science.239.4835.33 (see p. 8).
- [23] Patrik Fazekas. *Lecture Notes on Electron Correlation and Magnetism*. First Edit. World Scientific Publishing, 1999 (see p. 8).
- [24] Daniel Khomskii. *Transition Metal Compounds*. Cambridge University Press, 2014 (see pp. 8, 81, 95).
- [25] N F Mott. The Basis of the Electron Theory of Metals, with Special Reference to the Transition Metals. In: *Proc. Phys. Soc. Sect. A*, **62**:7 (1949), 416 (see pp. 10, 11).
- [26] J Hubbard. Electron Correlations in Narrow Energy Bands. In: *Proc. R. Soc. London. Ser. A. Math. Phys. Sci.*, **276**:1365 (Nov. 1963), 238–257. DOI: 10.1098/rspa.1963.0204 (see pp. 10, 11).
- [27] J Zaanen, GA Sawatzky and JW Allen. Band gaps and electronic structure of transition-metal compounds. In: *Phys. Rev. Lett.*, (1985) (see p. 13).
- [28] William Witczak-Krempa, Gang Chen, Yong Baek Kim and Leon Balents. Correlated Quantum Phenomena in the Strong Spin-Orbit Regime. In: *Annu. Rev. Condens. Matter Phys.*, **5**:1 (2014), 57–82. DOI: 10.1146/annurev-conmatphys-020911-125138. arXiv: 1305.2193 (see p. 15).

Bibliography

- [29] D. Basov, Richard Averitt, Dirk van der Marel, Martin Dressel and Kristjan Haule. Electrodynamics of correlated electron materials. In: *Rev. Mod. Phys.*, **83**:2 (June 2011), 471–542. DOI: 10.1103/RevModPhys.83.471 (see p. 15).
- [30] S. Park, T. Ishikawa and Y. Tokura. *Charge-gap formation upon the Verwey transition in Fe₃O₄*. 1998. DOI: 10.1103/PhysRevB.58.3717 (see pp. 16, 79, 84–87, 92, 94–96, 136).
- [31] J. Reul, A. Nugroho, T. Palstra and M. Grüninger. Probing orbital fluctuations in RVO₃ (R = Y, Gd, or Ce) by ellipsometry. In: *Phys. Rev. B*, **86**:12 (Sept. 2012), 1–6. DOI: 10.1103/PhysRevB.86.125128 (see pp. 16, 18, 42, 87).
- [32] Martin Dressel and George Grüner. *Electrodynamics of Solids: Optical Properties of Electrons in Matter*. First. University Press, 2002 (see pp. 19, 20, 24, 25).
- [33] Hans Kuzmany. *Solid-State Spectroscopy: An Introduction*. first. Springer, 1998 (see pp. 20, 29).
- [34] Marco Windt. *Optical Spectroscopy of Spin Ladders*. PhD thesis. Universität zu Köln, 2002 (see pp. 20, 48, 52, 65).
- [35] Mark Fox. *Optical Properties of Solids*. Second. Oxford University Press, 2010 (see p. 20).
- [36] F Wooten. *Optical Properties of Solids*. Academic Press, 1972 (see p. 20).
- [37] D De Sousa Meneses, M Malki and P Echegut. Structure and lattice dynamics of binary lead silicate glasses investigated by infrared spectroscopy. In: *J. Non. Cryst. Solids*, **352**:8 (June 2006), 769–776. DOI: 10.1016/j.jnoncrysol.2006.02.004 (see p. 26).
- [38] G. E. Jellison and F. A. Modine. Parameterization of the optical functions of amorphous materials in the interband region. In: *Appl. Phys. Lett.*, **69**:3 (1996), 371. DOI: 10.1063/1.118064 (see p. 27).
- [39] R.J. Bell. *Introductory Fourier Transform Spectroscopy*. New York: Academic Press, 1972 (see p. 29).
- [40] P.R. Griffiths and J.A. de Haseth. *Fourier Transform Infrared Spectrometry*. New York: John Wiley & Sons, 1986 (see p. 29).
- [41] Eva Benckiser. *Optical Spectroscopy of Orbital and Magnetic Excitations in Vanadates and Cuprates*. PhD thesis. Universität zu Köln, 2007 (see p. 30).

- [42] Frederick Wooten. Reflectivity of uniaxial absorbing crystals. In: *Appl. Opt.*, **23**:23 (Dec. 1984), 4226–4227. DOI: 10.1364/AO.23.004226 (see p. 31).
- [43] Yukio Mizuno and Shoichiro Koide. Vibrationally induced electronic transitions in crystals of magnetic compounds - II. Spin-dependent infrared absorption band in NiO. In: *Phys. der Kondens. Mater.*, **2**:2 (1964), 166–179. DOI: 10.1007/BF02422874 (see p. 33).
- [44] J. Lorenzana and G. A. Sawatzky. Theory of phonon-assisted multi-magnon optical absorption and bimagnon states in quantum antiferromagnets. In: *Phys. Rev. B*, **52**:13 (Oct. 1995), 9576–9589. DOI: 10.1103/PhysRevB.52.9576 (see p. 33).
- [45] H. Suzuura, H. Yasuhara, A. Furusaki, N. Nagaosa and Y. Tokura. Singularities in Optical Spectra of Quantum Spin Chains. In: *Phys. Rev. Lett.*, **76**:14 (1996), 2579–2582. DOI: 10.1103/PhysRevLett.76.2579 (see pp. 33, 47, 48).
- [46] J. Lorenzana and R. Eder. Dynamics of the one-dimensional Heisenberg model and optical absorption of spinons in cuprate antiferromagnetic chains. In: *Phys. Rev. B*, **55**:6 (1997), R3358–R3361. DOI: 10.1103/physrevb.55.r3358. arXiv: 9608035 [cond-mat] (see pp. 33, 48, 49).
- [47] M Windt, M Grüninger, T Nunner, C Knetter, K P Schmidt, G S Uhrig, T Kopp, A Freimuth, U Ammerahl, B Büchner and A Revcolevschi. Observation of Two-Magnon Bound States in the Two-Leg Ladders of $(Ca, La)_{14}Cu_{24}O_{41}$. In: *Phys. Rev. Lett.*, **87**:12 (Aug. 2001), 127002. DOI: 10.1103/PhysRevLett.87.127002 (see pp. 33, 56, 57, 65, 66).
- [48] R.M.A Azzam and N.M Bashara. *Ellipsometry and Polarized Light*. First. North Holland, 1988 (see pp. 34, 41).
- [49] Harland Tompkins and Eugene A Irene. *Handbook of Ellipsometry*. First. William Andrew, 2006 (see pp. 34, 43).
- [50] Hiroyuki Fujiwara. *Spectroscopic Ellipsometry: Principles and Applications*. First. John Wiley and Sons, Ltd, 2007 (see pp. 34, 40, 43).
- [51] Alexander Gössling. *Electronic structure of Titanates and layered Manganites probed by optical spectroscopy*. PhD thesis. Universität zu Köln, 2007 (see pp. 36, 39).
- [52] D. E. Aspnes. Approximate solution of ellipsometric equations for optically biaxial crystals. In: *J. Opt. Soc. Am.*, **70**:10 (Oct. 1980), 1275. DOI: 10.1364/JOSA.70.001275 (see p. 37).

Bibliography

- [53] P W Anderson. The Resonating Valence Bond State in La_2CuO_4 and Superconductivity. In: *Science*, **235**:4793 (Mar. 1987), 1196–8. DOI: 10.1126/science.235.4793.1196 (see pp. 45, 46).
- [54] Danfeng Li, Kyuho Lee, Bai Yang Wang, Motoki Osada, Samuel Crossley, Hye Ryoung Lee, Yi Cui, Yasuyuki Hikita and Harold Y. Hwang. Superconductivity in an infinite-layer nickelate. In: *Nature*, **572**: (2019), pages624–627. DOI: <https://doi.org/10.1038/s41586-019-1496-5> (see p. 45).
- [55] E Dagotto, J Riera and D Scalapino. Superconductivity in ladders and coupled planes. In: *Phys. Rev. B*, **45**:10 (1992), 5744–5747. DOI: 10.1103/PhysRevB.45.5744 (see pp. 45, 46).
- [56] Efstratios Manousakis. The spin- Heisenberg antiferromagnet on a square lattice and its application to the cuprous oxides. In: *Rev. Mod. Phys.*, **63**:1 (1991), 1–62. DOI: 10.1103/RevModPhys.63.1 (see p. 46).
- [57] N D Mermin and H Wagner. Absence of Ferromagnetism or Antiferromagnetism in One- or Two-Dimensional Isotropic Heisenberg Models. In: *Phys. Rev. Lett.*, **17**:22 (Nov. 1966), 1133–1136. DOI: 10.1103/PhysRevLett.17.1133 (see p. 46).
- [58] Sudha Gopalan, T M Rice and M Sigrist. Spin ladders with spin gaps: A description of a class of cuprates. In: *Phys. Rev. B*, **49**:13 (Apr. 1994), 8901–8910. DOI: 10.1103/PhysRevB.49.8901 (see pp. 46, 50).
- [59] S R White, R M Noack and D J Scalapino. Resonating Valence Bond Theory of Coupled Heisenberg Chains. In: *Phys. Rev. Lett.*, **73**:6 (Aug. 1994), 886–889. DOI: 10.1103/PhysRevLett.73.886 (see pp. 46, 68).
- [60] Steven R White and D J Scalapino. Ground states of the doped four-leg t-J ladder. In: *Phys. Rev. B*, **55**:22 (June 1997), R14701–R14704. DOI: 10.1103/PhysRevB.55.R14701 (see p. 46).
- [61] M Greven, R J Birgeneau and U J Wiese. A Monte Carlo Study of Correlations in Quantum Spin Ladders. In: *Phys. Rev. Lett.*, **77**:9 (1996), 1865–1868 (see pp. 46, 68).
- [62] Y Fan and M Ma. Generating-function approach to the resonating-bond state on the triangular and square ladders. In: *Phys. Rev. B*, **37**:4 (Feb. 1988), 1820–1824. DOI: 10.1103/PhysRevB.37.1820 (see p. 46).
- [63] M. Roncaglia, G. Sierra and M.A. Martin-Delgado. Dimer-resonating valence bond state of the four-leg Heisenberg ladder: Interference among resonances. In: *Phys. Rev. B - Condens. Matter Mater. Phys.*, **60**:17 (1999), 134–137. DOI: 10.1103/PhysRevB.60.12134 (see p. 46).

- [64] J. Knolle and R. Moessner. A Field Guide to Spin Liquids. In: *Annual Review of Condensed Matter Physics*, **10**:1 (2019), 451–472. DOI: 10.1146/annurev-conmatphys-031218-013401. eprint: <https://doi.org/10.1146/annurev-conmatphys-031218-013401> (see p. 46).
- [65] L D Faddeev and L A Takhtajan. What is the spin of a spin wave? In: *Phys. Lett. A*, **85**:6 (1981), 375–377. DOI: [https://doi.org/10.1016/0375-9601\(81\)90335-2](https://doi.org/10.1016/0375-9601(81)90335-2) (see p. 47).
- [66] Jacques des Cloizeaux and J J Pearson. Spin-Wave Spectrum of the Antiferromagnetic Linear Chain. In: *Phys. Rev.*, **128**:5 (Dec. 1962), 2131–2135. DOI: 10.1103/PhysRev.128.2131 (see p. 48).
- [67] Martin Mourigal, Mechthild Enderle, Axel Klöpperpieper, Jean-Sébastien Caux, Anne Stunault and Henrik M. Rønnow. Fractional spinon excitations in the quantum Heisenberg antiferromagnetic chain. In: *Nat. Phys.*, **9**:7 (2013), 435–441. DOI: 10.1038/nphys2652. arXiv: 1306.4678 (see p. 48).
- [68] Z. Hiroi, M. Azuma, M. Takano and Y. Bando. A new homologous series $Sr_{n-1}Cu_{n+1}O_{2n}$ found in the SrO-CuO system treated under high pressure. In: *J. Solid State Chem.*, **95**:1 (1991), 230–238. DOI: 10.1016/0022-4596(91)90394-W (see p. 49).
- [69] M. Azuma, Z. Hiroi, M. Takano, K. Ishida and Y. Kitaoka. Observation of a spin gap in SrCu₂O₃ comprising spin-Quasi-1D two-leg ladders. In: *Phys. Rev. Lett.*, **73**:25 (1994), 3463–3466. DOI: 10.1103/PhysRevLett.73.3463 (see pp. 49–51).
- [70] E. Dagotto and T. M. Rice. Surprises on the Way from 1D to 2D Quantum Magnets: the Novel Ladder Materials. In: *Science (80-.)*, **271**:5249 (1996), 18. DOI: 10.1126/science.271.5249.618. arXiv: 9509181 [cond-mat] (see p. 50).
- [71] M. Uehara, T. Nagata, J. Akimitsu, H. Takahashi, N. Môri and K. Kinoshita. Superconductivity in the Ladder Material $Sr_{0.4}Ca_{13.6}Cu_{24}O_{41.84}$. In: *J. Phys. Soc. Japan*, **65**:9 (1996), 2764–2767. DOI: 10.1143/JPSJ.65.2764 (see p. 50).
- [72] C. Knetter, K. P. Schmidt, M. Grüninger and G. S. Uhrig. Fractional and Integer Excitations in Quantum Antiferromagnetic Spin 1/2 Ladders. In: *Phys. Rev. Lett.*, **87**:16 (Oct. 2001), 167204. DOI: 10.1103/PhysRevLett.87.167204 (see pp. 51, 52, 54, 55).

Bibliography

- [73] D.C. Johnston, M Troyer, S Miyahara, D Lidsky, K Ueda, M Azuma, Z Hiroi, M Takano, M Isobe, Y Ueda, M.A. Korotin, V.I. Anisimov, A.V. Mahajan and L.L. Miller. Magnetic Susceptibilities of Spin-1/2 Antiferromagnetic Heisenberg Ladders and Applications to Ladder Oxide Compounds. In: *eprint arXiv:cond-mat/0001147*, (2000) (see p. 53).
- [74] S. Notbohm, P Ribeiro, B. Lake, D. Tennant, K. Schmidt, G. Uhrig, C. Hess, R. Klingeler, G. Behr, B. Büchner, M. Reehuis, R. Bewley, C. Frost, P. Manuel and R. Eccleston. One- and Two-Triplon Spectra of a Cuprate Ladder. In: *Phys. Rev. Lett.*, **98**:2 (Jan. 2007), 027403. DOI: 10.1103/PhysRevLett.98.027403 (see pp. 52, 53, 57).
- [75] Tamara S Nunner, Philipp Brune, Thilo Kopp, Marco Windt and Markus Grüninger. Cyclic spin exchange in cuprate spin ladders. In: *Phys. Rev. B*, **66**:18 (2002), 180404+. DOI: 10.1103/PhysRevB.66.180404. arXiv: 0203472v1 [arXiv:cond-mat] (see pp. 52, 56, 57, 75).
- [76] O. Sushkov and V. Kotov. Bound States of Magnons in the $S=1/2$ Quantum Spin Ladder. In: *Phys. Rev. Lett.*, **81**:9 (1998), 1941–1944. DOI: 10.1103/PhysRevLett.81.1941. arXiv: 9803180 [cond-mat] (see pp. 52, 54).
- [77] Weihong Zheng, Chris J Hamer, Rajiv R P Singh, Simon Trebst and Hartmut Monien. Linked cluster series expansions for two-particle bound states. In: *Phys. Rev. B*, **63**:14 (Mar. 2001), 144410. DOI: 10.1103/PhysRevB.63.144410 (see p. 52).
- [78] D G Shelton, A A Nersesyan and A M Tsvelik. Antiferromagnetic spin ladders: Crossover between spin $S=1/2$ and $S=1$ chains. In: *Phys. Rev. B*, **53**:13 (Apr. 1996), 8521–8532. DOI: 10.1103/PhysRevB.53.8521 (see p. 52).
- [79] J Lorenzana, J Eroles and S Sorella. Does the Heisenberg model describe the multimagnon spin dynamics in antiferromagnetic CuO layers? In: *Phys. Rev. Lett.*, **83**:24 (1999), 13–16. DOI: 10.1103/PhysRevLett.83.5122. arXiv: 9911037 [cond-mat] (see pp. 57, 58).
- [80] Chang-Ming Ho, V. N. Muthukumar, Masao Ogata and P. W. Anderson. Nature of Spin Excitations in Two-Dimensional Mott Insulators: Undoped Cuprates and Other Materials. In: *Phys. Rev. Lett.*, **86**: (8 Feb. 2001), 1626–1629. DOI: 10.1103/PhysRevLett.86.1626 (see p. 58).

- [81] Markus Grüninger, Marco Windt, Eva Benckiser, Tamara S Nunner, Kai P Schmidt, Götz S Uhrig and Thilo Kopp. *Optical Spectroscopy of Low-Dimensional Quantum Spin Systems*. In: *Adv. Solid State Phys.* Ed. by Bernhard Kramer. Berlin, Heidelberg: Springer Berlin Heidelberg, 2003, 95–112. DOI: 10.1007/978-3-540-44838-9_7 (see pp. 58, 73).
- [82] J. D. Perkins, J. M. Graybeal, M. A. Kastner, R. J. Birgeneau, J. P. Falck and M. Greven. Mid-infrared optical absorption in undoped lamellar copper oxides. In: *Phys. Rev. Lett.*, **71**:10 (1993), 1621–1624. DOI: 10.1103/PhysRevLett.71.1621 (see p. 59).
- [83] J. D. Perkins, D. S. Kleinberg, M. A. Kastner, R. J. Birgeneau, Y. Endoh, K. Yamada and S. Hosoya. Infrared optical excitations in La₂NiO₄. In: *Phys. Rev. B*, **52**:14 (1995), 9863–9866. DOI: 10.1103/PhysRevB.52.R9863 (see p. 59).
- [84] M. Grüninger, D. Van der Marel, A. Damascelli, A. Erb, T. Nunner and T. Kopp. Midinfrared absorption in YBa₂Cu₃O₆: Evidence for a failure of spin-wave theory for spin 1/2 in two dimensions. In: *Phys. Rev. B - Condens. Matter Mater. Phys.*, **62**:18 (2000), 12422–12426. DOI: 10.1103/PhysRevB.62.12422 (see p. 59).
- [85] R. J. Cava, T. Siegrist, B. Hessen, J. J. Krajewski, W. F. Peck, B. Batlogg, H. Takagi, J. V. Waszczak, L. F. Schneemeyer and H. W. Zandbergen. A new type of homologous series in the La-Cu-O system. In: *Phys. C Supercond. its Appl.*, **177**:1-3 (1991), 115–121. DOI: 10.1016/0921-4534(91)90306-J (see pp. 59, 61, 62).
- [86] C. Sekar, T. Watanabe and A. Matsuda. Crystal growth and characterization of the 4-leg spin ladder compound La₂Cu₂O₅. In: *J. Cryst. Growth*, **212**:1 (2000), 142–147. DOI: 10.1016/S0022-0248(00)00009-9 (see pp. 59, 62).
- [87] R. J. Cava, T. Siegrist, B. Hessen, J. J. Krajewski, W. F. Peck, B. Batlogg, H. Takagi, J. V. Waszczak, L. F. Schneemeyer and H. W. Zandbergen. A new homologous series of lanthanum copper oxides. In: *J. Solid State Chem.*, **94**:1 (1991), 170–184. DOI: 10.1016/0022-4596(91)90230-F (see pp. 60–62).
- [88] I V Golosovsky, A G Gukasov, V A Polyakov, D I Zhigunov and I A Zabolko. Magnetic structure of lanthanum copper oxide La₂Cu₂O₅. In: *J. Phys. Condens. Matter*, **11**:36 (1999), 6959 (see p. 62).

Bibliography

- [89] M. Grüninger, M. Windt, T. Nunner, C. Knetter, K. P Schmidt, G. S. Uhrig, T. Kopp, A. Freimuth, U. Ammerahl, B. Büchner and A. Revcolevschi. Magnetic excitations in two-leg spin 1/2 ladders: Experiment and theory. In: *J. Phys. Chem. Solids*, **63**:12 (2002), 2167–2173. DOI: 10.1016/S0022-3697(02)00251-2. arXiv: 0109524 [cond-mat] (see p. 63).
- [90] Kris Cöster. *Series expansions for dimerized quantum spin systems*. Diplom. TU Dortmund, 2011 (see pp. 66, 69, 71, 72).
- [91] Kai P. Schmidt. ‘Private communication’ (see p. 66).
- [92] Stefan Wessel. ‘Private communication’ (see p. 66).
- [93] Tamara S Nunner. *Spin Excitations in Low Dimensional Quantum Antiferromagnets*. PhD thesis. Universität Augsburg, 2003 (see pp. 67, 68).
- [94] C. Knetter and G. S. Uhrig. Perturbation theory by flow equations : dimerized and frustrated $S = 1/2$ chain. In: *Eur. Phys. J. B*, **225**:13 (2000), 209–225. DOI: 10.1007/s100510050026. arXiv: 9906243v1 [arXiv:cond-mat] (see p. 69).
- [95] W Eerenstein, T T M Palstra, S S Saxena and T Hibma. Spin-polarized transport across sharp antiferromagnetic boundaries. In: *Phys. Rev. Lett.*, **88**:24 (2002), 247204. DOI: 10.1103/PhysRevLett.88.247204 (see p. 77).
- [96] K. M. Reddy, Nitin P. Padture, Alex Punnoose and Charles Hanna. Heterojunction metal-oxide-metal Au-Fe₃O₄-Au single nanowire device for spintronics. In: *J. Appl. Phys.*, **117**:17 (2015), 17D710. DOI: 10.1063/1.4913891 (see p. 77).
- [97] Sönke Johnsen and Kenneth J Lohmann. The physics and neurobiology of magnetoreception. In: *Nat. Rev. Neurosci.*, **6**:9 (2005), 703–712. DOI: 10.1038/nrn1745 (see p. 77).
- [98] J Ebad-Allah, L Baldassarre, M Sing, R Claessen, V a M Brabers and C a Kuntscher. Polaron physics and crossover transition in magnetite probed by pressure-dependent infrared spectroscopy. In: *J. Phys. Condens. Matter*, **25**:3 (2013), 035602. DOI: 10.1088/0953-8984/25/3/035602. arXiv: arXiv:1202.4431v2 (see pp. 78, 80).
- [99] L R Bickford. The Low Temperature Transformation in Ferrites. In: *Rev. Mod. Phys.*, **25**:1 (Jan. 1953), 75–79. DOI: 10.1103/RevModPhys.25.75 (see p. 77).

- [100] J P Shepherd, J W Koenitzer, R Aragón, J Spal/ek and J M Honig. Heat capacity and entropy of nonstoichiometric magnetite $Fe_{3(1-\delta)}O_4$: The thermodynamic nature of the Verwey transition. In: *Phys. Rev. B*, **43**:10 (Apr. 1991), 8461–8471. DOI: 10.1103/PhysRevB.43.8461 (see p. 77).
- [101] Özden Özdemir, David J Dunlop and Bruce M Moskowitz. Changes in remanence, coercivity and domain state at low temperature in magnetite. In: *Earth Planet. Sci. Lett.*, **194**:34 (2002), 343–358. DOI: [http://dx.doi.org/10.1016/S0012-821X\(01\)00562-3](http://dx.doi.org/10.1016/S0012-821X(01)00562-3) (see p. 77).
- [102] Ming Liu, Jason Hoffman, Jing Wang, Jinxing Zhang, Brittany Nelson-Cheeseman and Anand Bhattacharya. Non-volatile ferroelastic switching of the Verwey transition and resistivity of epitaxial $Fe_3O_4/PMN-PT$ (011). In: *Sci. Rep.*, **3**:001 (2013), 1876. DOI: 10.1038/srep01876 (see p. 77).
- [103] Indira Chaitanya Lekshmi, Raffaella Buonsanti, Concetta Nobile, Ross Rinaldi, Pantaleo Davide Cozzoli and Giuseppe Maruccio. Tunneling Magnetoresistance with Sign Inversion in Junctions Based on Iron Oxide Nanocrystal Superlattices. In: *ACS Nano*, **5**:3 (2011), 1731–1738. DOI: 10.1021/nn102301y (see p. 77).
- [104] R Ramos, T Kikkawa, K Uchida, H Adachi, I Lucas, M H Aguirre, P Algarabel, L Morellón, S Maekawa, E Saitoh and M R Ibarra. Observation of the spin Seebeck effect in epitaxial Fe_3O_4 thin films. In: *Appl. Phys. Lett.*, **102**:7 (2013), 72413. DOI: 10.1063/1.4793486 (see p. 77).
- [105] Friedrich Walz. The Verwey transition - a topical review. In: *J. Phys. Condens. Matter*, **14**:12 (2002), R285–R340. DOI: 10.1088/0953-8984/14/12/203. arXiv: S0953-8984(02)19767-0 (see p. 78).
- [106] M Iizumi, T F Koetzle, G Shirane, S Chikazumi, M Matsui and S Todo. Structure of magnetite (Fe_3O_4) below the Verwey transition temperature. In: *Acta Crystallogr. Sect. B*, **38**:8 (Aug. 1982), 2121–2133. DOI: 10.1107/S0567740882008176 (see pp. 78, 82).
- [107] J P Wright, J P Attfield and P G Radaelli. Long Range Charge Ordering in Magnetite Below the Verwey Transition. In: *Phys. Rev. Lett.*, **87**:26 (2001), 266401. DOI: 10.1103/PhysRevLett.87.266401 (see p. 78).
- [108] E Nazarenko, J E Lorenzo, Y Joly, J L Hodeau, D Mannix and C Marin. Resonant X-Ray Diffraction Studies on the Charge Ordering in Magnetite. In: *Phys. Rev. Lett.*, **97**:5 (Aug. 2006), 56403. DOI: 10.1103/PhysRevLett.97.056403 (see p. 78).

Bibliography

- [109] J. E. Lorenzo, C. Mazzoli, N. Jaouen, C. Detlefs, D. Mannix, S. Grenier, Y. Joly and C. Marin. Charge and orbital correlations at and above the Verwey phase transition in magnetite. In: *Phys. Rev. Lett.*, **101**:22 (2008), 1–4. DOI: 10.1103/PhysRevLett.101.226401 (see p. 78).
- [110] Javier Blasco, Joaquín García and Gloria Subías. Structural transformation in magnetite below the Verwey transition. In: *Phys. Rev. B*, **83**:10 (Mar. 2011), 104105. DOI: 10.1103/PhysRevB.83.104105 (see p. 78).
- [111] A. Tanaka, C. F. Chang, M. Buchholz, C. Trabant, E. Schierle, J. Schlappa, D. Schmitz, H. Ott, P. Metcalf, L. H. Tjeng and C. Schüßler-Langeheine. Symmetry of orbital order in Fe₃O₄ studied by Fe L_{2,3} resonant X-ray diffraction. In: *Phys. Rev. Lett.*, **108**:22 (2012), 1–5. DOI: 10.1103/PhysRevLett.108.227203 (see p. 78).
- [112] Y Fujii, G Shirane and Y Yamada. Study of the 123-K phase transition of magnetite by critical neutron scattering. In: *Phys. Rev. B*, **11**:5 (Mar. 1975), 2036–2041. DOI: 10.1103/PhysRevB.11.2036 (see p. 78).
- [113] S M Shapiro, M Iizumi and G Shirane. Neutron scattering study of the diffuse critical scattering associated with the Verwey transition in magnetite Fe₃O₄. In: *Phys. Rev. B*, **14**:1 (July 1976), 200–207. DOI: 10.1103/PhysRevB.14.200 (see p. 78).
- [114] Shih-Chang Weng, Yen-Ru Lee, Cheng-Gang Chen, Chia-Hung Chu, Yun-Liang Soo and Shih-Lin Chang. Direct Observation of Charge Ordering in Magnetite Using Resonant Multiwave X-Ray Diffraction. In: *Phys. Rev. Lett.*, **108**:14 (2012), 1–4. DOI: 10.1103/PhysRevLett.108.146404 (see p. 78).
- [115] Mark S Senn, Jon P Wright and J Paul Attfield. Charge order and three-site distortions in the Verwey structure of magnetite. In: *Nature*, **481**:7380 (Jan. 2012), 173–176 (see pp. 78, 79, 82).
- [116] Mark S. Senn, Ingo Loa, Jon P. Wright and J. Paul Attfield. Electronic orders in the Verwey structure of magnetite. In: *Phys. Rev. B - Condens. Matter Mater. Phys.*, **85**:12 (2012), 1–5. DOI: 10.1103/PhysRevB.85.125119. arXiv: arXiv:1201.5106v2 (see pp. 79, 81–83).
- [117] Paolo G Radaelli, Y Horibe, Matthias J Gutmann, Hiroki Ishibashi, C H Chen, Richard M Ibberson, Y Koyama, Yew-San Hor, Valery Kiryukhin and Sang-Wook Cheong. Formation of isomorphous Ir³⁺ and Ir⁴⁺ octamers and spin dimerization in the spinel CuIr₂S₄. In: *Nature*, **416**:6877 (Mar. 2002), 155–158 (see p. 79).

- [118] M Schmidt, W Ratcliff, P G Radaelli, K Refson, N M Harrison and S W Cheong. Spin Singlet Formation in $MgTi_2O_4$: Evidence of a Helical Dimerization Pattern. In: *Phys. Rev. Lett.*, **92**:5 (Feb. 2004), 56402. DOI: 10.1103/PhysRevLett.92.056402 (see p. 79).
- [119] L. V. Gasparov, D. B. Tanner, D. B. Romero, H. Berger, G. Margaritondo and L. Forró. Infrared and Raman studies of the Verwey transition in magnetite. In: *Phys. Rev. B - Condens. Matter Mater. Phys.*, **62**:12 (2000), 7939–7944. DOI: 10.1103/PhysRevB.62.7939. arXiv: 9905278 [cond-mat] (see pp. 79, 84, 85, 87, 92, 94–96, 136).
- [121] N C Tombs and H P Rooksby. Structure transition and antiferromagnetism in magnetite. In: *Acta Crystallogr.*, **4**:5 (Sept. 1951), 474–475. DOI: 10.1107/S0365110X51001549 (see p. 79).
- [122] G. A. Samara and A. A. Giardini. Effect of Pressure on the Néel Temperature of Magnetite. In: *Phys. Rev.*, **186**: (2 Oct. 1969), 577–580. DOI: 10.1103/PhysRev.186.577 (see p. 80).
- [123] E J Verwey, P W Haayman and F C Romeijn. Physical Properties and Cation Arrangement of Oxides with Spinel Structures II. Electronic Conductivity. In: *J. Chem. Phys.*, **15**:4 (1947) (see p. 80).
- [124] P W Anderson. Ordering and Antiferromagnetism in Ferrites. In: *Phys. Rev.*, **102**:4 (1956), 1008–1013. DOI: 10.1103/PhysRev.102.1008 (see p. 81).
- [125] E J Samuelsen, E J Bleeker, L Dobrzynski and T Riste. Neutron Scattering from Magnetite below 119 K. In: *J. Appl. Phys.*, **39**:2 (1968) (see p. 81).
- [126] Jon P Wright, J Paul Attfield and Paolo G Radaelli. Charge ordered structure of magnetite Fe_3O_4 below the Verwey transition. In: *Phys. Rev. B*, **66**:21 (2002), 214422. DOI: 10.1103/PhysRevB.66.214422 (see pp. 81, 82).
- [127] Takeshi Kasama, Nathan S Church, Joshua M Feinberg, Rafal E Dunin-Borkowski and Richard J Harrison. Direct observation of ferrimagnetic/ferroelastic domain interactions in magnetite below the Verwey transition. In: *Earth Planet. Sci. Lett.*, **297**:12 (2010), 10–17. DOI: <http://dx.doi.org/10.1016/j.epsl.2010.05.004> (see p. 82).
- [128] Horng Tay Jeng, G. Y. Guo and D. J. Huang. Charge-orbital ordering in low-temperature structures of magnetite: GGA+U investigations. In: *Phys. Rev. B - Condens. Matter Mater. Phys.*, **74**:19 (2006), 1–10. DOI: 10.1103/PhysRevB.74.195115 (see p. 82).

Bibliography

- [129] Kunihiko Yamauchi, Tetsuya Fukushima and Silvia Picozzi. Ferroelectricity in multiferroic magnetite Fe_3O_4 driven by noncentrosymmetric Fe^{2+}/Fe^{3+} charge-ordering: First-principles study. In: *Phys. Rev. B*, **79**:21 (June 2009), 212404. DOI: 10.1103/PhysRevB.79.212404 (see p. 82).
- [130] I. Leonov, a. N. Yaresko, V. N. Antonov and V. I. Anisimov. Electronic structure of charge-ordered Fe_3O_4 from calculated optical, magneto-optical Kerr effect, and O K-edge x-ray absorption spectra. In: *Phys. Rev. B*, **74**:16 (2006), 32. DOI: 10.1103/PhysRevB.74.165117. arXiv: 0607187 [cond-mat] (see pp. 82, 83, 94–96).
- [131] Jeroen van den Brink and Daniel I Khomskii. Multiferroicity due to charge ordering. In: *J. Phys. Condens. Matter*, **20**:43 (2008), 434217 (see p. 82).
- [132] W. Fontijn, P. van der Zaag, M. Devillers, V. Brabers and R. Metselaar. Optical and magneto-optical polar Kerr spectra of Fe_3O_4 and Mg^{2+} - or Al^{3+} -substituted Fe_3O_4 . In: *Phys. Rev. B*, **56**:9 (1997), 5432–5442. DOI: 10.1103/PhysRevB.56.5432 (see pp. 84, 85, 87, 88, 96).
- [133] A Schlegel, S F Alvarado and P Wachter. Optical properties of magnetite (Fe_3O_4). In: *J. Phys. C Solid ...*, **12**: (1979), 1157. DOI: 10.1080/01418638008221885 (see pp. 84, 96).
- [134] S de Jong, R Kukreja, C Trabant, N Pontius, C F Chang, T Kachel, M Beye, F Sorgenfrei, C H Back, B Bräuer, W F Schlotter, J J Turner, O Krupin, M Doehler, D Zhu, M a Hossain, a O Scherz, D Fausti, F Novelli, M Esposito, W S Lee, Y D Chuang, D H Lu, R G Moore, M Yi, M Trigo, P Kirchmann, L Pathey, M S Golden, M Buchholz, P Metcalf, F Parmigiani, W Wurth, a Föhlich, C Schüssler-Langeheine and H a Dürr. Speed limit of the insulator-metal transition in magnetite. In: *Nat. Mater.*, **12**:10 (2013), 882–6. DOI: 10.1038/nmat3718 (see p. 85).
- [135] J. Reul, L. Fels, N. Qureshi, K. Shportko, M. Braden and M. Grüninger. Temperature-dependent optical conductivity of layered $LaSrFeO_4$. In: *Phys. Rev. B - Condens. Matter Mater. Phys.*, **87**:20 (2013), 2–9. DOI: 10.1103/PhysRevB.87.205142 (see pp. 87, 94, 121).
- [136] S. Nakatsuji and Y. Maeno. Quasi-Two-Dimensional Mott Transition System $Ca_{2-x}Sr_xRuO_4$. In: *Phys. Rev. Lett.*, **84**:12 (2000), 2666–2669. DOI: 10.1103/PhysRevLett.84.2666. arXiv: arXiv:1011.1669v3 (see p. 99).
- [137] Y Maeno, H Hashimoto, K Yoshida, S Nishizaki, T Fujita, J G Bednorz and F Lichtenberg. Superconductivity in a layered perovskite without copper. In: *Nature*, **372**:6506 (Dec. 1994), 532–534 (see p. 99).

- [138] Shuji Nishizaki, Yoshiteru Maeno and Toshizo Fujita. Effect of Annealing on the Superconductivity of Sr₂RuO₄. In: *J. Phys. Soc. Japan*, **65**:6 (1996), 1876–1877. DOI: 10.1143/JPSJ.65.1876 (see p. 99).
- [139] Satoru Nakatsuji, Shin-ichi Ikeda and Yoshiteru Maeno. Ca₂RuO₄: New Mott Insulators of Layered Ruthenate. In: *J. Phys. Soc. Japan*, **66**:7 (1997), 1868–1871. DOI: 10.1143/JPSJ.66.1868 (see pp. 99, 100).
- [140] C. Alexander, G. Cao, V. Dobrosavljevic, S. McCall, J. Crow, E. Lochner and R. Guertin. Destruction of the Mott insulating ground state of Ca₂RuO₄ by a structural transition. In: *Phys. Rev. B*, **60**:12 (1999), R8422–R8425. DOI: 10.1103/PhysRevB.60.R8422. arXiv: 9908390 [cond-mat] (see pp. 99, 101).
- [141] Takashi Hotta and Elbio Dagotto. Prediction of orbital ordering in single-layered ruthenates. In: *Phys. Rev. Lett.*, **88**:1 (2002), 017201. DOI: 10.1103/PhysRevLett.88.017201. arXiv: 0108531 [cond-mat] (see p. 99).
- [142] Fumihiko Nakamura, Mariko Sakaki, Yuya Yamanaka, Sho Tamaru, Takashi Suzuki and Yoshiteru Maeno. Electric-field-induced metal maintained by current of the Mott insulator Ca₂RuO₄. In: *Scientific Reports*, **3**: (2013), 2536. DOI: 10.1038/srep02536 (see p. 99).
- [143] Ryuji Okazaki, Yasuo Nishina, Yukio Yasui, Fumihiko Nakamura, Takashi Suzuki and Ichiro Terasaki. Current-Induced Gap Suppression in the Mott Insulator Ca₂RuO₄. In: *Journal of the Physical Society of Japan*, **82**:10 (2013), 103702. DOI: 10.7566/JPSJ.82.103702. eprint: <https://doi.org/10.7566/JPSJ.82.103702> (see p. 99).
- [144] Jiawei Zhang, Alexander S. McLeod, Qiang Han, Xinzhong Chen, Hans A. Bechtel, Ziheng Yao, S. N. Gilbert Corder, Thomas Ciavatti, Tiger H. Tao, Meigan Aronson, G. L. Carr, Michael C. Martin, Chanchal Sow, Shingo Yonezawa, Fumihiko Nakamura, Ichiro Terasaki, D. N. Basov, Andrew J. Millis, Yoshiteru Maeno and Mengkun Liu. Nano-Resolved Current-Induced Insulator-Metal Transition in the Mott Insulator Ca₂RuO₄. In: *Phys. Rev. X*, **9**: (1 Feb. 2019), 011032. DOI: 10.1103/PhysRevX.9.011032 (see p. 99).
- [145] K. Jenni, F. Wirth, K. Dietrich, L. Berger, Y. Sidis, S. Kunkemöller, C. P. Grams, D. I. Khomskii, J. Hemberger and M. Braden. Evidence for current-induced phase coexistence in Ca₂RuO₄ and its influence on magnetic order. In: *Phys. Rev. Materials*, **4**: (8 Aug. 2020), 085001. DOI: 10.1103/PhysRevMaterials.4.085001 (see p. 99).

Bibliography

- [146] S. Nakatsuji and Y. Maeno. Switching of magnetic coupling by a structural symmetry change near the Mott transition in $\text{Ca}_{2-x}\text{Sr}_x\text{RuO}_4$. In: *Phys. Rev. B*, **62**: (10 Sept. 2000), 6458–6466. DOI: 10.1103/PhysRevB.62.6458 (see p. 99).
- [147] O. Friedt, M. Braden, G. André, P. Adelman, S. Nakatsuji and Y. Maeno. Structural and magnetic aspects of the metal-insulator transition in $\text{Ca}_{2-x}\text{Sr}_x\text{RuO}_4$. In: *Phys. Rev. B*, **63**:17 (Apr. 2001), 174432. DOI: 10.1103/PhysRevB.63.174432 (see pp. 99–103).
- [148] S. Nakatsuji, D. Hall, L. Balicas, Z. Fisk, K. Sugahara, M. Yoshioka and Y. Maeno. Heavy-Mass Fermi Liquid near a Ferromagnetic Instability in Layered Ruthenates. In: *Phys. Rev. Lett.*, **90**: (13 Apr. 2003), 137202. DOI: 10.1103/PhysRevLett.90.137202 (see p. 99).
- [149] S. Nakatsuji, V. Dobrosavljevi, D. Tanaskovi, M. Minakata, H. Fukazawa and Y. Maeno. Mechanism of Hopping Transport in Disordered Mott Insulators. In: *Phys. Rev. Lett.*, **93**: (14 Sept. 2004), 146401. DOI: 10.1103/PhysRevLett.93.146401 (see p. 99).
- [150] J. P. Carlo, T. Goko, I. M. Gat-Malureanu, P. L. Russo, A. T. Savici, A. A. Aczel, G. J. MacDougall, J. A. Rodriguez, T. J. Williams, G. M. Luke, C. R. Wiebe, Y. Yoshida, S. Nakatsuji, Y. Maeno, T. Taniguchi and Y. J. Uemura. New magnetic phase diagram of $(\text{Sr,Ca})_2\text{RuO}_4$. English (US). In: *Nature Materials*, **11**:4 (Apr. 2012). Funding Information: This work has been supported by the US National Science Foundation (NSF) under the Materials World Network (MWN: DMR-0502706 and 0806846), the Partnership for International Research and Education (PIRE: OISE-0968226) and DMR-1105961 programs at Columbia, by the Canadian Natural Sciences and Engineering Research Council (NSERC) and the Canadian Institute for Advanced Research (CIFAR) at McMaster, and by Grants-in-Aid (No. 21684019) from the Japan Society for the Promotion of Science (JSPS) and (No. 19052003) for Scientific Research on Priority Areas (SRPA) from the Ministry of Education, Culture, Sports, Science and Technology (MEXT) at Kyoto and Tokyo Universities, and by MEXT-SRPA (No. 19052006) at Osaka University., 323–328. DOI: 10.1038/nmat3236 (see p. 99).
- [151] Z Fang and K Terakura. Magnetic phase diagram of $\text{Ca}_{2-x}\text{Sr}_x\text{RuO}_4$ governed by structural distortions. In: *Phys. Rev. B*, **64**:2 (June 2001), 20509. DOI: 10.1103/PhysRevB.64.020509 (see p. 99).

- [152] T. Mizokawa, L. H. Tjeng, G. A. Sawatzky, G. Ghiringhelli, O. Tjernberg, N. B. Brookes, H. Fukazawa, S. Nakatsuji and Y. Maeno. Spin-Orbit Coupling in the Mott Insulator Ca_2RuO_4 . In: *Phys. Rev. Lett.*, **87**:7 (2001), 077202. DOI: 10.1103/PhysRevLett.87.077202 (see pp. 99, 105, 106).
- [153] J S Lee, Y S Lee, T W Noh, S.-J. Oh, Jaejun Yu, S Nakatsuji, H Fukazawa and Y Maeno. Electron and Orbital Correlations in $Ca_{2-x}Sr_xRuO_4$ Probed by Optical Spectroscopy. In: *Phys. Rev. Lett.*, **89**:25 (2002), 257402. DOI: 10.1103/PhysRevLett.89.257402 (see pp. 99, 109–111, 118, 121, 123, 125, 134).
- [154] V I Anisimov, I A Nekrasov, D E Kondakov, T M Rice and M Sigrist. Orbital-selective Mott-insulator transition in $Ca_{2-x}Sr_xRuO_4$. In: *Eur. Phys. J. B - Condens. Matter Complex Syst.*, **25**:2 (2002), 191–201. DOI: 10.1140/epjb/e20020021 (see p. 99).
- [155] J H Jung, Z Fang, J P He, Y Kaneko, Y Okimoto and Y Tokura. Change of Electronic Structure in Ca_2RuO_4 Induced by Orbital Ordering. In: *Phys. Rev. Lett.*, **91**:5 (July 2003), 56403. DOI: 10.1103/PhysRevLett.91.056403 (see pp. 99, 104, 106–109, 111–113, 118, 121, 123).
- [156] Zhong Fang, Naoto Nagaosa and Kiyoyuki Terakura. Orbital-dependent phase control in $Ca_{2-x}Sr_xRuO_4$ $0 < x < 0.5$. In: *Phys. Rev. B*, **69**:4 (2004), 045116. DOI: 10.1103/PhysRevB.69.045116 (see pp. 99, 105, 106, 111, 112).
- [157] Antoine Georges, Luca de'Medici and Jernej Mravlje. Strong Correlations from Hund's Coupling. In: *Annu. Rev. Condens. Matter Phys.*, **4**:1 (2013), 137–178. DOI: 10.1146/annurev-conmatphys-020911-125045. arXiv: 1207.3033 (see p. 100).
- [158] B. J. Kim, Hosub Jin, S. J. Moon, J.-Y. Kim, B.-G. Park, C. S. Leem, Jaejun Yu, T. W. Noh, C. Kim, S.-J. Oh, J.-H. Park, V. Durairaj, G. Cao and E. Rotenberg. Novel $J_{eff} = 1/2$ Mott State Induced by Relativistic Spin-Orbit Coupling in Sr_2IrO_4 . In: *Phys. Rev. Lett.*, **101**:7 (Aug. 2008), 076402. DOI: 10.1103/PhysRevLett.101.076402. arXiv: 0803.2927 (see p. 100).
- [159] Fa Wang and T Senthil. Twisted Hubbard Model for Sr_2IrO_4 : Magnetism and Possible High Temperature Superconductivity. In: *Phys. Rev. Lett.*, **106**:13 (2011), 136402. DOI: 10.1103/PhysRevLett.106.136402 (see p. 100).

Bibliography

- [160] Arnab Banerjee, Jiaqiang Yan, Johannes Knolle, Craig A. Bridges, Matthew B. Stone, Mark D. Lumsden, David G. Mandrus, David A. Tennant, Roderich Moessner and Stephen E. Nagler. Neutron scattering in the proximate quantum spin liquid -RuCl_3 . In: *Science*, **356**:6342 (2017), 1055–1059. DOI: 10.1126/science.aah6015. eprint: <https://science.sciencemag.org/content/356/6342/1055.full.pdf> (see p. 100).
- [161] Giniyat Khaliullin. Excitonic Magnetism in Van Vleck–type d^4 Mott Insulators. In: *Phys. Rev. Lett.*, **111**:19 (Nov. 2013), 197201. DOI: 10.1103/PhysRevLett.111.197201. arXiv: arXiv:1310.0767v2 (see pp. 100, 105).
- [162] Alireza Akbari and Giniyat Khaliullin. Magnetic Excitations in Spin-Orbit Coupled d^4 Mott Insulator on Square Lattice. In: *Phys. Rev. B*, **90**:3 (2014), 035137. DOI: 10.1103/PhysRevB.90.035137. arXiv: 1405.6062 (see pp. 100, 105).
- [163] S. Kunkemöller, D. Khomskii, P. Steffens, A. Piovano, A. A. Nugroho and M. Braden. Highly Anisotropic Magnon Dispersion in Ca_2RuO_4 : Evidence for Strong Spin Orbit Coupling. In: *Phys. Rev. Lett.*, **115**:24 (2015), 1–5. DOI: 10.1103/PhysRevLett.115.247201. arXiv: 1509.03999 (see pp. 100, 103, 107, 112).
- [164] S. Kunkemöller, E. Komleva, S. V. Streltsov, S. Hoffmann, D. I. Khomskii, P. Steffens, Y. Sidis, K. Schmalzl and M. Braden. Magnon dispersion in $\text{Ca}_2\text{Ru}_{1-x}\text{Ti}_x\text{O}_4$: Impact of spin-orbit coupling and oxygen moments. In: *Phys. Rev. B*, **95**:21 (June 2017), 214408. DOI: 10.1103/PhysRevB.95.214408. arXiv: 1703.10017 (see pp. 100, 103–105).
- [165] A. Jain, M. Krautloher, J. Porras, G. H. Ryu, D. P. Chen, D. L. Abernathy, J. T. Park, A. Ivanov, J. Chaloupka, G. Khaliullin, B. Keimer and B. J. Kim. Higgs mode and its decay in a two-dimensional antiferromagnet. In: *Nature Physics*, **13**:7 (July 2017), 633–637. DOI: 10.1038/nphys4077. arXiv: 1705.00222 [cond-mat.str-el] (see p. 100).
- [166] Sofia-Michaela Souliou, Ji Chaloupka, Giniyat Khaliullin, Gihun Ryu, Anil Jain, B. J. Kim, Matthieu Le Tacon and Bernhard Keimer. Raman Scattering from Higgs Mode Oscillations in the Two-Dimensional Antiferromagnet Ca_2RuO_4 . In: *Phys. Rev. Lett.*, **119**: (6 Aug. 2017), 067201. DOI: 10.1103/PhysRevLett.119.067201 (see p. 100).
- [167] Guoren Zhang and Eva Pavarini. Mott transition, spin-orbit effects, and magnetism in Ca_2RuO_4 . In: *Phys. Rev. B*, **075145**:7 (2017), 1–10. DOI: 10.1103/PhysRevB.95.075145 (see pp. 100, 105, 107, 122).

- [168] Guoren Zhang and Eva Pavarini. Higgs mode and stability of xy -orbital ordering in Ca_2RuO_4 . In: *Phys. Rev. B*, **101**: (20 May 2020), 205128. DOI: 10.1103/PhysRevB.101.205128 (see p. 100).
- [169] Teresa Feldmaier, Pascal Strobel, Michael Schmid, Philipp Hansmann and Maria Daghofer. Excitonic magnetism at the intersection of spin-orbit coupling and crystal-field splitting. In: *Phys. Rev. Research*, **2**: (3 Aug. 2020), 033201. DOI: 10.1103/PhysRevResearch.2.033201 (see p. 100).
- [170] Pascal Strobel, Friedemann Aust and Maria Daghofer. Magnetic phases for strongly correlated t_{2g}^4 electrons on the square lattice: Impact of spin-orbit coupling and crystal field. In: *Phys. Rev. B*, **104**: (11 Sept. 2021), 115148. DOI: 10.1103/PhysRevB.104.115148 (see p. 100).
- [171] Q. Huang, J.L. Soubeyroux, O. Chmaissem, I.Natali Sora, A. Santoro, R.J. Cava, J.J. Krajewski and W.F. Peck. Neutron Powder Diffraction Study of the Crystal Structures of Sr_2RuO_4 and Sr_2IrO_4 at Room Temperature and at 10 K. In: *Journal of Solid State Chemistry*, **112**:2 (1994), 355–361. DOI: <https://doi.org/10.1006/jssc.1994.1316> (see p. 100).
- [172] M. K. Crawford, M. A. Subramanian, R. L. Harlow, J. A. Fernandez-Baca, Z. R. Wang and D. C. Johnston. Structural and magnetic studies of Sr_2IrO_4 . In: *Phys. Rev. B*, **49**: (13 Apr. 1994), 9198–9201. DOI: 10.1103/PhysRevB.49.9198 (see p. 100).
- [173] M.A. Subramanian, M.K. Crawford, R.L. Harlow, T. Ami, J.A. Fernandez-Baca, Z.R. Wang and D.C. Johnston. Sr_2RhO_4 and Sr_2IrO_4 : Structural and magnetic studies of 4d and 5d transition metal analogs of La_2CuO_4 . In: *Physica C: Superconductivity*, **235-240**: (1994), 743–744. DOI: [https://doi.org/10.1016/0921-4534\(94\)91596-2](https://doi.org/10.1016/0921-4534(94)91596-2) (see p. 100).
- [174] M. Braden, G. André, S. Nakatsuji and Y. Maeno. Crystal and magnetic structure of Ca_2RuO_4 ; Magnetoelastic coupling and the metal-insulator transition. In: *Phys. Rev. B*, **58**:2 (1998), 847–861. DOI: 10.1103/PhysRevB.58.847 (see pp. 100, 101).
- [175] D G Porter, V Granata, F Forte, S Di Matteo, M Cuoco, R Fittipaldi, A Vecchione and A Bombardi. Magnetic anisotropy and orbital ordering in Ca_2RuO_4 . In: *Phys. Rev. B*, **98**:12 (Sept. 2018), 125142. DOI: 10.1103/PhysRevB.98.125142 (see p. 101).

Bibliography

- [176] G. Cao, S. McCall, M. Shepard, J. E. Crow and R. P. Guertin. Magnetic and transport properties of single-crystal Ca_2RuO_4 : Relationship to superconducting Sr_2RuO_4 . In: *Phys. Rev. B*, **56**:6 (Aug. 1997), R2916–R2919. DOI: 10.1103/PhysRevB.56.R2916 (see p. 101).
- [177] C. G. Fatuzzo, M. Dantz, S. Fatale, P. Olalde-Velasco, N. E. Shaik, B. Dalla Piazza, S. Toth, J. Pelliciani, R. Fittipaldi, A. Vecchione, N. Kikugawa, J. S. Brooks, H. M. Rønnow, M. Grioni, Ch. Rüegg, T. Schmitt and J. Chang. Spin-orbit-induced orbital excitations in Sr_2RuO_4 and Ca_2RuO_4 : A resonant inelastic x-ray scattering study. In: *Phys. Rev. B*, **91**:15 (Apr. 2015), 155104. DOI: 10.1103/PhysRevB.91.155104. arXiv: arXiv:1503.01574v1 (see pp. 104, 106, 107).
- [178] E. Gorelov, M. Karolak, T. O. Wehling, F. Lechermann, A. I. Lichtenstein and E. Pavarini. Nature of the mott transition in Ca_2RuO_4 . In: *Phys. Rev. Lett.*, **104**:22 (2010), 3–6. DOI: 10.1103/PhysRevLett.104.226401. arXiv: 1001.4705 (see p. 105).
- [179] Guo-Qiang Liu. Competition between spin-orbit coupling and magnetic exchange splitting in Ca_2RuO_4 . In: *Phys. Rev. B*, **88**:10 (Sept. 2013), 104428. DOI: 10.1103/PhysRevB.88.104428 (see p. 107).
- [180] Minjae Kim, Jernej Mravlje, Michel Ferrero, Olivier Parcollet and Antoine Georges. Spin-Orbit Coupling and Electronic Correlations in Sr_2RuO_4 . In: *Phys. Rev. Lett.*, **120**:12 (Mar. 2018), 126401. DOI: 10.1103/PhysRevLett.120.126401. arXiv: 1707.02462 (see p. 107).
- [181] T. Katsufuji, M. Kasai and Y. Tokura. In-Plane and Out-of-Plane Optical Spectra of Sr_2RuO_4 . In: *Phys. Rev. Lett.*, **76**: (1 Jan. 1996), 126–129. DOI: 10.1103/PhysRevLett.76.126 (see p. 107).
- [182] Satoru Sugano, Yukito Tanabe and Hiroshi Kamimura. *Multiplets of transition-metal ions in crystals*. English. Academic Press New York, 1970, xi, 331 p. (See p. 110).
- [183] H. Gretarsson, H. Suzuki, Hoon Kim, K. Ueda, M. Krautloher, B. J. Kim, H. Yavas, G. Khaliullin and B. Keimer. Observation of spin-orbit excitations and Hund's multiplets in Ca_2RuO_4 . In: *Phys. Rev. B*, **100**:4 (July 2019), 45123. DOI: 10.1103/PhysRevB.100.045123 (see p. 123).
- [184] D. Sutter, C. G. Fatuzzo, S. Moser, M. Kim, R. Fittipaldi, A. Vecchione, V. Granata, Y. Sassa, F. Cossalter, G. Gatti, M. Grioni, H. M. Rønnow, N. C. Plumb, C. E. Matt, M. Shi, M. Hoesch, T. K. Kim, T-R Chang, H-T Jeng, C. Jozwiak, A. Bostwick, E. Rotenberg, A. Georges, T. Neupert and J. Chang. Hallmarks of Hund's coupling in the Mott insulator Ca_2RuO_4 . In: *Nat.*

Commun., **8**:May (May 2017), 15176. DOI: 10.1038/ncomms15176. arXiv: 1610.02854 (see p. 123).

- [185] I. Vergara, M. Magnaterra, P. Warzanowski, J. Attig, S. Kunkemöller, D. I. Khomskii, M. Braden, M. Hermanns and M. Grüninger. Spin-orbit coupling and crystal-field splitting in Ti-doped Ca_2RuO_4 studied by ellipsometry. In: *Phys. Rev. B*, **106**: (8 Aug. 2022), 085103. DOI: 10.1103/PhysRevB.106.085103 (see p. 134).

Publications

- [120] F. Randi, I. Vergara, F. Novelli, M. Esposito, M. Dell'Angela, V. A. M. Brabers, P. Metcalf, R. Kukreja, H. A. Dürr, Daniele Fausti, M. Grüninger and F. Parmigiani. Phase separation in the nonequilibrium Verwey transition in magnetite. In: *Phys. Rev. B - Condens. Matter Mater. Phys.*, **93**:5 (2016), 1–10. DOI: 10.1103/PhysRevB.93.054305. arXiv: 1509.04550 (see pp. 79, 85, 90, 97, 137).
- [186] N. Borgwardt, J. Lux, I. Vergara, Zhiwei Wang, A. A. Taskin, Kouji Segawa, P. H. M. van Loosdrecht, Yoichi Ando, A. Rosch and M. Grüninger. Self-organized charge puddles in a three-dimensional topological material. In: *Physical Review B*, **93**:24 (June 2016), 245149. DOI: 10.1103/PhysRevB.93.245149.
- [187] R. B. Versteeg, I. Vergara, S. D. Schäfer, D. Bischoff, A. Aqeel, T. T. M. Palstra, M. Grüninger and P. H. M. van Loosdrecht. Optically probed symmetry breaking in the chiral magnet Cu_2OSeO_3 . In: *Physical Review B*, **94**:9 (Sept. 2016), 094409. DOI: 10.1103/PhysRevB.94.094409.
- [188] Stefan Schumacher, Felix Huttmann, Marin Petrovi, Christian Witt, Daniel F. Förster, Chi Vo-Van, Johann Coraux, Antonio J. Martinez-Galera, Violetta Sessi, Ignacio Vergara, Reinhard Rückamp, Markus Grüninger, Nicolas Schleheck, Frank Meyer zu Heringdorf, Philippe Ohresser, Marko Kralj, Tim O. Wehling and Thomas Michely. Europium underneath graphene on Ir(111): Intercalation mechanism, magnetism, and band structure. In: *Phys. Rev. B*, **90**: (23 Dec. 2014), 235437. DOI: 10.1103/PhysRevB.90.235437.

